Strongly correlated Hubbard model within the composite operator formalism

Louis Haurie

université PARIS-SACLAY

Strongly correlated Hubbard model within the composite operator formalism

Régime fortement corrélé du modèle de Hubbard étudié avec le formalisme des opérateurs composites.

Thèse de doctorat de l'université Paris-Saclay

École doctorale n° 564, "Physique en Île-de-France", EDPIF
Spécialité de doctorat: Physique
Graduate School : Physique. Référent : Faculté des sciences d'Orsay

Thèse préparée dans l'unité de recherche **IPhT (Université Paris-Saclay, CNRS, CEA)**, sous la direction de **Catherine Pépin**, directrice de recherche au CEA.

Thèse soutenue à Paris-Saclay, le 20 septembre 2024, par

Louis HAURIE

Composition du jury

Membres du jury avec voix délibérative

Luca DE' MEDICI Directeur de recherche, LPEM, Université PSL	Président
Robert EDER Privatdozent, eq. HDR, Karlsruhe Institute of Technology,	Rapporteur et Examinateur
Karyn LE-HUR Directrice de recherche, Center for Theoretical Physics, Ecole Polytechnique	Rapporteuse et Examinatrice
Cécile REPELLIN Chargée de recherche, LPMMC, Université Grenoble Alpes	Examinatrice

THESE DE DOCTORAT

NNT : 2024UPASP073

université PARIS-SACLAY

ÉCOLE DOCTORALE
Physique en Île-de-France (PIF)

Titre: Régime fortement corrélé du modèle de Hubbard étudié avec le formalisme des opérateurs composites

Mots clés: corrélations électroniques, modèle de Hubbard, fonctions de Green, equations du mouvement

Ce manuscrit considère une approche dans un régime de fortes corrélations partant d'un état fondamental décrivant un isolant de Mott obtenu avec un large terme de répulsion électronique Coulombienne pour un réseau carré. Les opérateurs de Hubbard sont de bonnes excitations pour ce terme, puisqu'ils décrivent correctement la phase de Mott. Un terme de saut est alors ajouté dans un traitement du modèle de Hubbard basé sur les équations du mouvement. Une approximation est réalisée pour tronquer les courants des opérateurs de Hubbard et permettre une approche auto-cohérente. Différents jeux d'équations auto-cohérentes sont usuellement considérés dans la littérature et sont d'abord analysés pour des systèmes invariants par translation. La méthode viole le théorème de Luttinger et ne présente une symétrie particule trou qu'avec des termes de saut pour les plus proches voisins. Nous l'étendons alors pour étudier la supraconduction en symétrie d et des sauts vers des voisins plus éloignés. Bien que nous arrivons à stabiliser la supraconduction, nous montrons qu'elle n'est non-nulle qu'uniquement au voisinage d'une singularité de Van Hove. En incluant les sauts vers des voisins plus éloignés, la singularité de Van Hove comme le pic de supraconduction est décalée vers des dopages plus élevés. Finalement, un modèle de Hubbard à deux orbitales est considéré en tant qu'application de la méthode. Lorsque l'énergie de saut interorbitale est suffisamment faible, une brisure symétrie spontanée est observée sur les orbitales. En l'absence de cette énergie, la phase obtenue n'est pas hybridée et possède une orbitale demi remplie, ce qui correspond aux éléments caractérisant une phase de Mott orbitalement sélective, sans avoir à considérer un terme de Hund. Alors que l'énergie de saut inter-orbitale augmente, cette phase de Mott selective survit, mais gagne légèrement en hybridation alors qu'une des deux orbitales n'est désormais plus exactement demi remplie. Passé une valeur critique, cette phase de Mott orbitalement sélective est brisée, et le système passe dans une phase orbitalement uniforme.

Title: Strongly correlated Hubbard model within the composite operator formalism
Keywords: electronic correlations, Hubbard model, Green's function, equations of motion

Abstract: This manuscript considers a strong coupling approach starting with the expected ground-state of a Mott insulator obtained for a large Coulomb electronic repulsion term with a square lattice. The Hubbard operators are good excitations for this interaction term, as they describe properly the Mott phase. Hopping is then considered in an equation of motion treatment of Hubbard model. An approximation is performed to truncate the currents of the Hubbard operators and allow for a self-consistent framework. Different sets of self-consistent equations are typically considered in the literature and are firstly analyzed for translationally invariant systems. The method violates Luttinger's theorem and is only particle-hole symmetric with nearest-neighbors. We then extend it to study d-wave superconductivity and longer-range hopping. While we managed to stabilize superconductivity, we show it is non-zero only in the vicinity of a Van Hove singularity. As longer ranged hoppings are included, the Van hove singularity is moved away to higher doping and so does the superconductivity peak. Finally, a two-orbital Hubbard model is considered as an application case of the method. For small enough inter-orbital hopping and no inter-orbital interaction, a spontaneous orbital symmetry breaking is observed. In the absence of inter-orbital hopping, the resulting phase is unhybridized and has one orbital close to half-filling, presenting the characteristic features of the orbital-selective Mott phase without having to consider any Hund term. As the inter-orbital hopping is switched on, this selective Mott phase survives but becomes slightly hybridized and with an orbital not exactly half-filled anymore. Past a critical value, this orbital selective phase is broken and the system goes in an orbital uniform phase.

Contents

1 . Acknowledgement

Je souhaite avant tout remercier ma directrice de thèse Catherine Pépin de m'avoir donné la chance d'effectuer cette thèse. Au-delà de tout ce que j'ai pu apprendre en matière condensée, de la rigueur et de l'esprit d'initiative qu'elle m'a permis de développer, cette thèse m'a beaucoup apporté personnellement et fait gagné en recul et en maturité. Ce fut une vraie expérience psychologique grandeur nature ! Et je suis certain qu'elle me servira pour le restant de ma vie, tant professionnellement qu'émotionnellement.

Je voudrais également particulièrement remercier mes collègues Anurag Banerjee et Emile Pangburn avec qui j'ai vraiment apprécié de travailler. J'ai beaucoup de reconnaissance pour le temps qu'ils ont pris pour discuter avec moi sur les problèmes que nous avons pu rencontrer et pour le soutien qu'ils m'ont apporté. Je remercie également Sébastien Burdin et Cristina Bena pour leurs conseils et discussions intéressantes dans le cadre de plusieurs projets collaboratifs. De manière plus générale, je souhaite remercier tous mes collègues doctorants et post-doctorants de l'IPhT pour leur bienveillance, ainsi que tous les bons moments que nous avons passés ensemble: Benjamin, Marc, Duc, Rémi, Dimitri, Siggtriggur, Pavel, Linéa, Maxence, Soufiane, sans oublier ceux avec qui j'ai interagi plus ponctuellement. Je pense également à mes anciens professeurs qui m'ont transmis une passion pour la physique, Patricia, Caroline et Daniel, ainsi que ceux qui m'ont tant appris lors de mes années universitaires.

Enfin, je souhaiterais remercier ma famille de m'avoir toujours soutenu et plus particulièrement ma tante et mon oncle Dany et Pierre, mes tantes Pascale et Christine, ainsi que feu ma mère. Cette thèse fut loin d'être sans son lot de difficultés et sa charge mentale, et je n'aurais jamais pu tirer profit de ces épreuves sans l'aide de mes amis. Je remercie Marie, Louis, Vincent, Emeric, Lucas, Florine, Victoire et plus particulièrement Charlotte, Némo et Benjamin pour leur présence, leur soutien et leur gentillesse.

2 . Introduction

Investigating strong electronic correlations is a central challenge in quantum matter, underlying many non-trivial phenomena, such as high-T_c superconductivity, Mott insulators, and heavy Fermi liquids, among others. The significant interactions between different degrees of freedom in quantum materials lead to multiple broken symmetry phases, resulting in an extremely rich phase diagram.

The Hubbard model is a central focus of theoretical efforts to understand strong correlations. More than 50 years after it was first introduced, it remains an intensive topic of study even now. The main question at the core of these investigations is whether this simple yet still undefeated model is enough to predict exotic behaviors caused by correlations and, more importantly, whether it can provide a physical scenario to explain the appearance of such behaviors. Instances of these can involve unconventional superconductivity, charge density waves, selective Mott insulators, or even the putative pair density waves. In this manuscript, we consider the composite operator method, initially introduced to encompass the strongly correlated regime of the Hubbard model.

Chapter 3 offers a physical and equationless presentation of the relevance of strong electronic correlation. It also qualitatively introduces several key concepts of this phd.

Chapter 4 presents more in depth important theoretical frameworks and studies we will use as a basis for most of this work. Namely, after a general introduction on second quantization and Green's function, we present the Hubbard model and perform a detailed study of Hubbard I approximation. For the sake of an analogy occurring in chapter 6, Kondo physics is also lightly introduced.

In **Chapter 5** the main technique used in this manuscript, the composite operator method, is completely presented and detailed. The two usual self-consistent schemes performed with this method, "Roth" and "Pauli" schemes are then introduced and compared. After making various benchmark with litterature, we conclude which solution is the most physical. We then consider the study to the violation of Luttinger theorem as well as a particle-hole symmetry. The method is then extended to d-wave superconductivity and longer ranged hopping. The goal of this chapter is therefore characterizing and understanding composite operators.

Finally, in **Chapter 6** we apply the technique to a two orbital hubbard Hamiltonian. No inter-orbital interaction is considered, but the inter-orbital hopping is fixed as an external parameter. Translational invariance is still imposed. A spontaneous orbital symmetry breaking is observed when this parameter is small enough, and the system can enter in an orbital selective Mott phase, even though no Hund term has been considered.

3 . The importance of strong interaction physics

3.1 . Early days in the physics of interactions

3.1.1 . Free electrons gas

A crystal is defined by an ordering of atoms. Despite some possible irregularities or local impurities [1, 2], it is commonly assumed to be a periodic system described by a lattice. Valence electrons may move or remain on lattice sites, each of them containing positively charged ions enforcing charge neutrality [3, 4, 5]. Because of the assumed discrete translational invariance, momentum of the electrons (product of mass and velocity) is a good quantum number and is usually introduced in the study of these systems. It is by definition the associated Fourier variable of the position of the electrons in the lattice [3]. For simplicity, this position is usually defined only in the Wigner-Seitz unit cell, which contains exactly one lattice site. This cell is repeated in space, and atomic nucleus with their core electrons are positioned within it. Conversely, momentum is defined in the Brillouin zone which is analogous to the Wigner-Seitz unit cell within the reciprocal lattice obtained from a Fourier transform [6, 7].

One of the first assumption made in these models is the weakly interacting nature of valence electrons. They can move between lattice sites without feeling too much repulsion. This free electron gas model (oftentimes referred as Fermi gas) was one of the early success of condensed matter, allowing to predict the electrical nature of crystal. To analyze this system, Bloch assumed valence electrons should be described as the solutions of a Schrodinger equation with a periodic potential of period equal to the length of an unit cell. His theorem [8] states that the solution of such a Schrodinger equation are plane wave modulated by a periodic potential. Thus the energies of valence electrons depend on their positions within the Wigner-Seitz unit cell. In the reciprocal lattice, this leads to eigenvalues dependent of the momentum. Hence, the name "bands" was introduced, as the energy levels are not flat anymore when represented along position or momentum.

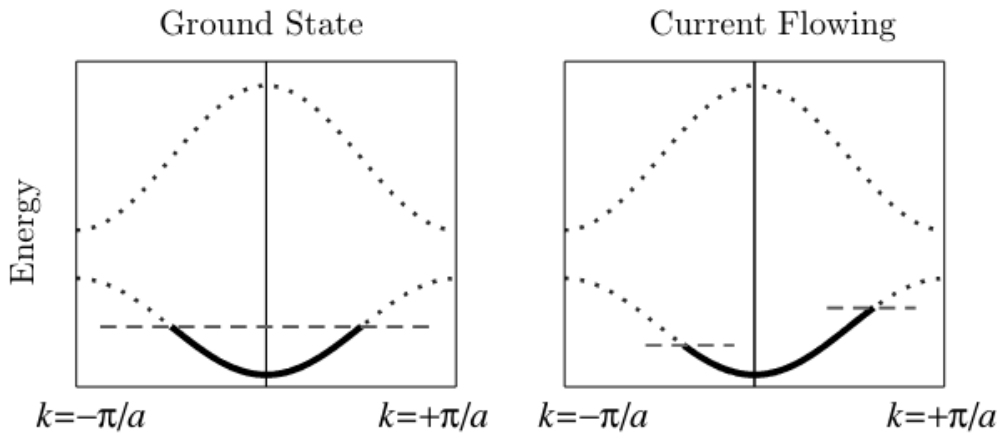

Figure 1: Display of the bands of a one dimensional system. (left): in the ground-state, the band is half-filled. (right): if a current occurs electrons accelerate, resulting in a shift in the filling of the band. This figure is taken from Ref. [9]

The insulating or conducting nature of a material can then be described by considering the occupation of the bands [10]. Since electrons are fermions, in the absence of thermal excitations, they will populate the lowest energy level of the bands and fill them progressively. The highest energy occupied by an electron is called the Fermi energy (horizontal dashed line in the ground-state of fig. 1).

Let's assume there is a current in the crystal (for instance by mean of an external electric field). The electrons then gain velocity as they describe a global flow. This creates a shift in momentum. However, as the energy of the electrons is constrained to the bands, this shift can only change the filling of the band as depicted on fig. 1. Therefore a Fermi gas with states available above the Fermi energy describes a metal [9]. In the case of a fully filled band, this shift in occupation cannot occur because all states are filled and Pauli exclusion principle forbid two electrons of being in the same state. In that case, a current can only occur if the electrons gains enough energy to hop in an empty band at higher energy. Depending on the value of the energy gap between the filled and empty bands, the system is either an insulator or a semi-conductor (small gap).

Despite an experimental agreement with most of the materials, bands theory is not able to predict the behavior of all materials. This can be explained by two main arguments. First, because some materials are too heterogeneous due to the presence of defects or impurities for the system to be described with a periodic potential. [5, 9]. Second and this point will be the main interest of this manuscript, because electrons of this model are assumed weakly interact. While this assumption may be reasonable for a broad range of materials, a rich amount of physical behaviors find their origin in electronic interactions.

3.1.2 . Fermi liquid and quasi-particles

Fermi liquid is the conventional way of treating electronic interactions. This theory was first introduced qualitatively by Landau, and a more formal and mathematical framework was given later on [13, 14, 15].

The key concept of Fermi liquid theory is adiabaticity: the electronic interaction is very slowly switched on in the system [16]. In the absence of interaction, the usual Fermi gas model applies. For simplicity let us consider the situation at vanishing temperature. Because of Fermi-Dirac statistics, electrons are going to occupied states up to the Fermi energy. This will create a Fermi sea (the ensemble of occupied states) and a Fermi surface (the cross-section in momentum space of the bands at the Fermi energy). If the interaction is now slowly switched on, Fermi liquid theory predicts a change in the dynamic properties of the electrons due to electronic repulsion. Namely, their mass or their momentum are going to be renormalized [17]. No symmetry will be broken, and the Fermi sea turns to an interacting ground-state of "dressed" particles. These quasi-particles present particle-hole excitations analogous to the Fermi gas situation, but are the results of the interactions and have different dynamical properties, such as an effective mass [18].

A typical characteristic property of a Fermi liquid behavior is a discontinuity in the electron density in momentum space in the neighborhood of the Fermi surface. As sketched on Fig 2, for the classic Fermi gas the electron density is always equal to one (or 2 in the case of spin degeneracy) for momentum inside the Fermi surface and jumps to zero for momentum out of the Fermi sea. In the case of a Fermi liquid, the situation is different: due to interactions, it is possible for an electron near the Fermi

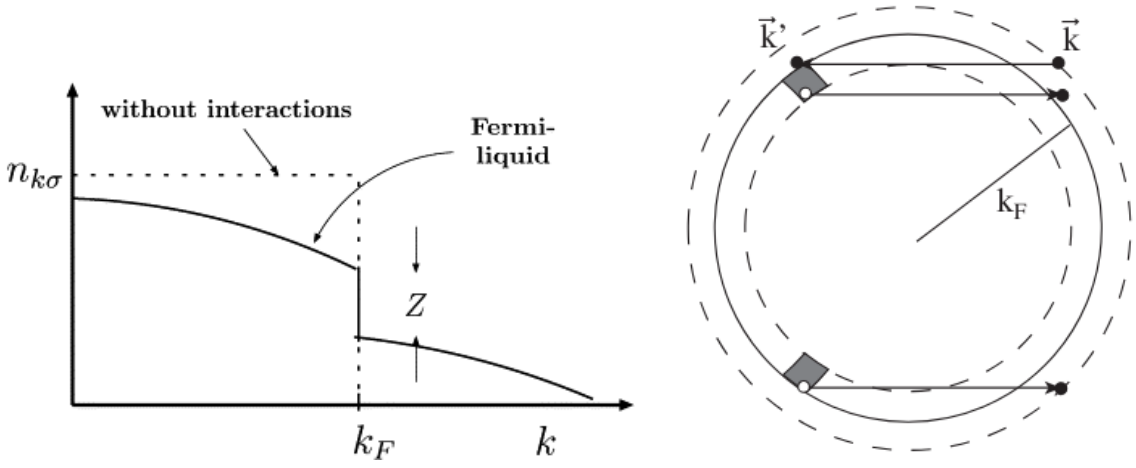

Figure 2: (left): Electron density as a function of momentum modulus. In the ideal Fermi gas, below k_F in the Fermi sea the electron density is fully filled (one, or two in the case of spin degeneracy). It then drops to zero above k_F. In the case of a Fermi-liquid, scattering processes occurs due to electron interactions and creates a drop of the electron density in the Fermi sea, and an enhancement of the density above the Fermi energy. (right): display of such a particle-hole excitation: due to interactions, scattering processes occur and electron at momentum k greater than k_F decays to momentum k' at a lower energy, closer the the Fermi surface. Due to momentum conservation, an electron inside the Fermi surface is then scattered out of the Fermi sea. These scattering processes justify why some particles resides outside of the Fermi sea (and respectively some hole are inside), making Z smaller than 1. The figures are respectively from Ref. [11] and [12].

surface to be scattered, losing some energy and momentum. Because of momentum conservation another electron from within the Fermi sea is then scattered out of the Fermi surface. These excitations causes a non-zero density above k_F for Fermi liquid, and conversely lower the density below k_F. Therefore the initial discontinuity of the Fermi gas is smaller, and called "quasi-particle weight" Z. This weight can thus be described as the overlap between the quasi-particle and bare electrons so that Z in the Fermi gas case. It is important to note that this quasi-particle weight is not exclusively observed in Fermi liquids. In sec. 6.3.3 we display a jump in the momentum resolved electron density for a non-Fermi liquid phase. The interpretation remain similar, and this is still measuring overlap between quasi-particles and bare electrons, but these quasi-particles are rather emerging directly from the existence of a Fermi surface.

3.1.3 . Luttinger theorem

Not every strongly correlated system is well described by a Fermi liquid. The adiabatic assumption is not always satisfied, there can be discontinuities that can break this assumption. These phases that display a non Fermi liquid behavior are still nowadays an intensive research topic. Example of these includes the famous one dimensional Luttinger liquid [19] or the strange metal observed in cuprates materials with a linear resistivity with temperature [20] while Fermi liquid theory would predict a

quadratic resistivity. In the case of Mott Insulators usually observed around half-filling for a large variety of strongly correlated materials [21], no Fermi surface exists causing a definition issue of the theorem. Suggestions for solving this issue have been made by considering a Luttinger surface from the zero of the Green's function [22].

In a Fermi gas at vanishing temperature, every states under the Fermi energy are filled. As a consequence, if one displays the Fermi surface, all momentum enclosed by the Fermi surface are occupied by electron. Therefore, it is clear that the enclosed volume of the Fermi surface is equal to the number of electrons in the system. Characteristic of a Fermi liquid behavior, Luttinger theorem states that despite interaction, the Fermi surface of the quasi-particles will keep enclosing the number of charge carriers of the system [23, 24].

A perturbative proof of the theorem was first performed using Luttinger-Ward functionnal [25]. Later, a non-pertubative proof was developped using topological argument [26]. In both cases it is assumed the considered system is a Fermi liquid. A strong debate remains on whether the Luttinger theorem is satisfied or not in the case of non Fermi liquid system, with many suggestions of how to extend the theorem to various cases [27, 28]. In the case of the Hubbard model, a Luttinger breakdown has been reported using Determinantal Monte-Carlo simulations [29]. This is possible, as several studies reported the non-Fermi liquid behavior of the Hubbard model [30, 31].

Further work also reports a violation of the theorem for the Hubbard I approximation [32]. In Sec. 4.2.3, this approximation is studied in depth and the area of the Fermi surface will be computed in the neighborhood of half-filling to confirm Luttinger breakdown. In Sec.5.2.2 the analysis of the theorem is also studied with the composite operators method.

3.2 . The case of Superconductivity

3.2.1 . BCS theory

Superconductivity is the typical example of interactions (whether they are weak or not, between electrons or between electrons and lattice) giving birth to exotic behavior at very low temperatures. Macroscopically, a superconductor is known for two main properties: perfect conductivity with a vanishing resistivity, and the Meissner effect. The latter is a consequence of the perfect diamagnetism in superconductors, causing material in this phase to repel magnetic fields [33]. In this section we introduce qualitatively BCS theory and sketch the relevance of interaction to the modelisation of superconductors.

Because of particle-wave duality, the collective motion of the lattice can be described by particles called phonons which correspond to the quantum of vibrational energy require to excite the lattice. One key experiment indicating the relevance of phonons in the superconducting states us the isotope effect. The superconducting critical temperature below which a material enter a superconducting phase decays with the isotope mass of the lattice [34, 35, 36]. This experiment showed importance in the vibrational modes of the lattice and was later explained by BCS theory.

BCS theory relies on the notion of Cooper pairs to model superconductivity [37, 38]. BCS theory suggested phonons as an attractive pairing mechanism leading to pairs of opposite spin and momentum. Let us first provide a qualitative scenario to justify such type of pairing of electrons. Consider an electron propagating in the lattice. Because the lattice sites are positively charge, they are going to be attracted by this electron. This attraction creates some vibration of lattice sites, that are going to

change the electrostatic properties of other electrons. Correlations then gets created between electrons of opposite spins and momentum in the lattice, forming pairs. The situation is described in Fig 3a.

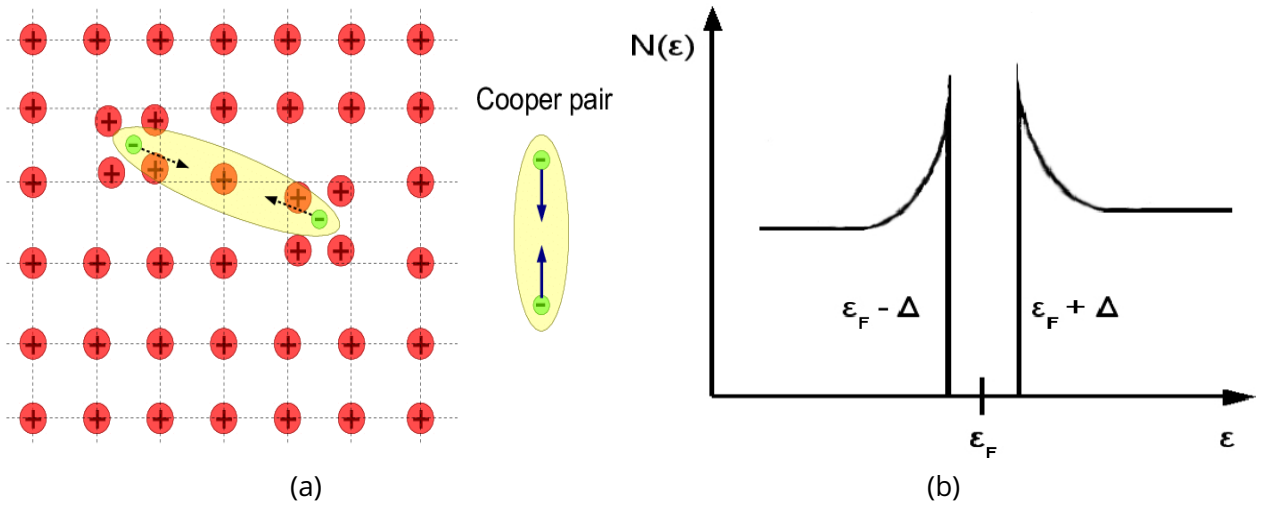

Figure 3: (a): sketch of the formation of a Cooper pair in the lattice for a conventional superconductor. A correlation between electrons of opposite spins and momentum is created by the vibrations of the lattice due to the attraction between lattice sites and electrons. Taken from ref. [39]. (b): Display of the profile of the density of states for a BCS superconductor. At a low enough temperature the Cooper pair form a Bose-Einstein condensate and cannot be described as single electrons anymore, resulting in a gap Δ in the density of states around the Fermi energy ϵ_F.

BCS theory relies on the idea that at low enough temperature, the Cooper pairs form a Bose-Einstein condensate. A pair of electrons is indeed a boson. As such, they all get into the same ground-state energy at vanishing temperature. Since Cooper pairs are not single electrons anymore, at low enough temperature the electronic density of states looses states associated to the electrons involved in pairing. This typically opens up a gap [38, 40] in the density of states sketched on Fig. 3. It is then possible to prove the supercurrent and the perfect diamagnetism find their origin in this coherence of the bose-Eistein condensate[41].

3.2.2 . Superconductivity in cuprates

In 1986, G. Berdnoz and K. A. Müller observed the first signature of high critical temperature superconductivity in cuprates [42]. These are a materials family composed of oxygen and copper plans with various atoms in between acting as charge reservoirs. These atoms can be substituted to modify the electronic doping within the planes. As such, most of the physics happens within these plans [20, 43]. According to Band theory, undoped cuprates have half-filled bands and should be metallic but are rather insulator, due to the strong electronic repulsion effects within the planes. At half-filling, cuprates are described as Mott-insulators [20, 44]. These strong correlations are at the center of a very rich phase diagram displayed in Fig 4 where superconductivity is only one among many exotic phases. Although not central to this manuscript, we will briefly mention the pseudogap phase and

the strange metal phase. The pseudogap is believed to be possibly related to the formation of superconductivity and is characterized mainly by a loss in the density of states at the Fermi energy for specific momentum and the absence of Fermi surface, only "Fermi arcs" are observed experimentally [45]. On the other hand, the strange metal is known for a linear resistivity with temperature, contrary to the usual quadratic behavior of Fermi liquids [46].

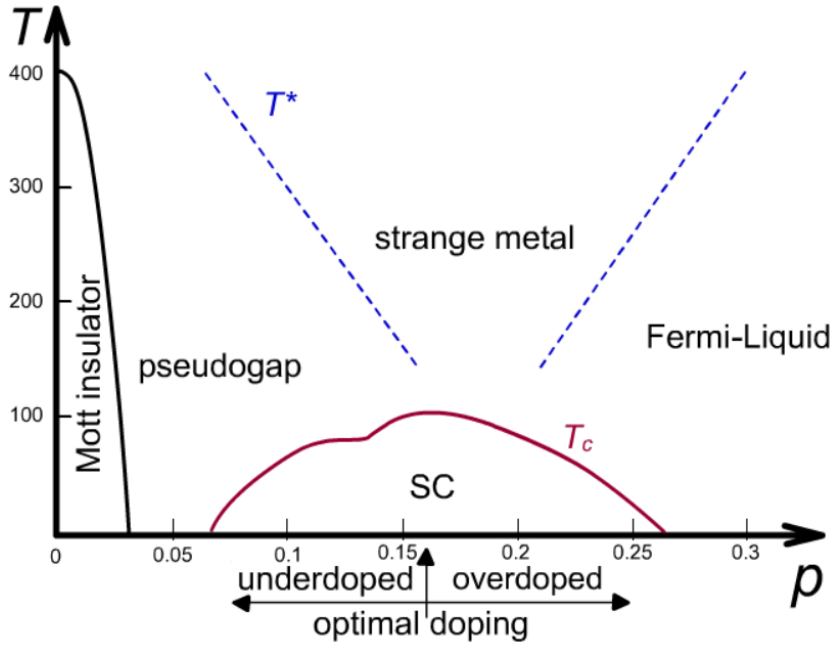

Figure 4: Sketch of the typical shape of cuprates phase diagram. p denotes the hole doping concentration. In the vicinity of half-filling, due to strong electronic correlation the material is a Mott insulator with an antiferromagnetic ordering. Two exotic phases are intensively studied in the vicinity of the superconductivity (SC) dome, the pseudogap and strange metal phase. As we mostly focus on the Mott and superconducting phase, they will not be described in depth. Let us finally note a Fermi liquid behavior is observed at high hole-doping. Taken from [47].

Because conventional superconductivity is caused by electron-phonon interaction, it is possible to give an estimate of the highest critical temperature (below which the material becomes a superconductor) in these materials using the Debye frequency [37]. This temperature is estimated under normal pressure at roughly 40K. In some cuprates compounds, the critical temperature can reach up to 160K. This means the pairing mechanism of such superconductors is not the usual electron phonon interaction. Later on, other families of materials have exhibit unconventional superconductivity, such as iron pnictides or strontium Ruthenate [48, 49].

While there is still an experimental and theoretical consensus of Cooper pairing [50, 51], the great mystery of unconventional superconductivity is the origin of the interaction allowing the formation of such pairs [52]. Let us note that the Cooper pairs of these systems are not always on site with opposite spin pairs. The superconductivity order parameter can indeed be decomposed in the symmetries of the lattice [12]. The ground-state energy can then be computed for each of these symmetries and the

system form pairs in the lowest symmetry channel. While most conventional superconductors have an s-wave symmetry, cuprates superconductivity is for instance d-wave [50].

3.2.3 . Superconductivity within the Hubbard model

The Hubbard model was suggested as a simple yet challenging model to analyze electronic interactions. In this model electrons can hop from one site to another, but with a strong repulsion or attraction (depending on the sign of the interaction term) whenever two of them lie at the same site with opposite sites. Initially introduced in 1963 [53], it remains a theoretical challenge today. It has been exactly solved in one dimension [54] but requires various approximation schemes in dimension n greater than one.

In the early days of the model, many studies were focused on understanding the Mott phase such as the one observed in cuprates close to half-filling [53]. To this end, various schemes were developed. The usual Hartree-Fock approximation has shown good description of the magnetic phase in the weakly interacting limit [55], but as it is a weak coupling perturbative technique, it is not well suited for describing the metal-insulator transition where interaction is strong [56]. The Hubbard I approximation, derived in Sec. 4.2 provided the first qualitative explanation of Mott-Insulators. It is however only suited for the strong correlated regime, as the approximation mainly comes from the atomic limit without any hopping. It also has notable drawbacks such as an electron-hole symmetry violation [55]. To enhance it, other approximations were introduced such as the Hubbard-II and III. In Hubbard II approximation, a frequency dependent self-energy correction to be determined self-consistently is added to model the behavior of an electron of spin σ which can either hop on electrons of spin $\bar{\sigma}$ or empty sites. Electrons of spin $\bar{\sigma}$ are assumed to not move, while in Hubbard-III approximation this assumption is lifted and both spins are considered to fluctuate [55, 57].

Motivated by the rich physics of phases and order of cuprates, an underlying question of the model also consists in determining the ground-state, and whether superconductivity can be stabilized. Indeed, due to the close proximity of Mott-insulators and the superconducting domes in these materials, a natural question was about the connection between these two phases. To this end, more sophisticated techniques were applied, such as Density Matrix Renormalization Group (DMRG), Gutzwiller wave function approximation or Determinantal Quantum Monte Carlo (DQMC) [29, 58, 59]. Dynamical Mean Field Theory (DMFT) solved the model in infinite dimensions by performing a mapping on an Anderson impurity problem. DMRG turned out to be a good method for one dimension, but is becoming too complex for higher dimensions.

Recent studies [60, 61, 62] have shown the groundstates of the model is mainly composed of vertical stripes in the strongly correlated regime around 12% hole doping: these stripes are a charge ordering in space of the electrons, with superconductivity at higher energy. Already expected [63], the competition between charge density waves and superconductivity is also a core question of the Hubbard model, as people now try to understand what changes to the model can favor superconductivity over stripes formations [64].

3.3 . Orbital selective Mott-insulators

3.3.1 . The one orbital Mott-Insulator Physics

Already mentioned in the discussion on cuprates and Hubbard model, Mott-Insulators are a typical example of a non-conventional behavior caused by electronic repulsion because they cannot be well described by bands theory detailed in Sec. 3.1.1. The understanding of Mott physics was one of the first important achievement made by the Hubbard model in the strongly correlated regime.

Qualitatively, according to Hubbard-I approximation and later developed schemes, the insulating nature of this phase is due to the considerable energy penalty electrons have to pay if they form a pair due to Coulomb repulsion. Therefore at half-filling, the lowest energy configuration would be the one with exactly one electron on each lattice site [65]. Let us then assume an electron tries to hop on a neighboring site with another electron of opposite spin. This would create a pair, and penalize so much the system in energy than this hopping process is very unlikely. Then, electrons are likely to stay on their respective lattice site, and this localization makes the system insulator. It is also very common for Mott-insulator to form some kind of antiferromagnetic ordering, where the spin of the electrons get flip from one site to its nearest neighbors. This is rather well understood by Heisenberg model, which can be obtained from the Hubbard model at half-filling with stron correlation by mean of a Schrieffer-Wolff transformation [66].

While there is now a consensus that Mott-insulators are well understood, important questions remain on their relationship with high temperature superconductors. Some models such as the Hatsugai-Kohmoto Hamiltonian have even been analyzed to present a superconducting instability when hole doping a Mott insulator [44]. The question of the relation between the Mott parent compound and the superconducting phase upon doping is also deeply related to the question of charge order formation, as proven by recent scanning tunneling experiments showing the emergence of checkerboard patterns [67]. Since the Hubbard model describes so well Mott-insulators and the metal-insulator transition upon doping, it is also at the center of theoretical efforts to understand superconductivity and charge order formation away from half-filling. This regime is difficult to capture by DQMC: because of the sign problem the method is mainly applied at half-filling [97]. DMFT has been a popular method for studying the energy of these phases in the vicinity of half-filling [55].

After revisiting Hubbard I approximation in Sec. 4.2 and recovering the usual Mott-insulator physics, we will mostly focus on the composite operator method. We will see the method can be applied in the vicinity of half-filling. In Sec. 6 the analysis is then extended to a two orbitals Hubbard model, each with strong repulsion for double occupancy. At half-filling the model is expected to be in a Mott phase with one electron on each orbital for a given phase. In this system the question of what happen upon doping is interesting. Will the ground-state still be an orbital uniform phase with the same electron density on each orbital, or can a spontaneous orbital symmetry breaking happen ? This type of orbital selectivity is usually obtained theoretically by considering a Hund term [71].

3.3.2 . Hund's coupling within multi-orbital systems

Hund's rules have been introduced in 1925 by physicist Friedrich Hund in the study of degenerated atomic shells. These rules explain how to fill them with electrons: electrons must first occupy empty spots and all single occupied spots must align their spins to maximize total spin [68]. These rules have to be also considered also for crystals.

Whenever a lattice is introduced, the crystal field lifts the degeneracy of the atomic orbitals depending on the symmetry of the considered lattice [69]. A sketch of the effect of the crystal field for

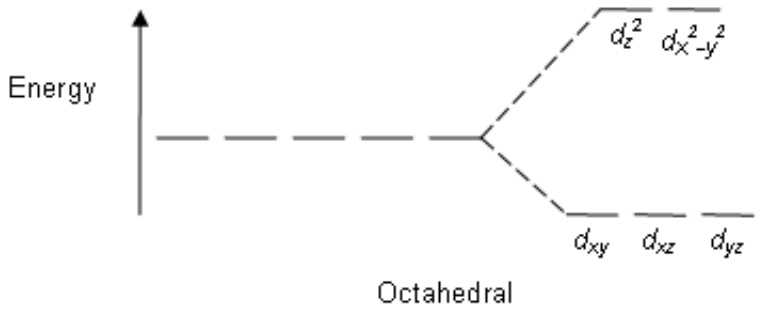

Figure 5: Example of the effect of crystal field effect on a d-shell of a free ion (sketched by 5 degenerated energy level on the left) for a Octahedral lattice symmetry. The resulting energy levels are 3 degenerated crystal orbital d_{xy}, d_{xz}, d_{yz} and 2 degenerated orbitals d_z^2 and $d_{x^2-y^2}$.

an octohedral lattice symmetry is shown on Fig. 5. Some crystal orbitals can still be degenerated in energy after considering the crystal field effect. Hund's term makes spin alignment on the of a given set of degenerated crystal orbitals favorable.

Hund's coupling has three different effects on an ordinary metal [70]. Firstly, it tends to enhance the effective mass of the quasi-electrons. Second, it has a natural effect on spin correlation as it forces singly occupied sites to align. Finally, in the case of a multi-orbital system it tends to enhance the electronic correlation of one of the orbital and cause a spontaneous orbital symmetry breaking [71]. These properties have been confirmed theoretically using DMFT [72, 73] or DMRG where Hund's term is showed to enhance superconductivity of a two orbital system [74].

In a typical Mott-insulator described by a one band Hubbard model, the charge fluctuation vanishes as we approach the Mott phase due to the penalized double occupancy and the charge localization. This contrast with the effect of Hund coupling, where the constrains affect spin rather than charge. Hund term is directly involved in the value of the Coulomb repulsion necessary to stabilize a Mott insulator in the vicinity of half-filling. This result is typically obtained by adding a Hund term the Hubbard model, as it increases the Mott gap it at half-filling and reduce it away from half-filling [75].

3.3.3 . Selective Mott insulators

Beside its relationship with Mott insulators, Hund term has shown importance to differentiate two degenerated set of crystal orbitals [76, 77]. In this regard several works report that this term must be considered to obtain an orbital with an important mass renormalization compared to the other. It is also believed to be a key ingredient in the formation of an orbital selective Mott-Insulator phase (OSMP) [75, 78]

OSMP was first proposed to explain the coexistence of metallic and magnetic properties in ruthenates [79, 80] and has since been recognized as key for understanding the normal [49] and superconducting properties [81, 82] of iron-based superconductors. It is characterized by the selective localization of electrons in specific orbitals, while electrons in other orbitals remain itinerant. Initial evidence

came from Angle-resolved photoemission spectroscopy (ARPES) studies [83] in $Ca_{1.8}Sr_{0.2}RuO_4$, followed by similar observations in iron-chalcogenides [84]. In these materials, the spectral weight of the d_{xy} orbitals vanishes upon cooling, while the spectral weight of other $3d$ orbitals remains non-zero. More recently, theoretical proposals suggest that OSMP could also emerge in twisted bilayer systems such as twisted dichalcogenides [85] and twisted trilayer graphene [86].

This phase has been theoretically studied with either a multi-orbital Hubbard model with inter and intra orbital on-site interaction or with Hund coupling or both[87]. In the OSMP, one orbital is completely localized and decoupled from the other metallic orbitals. The stability of OSMP phase with respect to kinetic inter-orbital interactions remains a subject of debate. While there is agreement among various methods that an OSMP exists when the hopping between different orbitals is negligible, the situation becomes more intricate when it is non-zero. Slave-spin method shows stability of the OSMP phase with inter-orbital hopping [88, 89], with the hybridization of the localized orbitals to the others renormalized to zero. Single-site DMFT shows opposite results [90] claiming any amount of inter-orbital hopping should lead to a finite hybridization. Both methods nevertheless agree that for finite hybridization orbital differentiation exists with a large difference in effective mass. The hybridization of the OSMP is reminiscent of the Kondo model. In the latter, a lattice of strongly interacting impurities is connected to a lattice of conduction electron by mean of a hopping from the conduction to the impurity lattice. While the two systems are not exactly similar, some analogies can be make between the OSMP we observe in Sec. 6 with a composite operators treatment of the 2 orbital Hubbard model and Kondo model. For this reason, Sec. 4.3 provides a light introduction on Kondo physics.

3.4 . The composite operators method

3.4.1 . State of the art

While the Hubbard-I approximation discussed in Sec. 4.2.2 is a good enough scheme to understand Mott insulators, there are now more advanced methods that showed good results in the analysis of the Hubbard model in the regime of strong correlations. DMFT as well as DQMC are for instance some of the leading technique that attracts a lot of attention for performing this analysis [29, 55].

DMFT is adapted to treat the strongly correlated regime of Hubbard model. It has notably explained the metal to Mott-insulator transition when tuning the interaction strength. It has also proved to be relevant in the study of ferromagnetism and disorder within the model [91]. Single-site DMFT considers one site in a sea of electrons and perform a mapping to the Anderson impurity problem [92, 93]. As a consequence the method is treating very well quantum fluctuations and dynamical effects, but has the drawback of being mostly local [94]. Several extensions of single-site DMFT have been suggested to answer this issue and are still an intensive topic of research, like Cluster-DMFT [95].

On the other hand, DQMC is an exact numerical method to solve the strongly correlated regime of the Hubbard model. However, due to the inherent complexity of Quantum Monte-Carlo for fermions because of the notorious sign problem, the main drawback of DQMC lies in its limitation with system size and temperature, as it have a $\mathcal{O}(\beta N^3)$ complexity [96], where N denotes the number of lattice site and β is the inverse of temperature. Despite this problem DQMC has predicted numerous results in the half-filled regime of Hubbard model where the sign problem can be avoided [97]. One could cite

the study of charge order and stripes [98], Luttinger theorem and Fermi surface [29] or magnetism [97]. Other famous strong coupling methods involved DMRG, or tensor networks, but these methods are also mostly limited by number of sites or complexity [99, 100].

We now shift our attention to the method that is going to be considered in this thesis. The composite operator technique, presented in Sec. 5 is a self-consistent framework developed from the Hubbard-II approximation. Compared to DMFT, this method treats and considers local corrections to the self-energy while also including dynamical corrections. Originally called two-poles approximation, it relies on the Hubbard operators and uses a decoupling scheme based on equation of motion developed by L. Roth [101]. This decoupling is used express two bodies correlators obtained from a truncation of the equation of motions. In the normal state, the metal to Mott-insulators transition upon doping is recovered and a good qualitative agreement is made with Monte-Carlo simulations [102]. Some early claims of Luttinger theorem violation have also been reported [102, 103]. In the vicinity of half-filling a transfer of spectral weight, typical of what is experimentally observed in Mott insulators has also been predicted by the method [102].

Superconductivity has also been considered and observed in the d-wave symmetry channel within the method [102, 104, 105]. In these works, a gap opens in the band structure and present the usual d-wave symmetry. The gap amplitude has also been reported as a function of Coulomb interaction and the critical temperature predicted to be in the range of 10 to 100 K in the regime of moderate electron interactions. This manuscript assume a paramagnetic order for simplicity. The different magnetic orders stabilized by the method has been summarized in a phase diagram in [106].

A few other models have been considered with composite operators such as the extended Hubbard model [105], attractive Hubbard models [107] or the Emery model [108].

3.4.2 . Motivations

The composite operators method have the notable drawback of violating Pauli principle. This violation is likely a consequence of the uncontrolled approximation made to truncate the equation of motions. While this violation is increasingly small as the Coulomb interaction is large, another self-consistent scheme has been suggested. Instead of using Roth decoupling to express the two-bodies correlators appearing in the self-consistency, these parameters are left to vary freely while the quantities that should have vanished due to Pauli principle are imposed to be zero as a self-consistent equation instead [103, 122, 141]. This second scheme, called "Pauli scheme" has been extensively studied in the last few years. Contrary to the initial "Roth scheme" it presents two self-consistent solutions [121]. One of them is not Mott insulators and does not present superconductivity, while the other does but displays two electron pockets at the Fermi energy. A higher order computation of the equation of motion allowed to show one of the two pockets has a vanishing lifetime [103].

Nowadays composite operators is a mostly unused method because of the respective drawbacks of each schemes. On one hand, there is the violation of Pauli principle with Roth scheme, on the other hand the Pauli scheme displays unconventional behaviors such as the two electron pockets in the Fermi surface, or the uncontrolled variation of the two-bodies self-consistent parameters. It is however a powerful method, as in allows to recover the bands, Fermi surface and the energy dependence while allowing to tune electron density, Coulomb repulsion (as long as it dominates over the hopping energy) and temperature as external parameters. In addition, contrary to DMFT it allows to

consider both dynamical and momentum corrections to the self-energy.

The first goal of this thesis is to compute, compare and discriminate the various schemes and solutions. To this end, we will compute the bands, Fermi surface, density of states of each solutions and also consider new quantities such as the area of the Fermi surface to better characterize Luttinger violation, particle-hole symmetry, an in depth study of the effect of each self-consistent parameters and superconductivity. We claim Roth solution is the rightful self-consistency to consider, as Pauli scheme presents a non self-consistent behavior and an uncontrolled variation of the two bodies parameters. We will then highlight the correlation between the Van Hove singularity in the density of states and superconductivity. Finally we will extend the method to perform a new study with longer ranged hopping to detail their effects on the solutions. As the Van Hove singularity is shifted away with the details of the tight-binding parameters, we report a shift of superconducting peak at the same density, confirming the correlation established with nearest-neighbors.

Once the method has been reviewed and clarified, the second objective is to consider a two orbital Hubbard model and check whether a spontaneous orbital symmetry breaking can be obtained with the composite operators approach without any Hund coupling involved in the Hamiltonian. An orbital selective Mott phase (OSMP) is displayed and characterized by computing the bands, the Fermi surface, the density of states, the quasi-particle weight as well as their orbitally resolved counterparts. A phase diagram summarize and details the transition seen between the orbitally uniform and the OSMP.

4 . Theoretical Tools

4.1 . Basic notions

4.1.1 . Second Quantization

In all the following, the framework of second quantization will be heavily used. In this section we give a small introduction of this formalism. In first quantization, states are described by wavefunctions living in a Hilbert space, and the system evolves in time according to the Schrödinger equation under the influence of a Hamiltonian. The eigenvalues of this Hamiltonian represent the energy levels of the system, while the eigenvectors correspond to the states of the system [109]. The probabilities of measuring specific outcomes are related to the squared eigenvectors associated to a specific eigenvalues. In the case of multiple systems, the Hilbert space is decomposed as a tensorial product of subspaces associated to each system. However, this formalism can become cumbersome, particularly when dealing with a large number of particles.

Second quantization aims at replacing this tensorial product picture by an empty/occupied states formalism. The two pictures are equivalents: the many-body state $|\Psi\rangle$ is composed of a complete basis of single particles states $\{|\nu_1\rangle, ..., |\nu_N\rangle\}$ where ν_u denotes the state of single particle u. Hence, the tensorial product of first quantization is replaced by the N-particles states:

$$|n_{\nu_1}, n_{\nu_2}, ..., n_{\nu_l}\rangle \text{ with } \sum_{u=1}^{l} n_{\nu_u} = N \tag{1}$$

In this picture, l denotes the number of considered states (which can be empty or not) and n_{ν_u} denotes the number of particles in state $|\nu_u\rangle$. We define the quantum operator $\hat{n}_{\nu_u}$ such that:

$$\hat{n}_{\nu_u}|n_{\nu_u}\rangle = n_{\nu_u}|n_{\nu_u}\rangle \tag{2}$$

Some important elements of second quantization are the operators $\hat{c}_u$ and $\hat{c}_u^\dagger$ that annihilates and creates respectively a particle on site u. They are related to $\hat{n}_u$ by the following :

$$\hat{n}_u = \hat{c}_u^\dagger \hat{c}_u \text{ and } \begin{cases} \hat{c}_u^\dagger|n_{\nu_u}\rangle & = |n_{\nu_u}+1\rangle \\ \hat{c}_u|n_{\nu_u}\rangle & = |n_{\nu_u}-1\rangle \end{cases} \tag{3}$$

Note that the eigenvalues of the annihilation operator $\hat{c}_u$ acting on an empty state are zero, meaning that $\hat{c}_u|0_u\rangle = 0$.

The operator $\hat{n}_u$ is a number operator associated with a specific single-particle state at site u. Importantly, $\hat{n}_u$ operates in the Fock space, a larger vector space that encompasses states with varying numbers of particles. The Fock space is constructed by taking the tensor product of the single-particle Hilbert spaces for each particle, providing a comprehensive framework for describing systems with multiple particles.

It is important to distinguish the operator $\hat{n}_u$ from the integer n_u that counts the number of particles occupying a particular state on site u. The quantum state $|n_u\rangle$ corresponds to a vector in the Fock space, specifically representing a configuration where n particles are on site u. In this context,

the Fock space captures the full quantum state of a system by considering all possible configurations of particles across different sites.

An equivalence can be built between the first and second quantization. The latter can be seen as a shift mathematical representations rather than a change in physical content. In first quantization, a quantum system is described by wavefunctions representing individual particles, while in second quantization, the focus shifts to an ensemble of single particle states defined by occupation numbers. The two pictures are therefore interchangeable.

The fermionic or bosonic nature of the considered particles is usually derived by exchanging the particles. This exchange can be directly encoded in the algebra by imposing anticommutation rules for fermions and commutation rules for bosons. The algebra of second quantization can be obtained by considering:

$$\{c_u, c_v^\dagger\}_\pm = \delta_{uv} \text{ and } \{c_u, c_v\}_\pm = \{c_u^\dagger, c_v^\dagger\}_\pm = 0 \tag{4}$$

Where $\{.,.\}_\pm$ is respectively a commutator for + and an anticommutator for -. The Pauli principle can be directly expressed from this algebra when fermions are considered. Indeed, from these commutation relations, $(c_i^\dagger)^2 = 0$, meaning that two fermions cannot exist in the same state. Finally, any n-body operator $\hat{O}$ can be rewritten in second quantization in term of creation and annihilation operators:

$$\hat{O} = \sum_{u_1,\dots,u_{2n}} O_{\nu_{u_1},\dots,\nu_{u_{2n}}} c_{\nu_{u_1}}^\dagger \dots c_{\nu_{u_n}}^\dagger c_{\nu_{u_{n+1}}} \dots c_{\nu_{u_{2n}}} \tag{5}$$

Where $O_{\nu_{u_1},\dots,\nu_{u_{2n}}}$ are the matrix elements of the operator $\hat{O}$. For the case of a one body parameter, we get:

$$\hat{O} = \sum_{uv} O_{uv} c_u^\dagger c_v = \sum_{uv} \langle u|\hat{O}|v\rangle c_u^\dagger c_v \tag{6}$$

In the following we will consider translational invariant systems in which we will heavily rely Fourier transforms. The Fourier transform of an operator c_i in second quantization is defined by:

$$c_k = \frac{1}{\sqrt{N}} \sum_u e^{ikr_u} c_u \tag{7}$$

Because of translational invariance of crystal lattice the momentum variable k will be considered in the Brillouin zone, which is the smallest unit cell one can consider to fully reconstruct momentum space by translations.

Second quantization proves particularly advantageous in solving condensed matter problems, providing a powerful tool for handling many-body systems. By transforming the Hamiltonian from the traditional first quantization form to its second quantized counterpart, expressed in terms of creation and annihilation operators, one gains a more convenient and efficient framework. This approach simplifies the treatment of systems with varying particle numbers and facilitates the derivation of quantum many-body theories. Second quantization enables a natural description of complex interactions and correlations within condensed matter systems.

4.1.2 . Green's function

Green's functions, also known as propagators, play a central role in the field of quantum many-body physics, providing a powerful tool for characterizing the response of a system to external perturbations. In essence, a Green's function in condensed matter can be understood as an object describing the response of a system under an excitation. It can be define for an arbitrary number n of particles n-points Green's functions, but in this manuscript we will mainly focus on the 2-points Green's function. Let us first consider operators in the Heisenberg representation: they are time-dependent operators $\psi(\tau)$ of a given Hilbert space such that:

$$\psi(x,t) = e^{i\hat{H}t}\psi(x,0)e^{-i\hat{H}t} \tag{8}$$

Where $\hat{H}$ is the Hamiltonian which define the time evolution of a system by means of the Schrodinger equation. As a direct consequence, we obtain the following result:

$$\frac{d\psi(t)}{dt} = [\psi(t), H] + i\frac{\partial\psi}{\partial t} \tag{9}$$

Where the second term account for the explicit dependence in time of ψ, and will be considered 0 (time independant operator) in the following. We can now define the causal 2-points Green's function [110] as follow

$$G^c_{uv}(t,t') = -i\langle T(c_u(t)c_v^\dagger(t'))\rangle = -i\langle\theta_H(t-t')c_u(t)c_v^\dagger(t') - \theta_H(t'-t)c_v^\dagger(t')c_u(t)\rangle \tag{10}$$

In this equation T is the time ordering operator and can be defined using heaviside function θ_H (we remind that $\theta_H(x) = 1$ if x is positive, and 0 otherwise). With this time ordering (or heaviside functions), the operator on the left always is at a later time than the one on the right. The subscripts u and v denotes two quantum numbers (for example, spin, momentum or lattice site). $\langle\hat{O}\rangle$ denotes the thermal expectation value, defined as

$$\langle\hat{O}\rangle = \frac{1}{Z}Tr(e^{-\beta H}\hat{O}) \tag{11}$$

Where $Z = Tr(e^{-\beta H})$ is the partition function. We can introduce the retarded and advanced Green's function, defined by :

$$\begin{cases} G^r_{uv}(t,t') &= -i\theta_H(t-t')\langle\{c_u(t), c_v^\dagger(t')\}\rangle \\ G^a_{uv}(t,t') &= i\theta_H(t'-t)\langle\{c_u(t), c_v^\dagger(t')\}\rangle \end{cases} \tag{12}$$

The retarded Green's function is the complex conjugate of the advanced one, and the causal Green's function can be rebuilt from the retarded and advanced Green's function. Even though they are all related, the retarded Green's function is usually the most considered because it is the most physical in condensed matter. Indeed, one can show from linear response theory [111] that this Green's function determine the linear response of the system to a perturbation. It makes sense, because the response of a system appears after a perturbation.

We now move on to the frequency domain to introduce the spectral representation. We consider first a non-interacting (ie separable) Hamiltonian such as

$$H = \sum_n \epsilon_n c_n^\dagger c_n \tag{13}$$

Computing the commutator of the operator c_n with the Hamiltonian (called the "current" of this operator) leads to the following equation of motion

$$\frac{dc_n(t)}{dt} = -i[c_n, H] = -i\epsilon_n c_n \tag{14}$$

This differential equation is solvable and one can get:

$$c_n(t) = e^{i\epsilon_n t} c_n(0) \tag{15}$$

Introducing this in the definition of the retarded Green's function leads to:

$$G^r_{nn'}(t-t') = -i\theta(t-t')e^{-i\epsilon_n(t-t')}\delta_{nn'} \tag{16}$$

Where we used $\{c_n, c_{n'}^\dagger\} = \delta_{nn'}$. We can now use the following property of the Heaviside step function:

$$\theta_H(t-t') = \frac{1}{2\pi i}\int_{-\infty}^{+\infty} d\omega \frac{e^{-\omega(t-t')}}{\omega + i0^+} \tag{17}$$

Introducing this in Eq. (16) leads with a bit of algebra to the non interacting Lehman representation:

$$G^r_{nn'}(\omega) = \sum_u \frac{\langle n|u\rangle\langle u|n'\rangle}{\omega - \epsilon_n + i0^+} \tag{18}$$

For a non-interacting system, two important physical properties are lying in this definition. First, the poles of the Green's function is directly corresponding to the eigenvalues of the system. Second, the imaginary part of the same site retarded Green's function, called spectral function A_{nn} is proportional to the local density of states:

$$\rho_n(\omega) = \mp\frac{1}{\pi} Im(G^r_{nn}(\omega)) = \mp\frac{1}{\pi} A^r_{nn}(\omega) \tag{19}$$

In the case of an interacting system we can still define and call $|m\rangle$ the eigenbasis for m electron, but the particle-hole excitation operator $c_n^\dagger/c_n$ removing or adding an electron at lattice site n will create a state $|m-1\rangle$ which is not anymore an eigenstate of the interacting hamiltonian. The Lehman representation of an interacting system thus takes the form:

$$G^R_{nn}(\omega) = \frac{1}{Z}\sum_{uv} \frac{|\langle u|c_n(0)|v\rangle|^2(e^{-\beta\epsilon_u} + e^{-\beta\epsilon_v})}{\omega - (\epsilon_v - \epsilon_u) + i0^+} \tag{20}$$

Where Z is the partition function of the system and β is inversely proportional to the temperature. In the non interacting case, the overlap element $|\langle u|c_n(0)|v\rangle|^2$ reduces to a Kronecker function and we recover the previously non-interacting Lehman representation of Eq. (18). The local density of states is now taking the form:

$$\rho_n(\omega) = \frac{1}{Z}\sum_{uv} |\langle u|c_n(0)|v\rangle|^2 (e^{-\beta\epsilon_u} + e^{-\beta\epsilon_v})\delta(\omega - (\epsilon_v - \epsilon_u)) \tag{21}$$

The $\frac{|\langle u|c_n(0)|v\rangle|^2(e^{-\beta\epsilon_u}+e^{-\beta\epsilon_v})}{Z}$ factor is often referred as the spectral weight and modify the density of states of interacting systems.

Let us finally mention imaginary time, defined as $\tau = it$ with t being real time. We can also define the Matsubara Green's function $G^M(\tau)$. This Green's function is often used because of the analytical continuation that can connect it to the retarded Green's function after a time-Fourier transform:

$$G^R_{nn'}(\omega) = \lim_{i\omega_n \to \omega + i0^+} G^M_{nn'}(i\omega_n) \tag{22}$$

4.1.3 . Tight-binding model

In this section, we show an example of the previously introduced tool on a well known condensed matter system: the tigh-binding model. The tight-binding Hamiltonian is a simple model, yet able to capture a lot of complex phenomenons (ref [112]). This model considers that each lattice sites of the total hamiltonian are described by an atomic hamiltonian with atomic orbitals of spatial extension usually assumed to vanish for distances larger than lattice spacing. The electrons are therefore tightly binded to atomic sites (explaining the name of the model). Electrons can tunnel from one atom to the other through overlapping of the orbitals. Therefore, the tight-binding model describes the kinetic energy of these localized electrons by means of hopping process from one lattice site to another. In second quantization, it is given by:

$$H = \sum_{ij} t_{ij}(c_i^\dagger c_j + c_j^\dagger c_i) \tag{23}$$

This Hamiltonian describes the destruction of an electron on one site i, and the creation of an electron on a neighboring site j effectively representing the process of an electron hopping from site i to j. t_{ij} is called the hopping parameter and is the energy cost of each hopping processes. It can take several values depending on the configuration if i and j. For example, it is standard to consider

$$\begin{cases} t_{ij} = 0 & \text{if i=j} \\ t_{ij} = -t & \text{if i and j are nearest-neighbours} \\ t_{ij} = t' & \text{if i and j are next-nearest neighbours} \end{cases} \tag{24}$$

The sign of t and t' can vary depending on the considered material. The more hopping parameter we consider, the more accurate it can describe the band structure of a material. These parameters can be fitted from experiments such as angular photo-emission spectroscopy (ARPES) [113]. We now Fourier transform this Hamiltonian using the rules defined in Sec. 4.1.1:

$$
\begin{aligned}
H &= \sum_{ij} \frac{t_{ij}}{N} \sum_{kk'} (e^{ikr_i} e^{-ik'r_j} c_k^\dagger c_{k'} + e^{-ikr_i} e^{ik'r_j} c_{k'}^\dagger c_k) \\
&= -t \sum_{kk'\delta} (\delta(k-k') e^{-ik'\delta} c_k^\dagger c_{k'} + \delta(k'-k) e^{ik'\delta} c_{k'}^\dagger c_k) + t' \sum_{kk'\delta'} (\delta(k-k') e^{-ik'\delta'} c_k^\dagger c_{k'} + \delta(k'-k) e^{ik'\delta'} c_{k'}^\dagger c_k) \\
&= \sum_k \epsilon_k c_k^\dagger c_k + \sum_k \epsilon'_k c_k^\dagger c_k
\end{aligned}
\tag{25}
$$

With δ and δ' running respectively on the nearest and next-nearest neighbours of site i, and ϵ_k and ϵ'_k the eigenvalues of the tight-binding model in momentum space, given by:

$$
\epsilon_k = -t \sum_\delta e^{-ik\delta} \quad \epsilon'_k = t' \sum_{\delta'} e^{-ik\delta'} \tag{26}
$$

The exact expression of ϵ_k and ϵ'_k depends on the symmetry of the considered lattice. For a square lattice, they are given by

$$
\epsilon_k = -2t(cos(k_x) + cos(k_y)) \quad \epsilon'_k = 4t' cos(k_x) cos(k_y) \tag{27}
$$

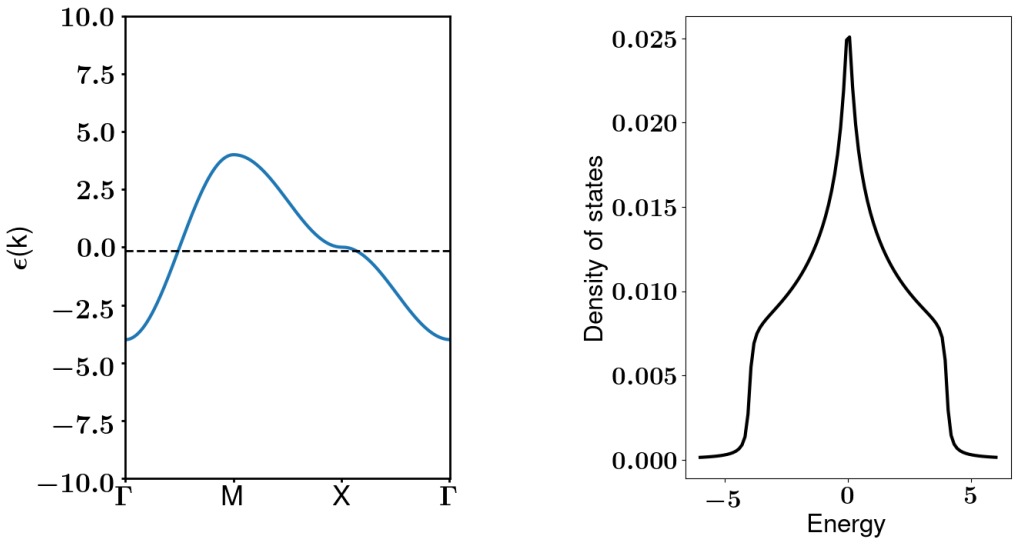

Figure 6: Bands along high symmetry points and density of states for the tight-binding model with t=1 and t'=0 for a square lattice. The high symmetry points for this lattice are $\Gamma = (0,0)$, $M = (\pi,\pi)$ and $X = (\pi,0)$. The chemical potential is computed from the Fermi-Dirac distribution at T=0K and n=0.9 (corresponding to 10% hole doping). Since the chemical potential at the level of the bands, this means that this system would be a conductor at this doping. The density of states presents a peak at $E = 0$. This corresponds to the energy where the band is flat (near k=X). This divergence of the density of states is called "Van Hove singularity".

In the case of a weakly interacting material, plotting the bands $\epsilon_k + \epsilon'_k$ can give information on the electrical conducting nature of the considered material. In the absence of excitation, under the chemical potential energy, the bands are filled, and they are empty above. The chemical potential μ can be considered by adding the following expression to the tight-binding Hamiltonian:

$$H_\mu = \mu \sum_i n_i \tag{28}$$

The value of μ can then be determined self consistently by fixing the total electron density of the system n, defined by

$$n = \frac{1}{N} \sum_{i=1}^{N} n_i \tag{29}$$

where N is the total number of site. In Fig. 6, we plot the bands of the tight-binding model for a square lattice from Eq. (27) at vanishing temperature with no t'. The dashed line is the chemical potential computed from the Fermi Dirac distribution with electron density n=0.9 which corresponds to 10% hole doping. At this density the chemical potential is lying inside the band. This means that in the ground-state at T=0K, all of the energies and momentum associated to the band for energy below the chemical potential are filled with electrons, and conversely the band is empty above the chemical potential. This also mean that a very small external electric field will create a current since electron can be excited with this small field and fill an empty energy state just above the chemical potential, the material is a conductor. If however, the chemical potential lies in between two bands, the external electric field to apply must be at least of the order of the gap between the bands in order to excite the electron from the band below the chemical potential to the empty band. The system is an insulator (or a semi-conductor if this gap is small).

We can also get the density of states by using:

$$\rho(E) = \frac{1}{N} \sum_k \delta(E - \epsilon_k - \epsilon'_k) \tag{30}$$

The dirac distribution can be computed numerically by approximating it to a Lorentzian with small broadening. The density of states corresponds to the number of states (filled or not) at a given energy. It is interesting to note the singularity around $E = 0$, called the "Van Hove singularity", and caused by the flatness of the band around this energy. If the band is flat, it means there are indeed a lot of momentum site available near this energy, creating effectively a singularity.

Let us finally note the same results can be recovered using Green's function formalism. Since the tight-binding model is a non-interacting system, from Eq. (18) we can extract $\epsilon_k + \epsilon'_k$ by considering the pole of the electronic Green's function, and the imaginary part turns out to give the same density of state as the one obtained by mean of Eq. 30

4.2 . The Hubbard model

4.2.1 . Description of the model and qualitative Hubbard I approximation

Introduced by Hubbard in 1963 [53], the Hubbard model has often been described as the simplest model one can build in order to capture the physics of strongly correlated material. The Hubbard Hamiltonian is as follow:

$$H = -\sum_{i,j\sigma} t_{ij}(c^{\dagger}_{i\sigma}c_{j\sigma} + hc) + U\sum_{i} n_{i\uparrow}n_{i\downarrow} - \mu\sum_{i\sigma} n_{i\sigma} \tag{31}$$

The first term acts as the kinetic energy of the electron : they are hopping from one site to another, this is simply the tight-binding Hamiltonian from sec. 4.1.3. The second term penalizes double occupancy by adding an energy cost U if two electrons are on the same site. The sign of the U term will decide whether the considered interaction is repulsive or attractive. The last term is the chemical potential and acts on the filling of the system, and usually fixed by the electron density. This model is exactly solvable in one dimension, and in infinite dimension [54] [114]. In two or three dimensions, it has remained unsolved for decades and is still a hot topic of the field of strong correlations [115].

One of the big success of this model in the strongly correlated limit is its ability to well describe the Mott-Insulator transition around half-filling [53]. Qualitatively the idea behind is that at half-filling, since there is only one electron per site, from a band picture the material should be a conductor because the band is not filled. However, hopping processes are blocked by the Coulomb repulsion U and the system is insulator.

To build the notorious picture of Hubbard bands to explain Mott insulators, we will first perform an heuristic derivation starting from the ground-state at half-filling inspired by ref. [57]. In that case, since the interaction is large, there can only be one electron per site. We will assume the system to be paramagnetic, thus there is as many spin up than spin down, in a disordered configuration. Now, let's assume an excitation is created by the hopping term: an electron moves to one of its neighboring sites to form a doubly occupied state, at a penalty cost in energy of U. This hopping can only occur if the electron of spin σ hops on a site with a spin $\bar{\sigma}$ electron. This has a probability $\frac{1}{2}$ to occur (paramagnetic assumption). This excitation creates a double occupied state $\eta_{i\sigma}$ at site i by adding an electron of spin σ to a site with an electron of spin $\bar{\sigma}$, therefore $\eta^{\dagger}_{i\sigma} = c^{\dagger}_{i\sigma}n_{i\bar{\sigma}}$. As a consequence, a hole is created from this hopping on a neighboring site j, since no electron of spin σ will be left on site j: $\xi_{j\bar{\sigma}} = c_{j\sigma}(1-n_{j\bar{\sigma}})$. The effective Hamiltonian resulting of this particle-hole excitation then takes the form:

$$H_{eff} = \frac{1}{2}\sum_{ij\sigma} t_{ij}(\eta^{\dagger}_{i\sigma}\xi^{\dagger}_{j\bar{\sigma}} + hc) + U\sum_{i\sigma}\eta^{\dagger}_{i\sigma}\eta_{i\sigma} \tag{32}$$

The first term describes the excitation of an electron forming a pair on site i and a hole on neighboring site j, and the second term is the energy penalty of U for the formation of such a pair.

Once a pair have been formed, its propagation will not have a considerable energy cost because this conserve the number of pairs and will not cost another penalty in energy of U. Assuming the electron of the pair conserve its spin, it can hop to another neighboring site of spin $\bar{\sigma}$ (which still has a probability $\frac{1}{2}$ due to the paramagnetic assumption). The hole can similarly propagate, leading to the following particle-hole hopping Hamiltonian:

$$H_{eff,2} = \frac{1}{2}\sum_{ij\sigma} t_{ij}(\eta^{\dagger}_{i\sigma}\eta_{j\sigma} - \xi^{\dagger}_{i\bar{\sigma}}\xi_{j\bar{\sigma}}) \tag{33}$$

The negative sign in front of the hole term is due to the fact that hole propagation is the opposite of electron propagation $t_{ij}c^{\dagger}_{j\sigma}c_{i\sigma}$. The global $\frac{1}{2}$ prefactor comes again from the paramagnetic condition. The full effective Hamiltonian, obtained from summing these two processes can be expressed in Fourier space.

$$H_{eff} = \sum_{k\sigma} \left((\frac{\epsilon_k}{2} + U)\eta^{\dagger}_{k\sigma}\eta_{k\sigma} - \frac{\epsilon_k}{2}\xi^{\dagger}_{k\sigma}\xi_{k\sigma} + \frac{\epsilon_k}{2}\eta^{\dagger}_{k\sigma}\xi_{k\sigma} + hc \right) \tag{34}$$

Where ϵ_k is the Fourier transform of the tight-binding hamiltonian and depends on the details of the considered lattice (refer to Sec. 4.1.3 for details). We now perform the following unitary transform to get the eigenvalues of the Hamiltonian:

$$\begin{cases} \alpha_{k\sigma} & = a_k\eta_{k\sigma} + b_k\xi^{\dagger}_{k\bar{\sigma}} \\ \beta_{k\sigma} & = -b_k\eta_{k\sigma} + a_k\xi^{\dagger}_{k\bar{\sigma}} \end{cases} \tag{35}$$

Where a_k and b_k are some complex numbers. A bit of algebra leads to the following form of the two eigenvalues of this effective Hamiltonian.

$$E^{(\pm)}_k = \frac{1}{2}\left(\epsilon_k + U \pm \sqrt{\epsilon_k^2 + U^2} \right) \tag{36}$$

In the large U limit this simplifies into $E^{-}_k = \frac{\epsilon_k}{2}$ and $E^{+}_k = \frac{\epsilon_k}{2} + U$, allowing to obtain this picture of lower and upper Hubbard bands. In the case of half-filling, the chemical potential will lie in between these bands. Since the Fermi energy is inside the gap, there are no available states for the electrons if a small electric field is applied. The system is then called a Mott insulator.

It is important to understand another approximation is being made in Hubbard I approximation. The energies we obtain are defined for the Hubbard operators. These operators do not commute the same way the electronic operators do. As a consequence, the bands should not be filled according to Fermi-Dirac distribution. However, by stating at half-filling the chemical potential is in between the energies, we are already assuming the Hubbard operators behaves as the electronic one. We will dwell on this approximation more in the next section.

4.2.2 . Rigorous Hubbard I derivation

We now build more rigorously the Hubbard I approximation the way it was historically introduced in 1963 by Hubbard. We introduce formally the two previously defined operator:

$$c_{i\sigma} = \eta_{i\sigma} + \xi_{i\sigma} \quad \text{with} \begin{cases} \eta_{i\sigma} & = c_{i\sigma}n_{i\bar{\sigma}} \\ \xi_{i\sigma} & = c_{i\sigma}(1 - n_{i\bar{\sigma}}) \end{cases} \tag{37}$$

These operators $\eta_{i\sigma}$ and $\xi_{i\sigma}$ are called "Hubbard operators". They present the following commutation relation (often referred as "currents") with the Hubbard Hamiltonian in the atomic limit ($t_{ij} = 0$):

$$\begin{cases} [\eta_{i\sigma}, H_{AL}] = -(\mu - U)\eta_{i\sigma} \\ [\xi_{i\sigma}, H_{AL}] = -\mu\xi_{i\sigma} \end{cases} \tag{38}$$

We now consider the hopping term as a small perturbation. The currents with the full Hubbard Hamiltonian becomes:

$$\begin{cases} [\xi_{i\sigma}, H] = & -\mu\xi_{i\sigma} - \sum_l t_{il}\left((1 - \langle n_{i\bar{\sigma}}\rangle)c_{l\sigma} - (n_{i\bar{\sigma}} - \langle n_{i\bar{\sigma}}\rangle)c_{l\sigma} + S_i^{sign(\bar{\sigma})}c_{l\bar{\sigma}} + sign(\bar{\sigma})\Delta_i c_{l\bar{\sigma}}^\dagger\right) \\ [\eta_{i\sigma}, H] = & -(\mu - U)\eta_{i\sigma} + \sum_l t_{il}\left(-\langle n_{i\bar{\sigma}}\rangle c_{l\sigma} - (n_{i\bar{\sigma}} - \langle n_{i\bar{\sigma}}\rangle)c_{l\sigma} + S_i^{sign(\bar{\sigma})}c_{l\bar{\sigma}} + sign(\bar{\sigma})\Delta_i c_{l\bar{\sigma}}^\dagger\right) \end{cases} \tag{39}$$

With $S_i^- = c_{i\downarrow}^\dagger c_{i\uparrow}$, $S_i^+ = c_{i\uparrow}^\dagger c_{i\downarrow}$ the spin operators and $\Delta_i = c_{i\uparrow}c_{i\downarrow}$ a pair operator. The charge operator n_i have been rewritten as $n_{i\bar{\sigma}} = n_{i\bar{\sigma}} + \langle n_{i\bar{\sigma}}\rangle - \langle n_{i\bar{\sigma}}\rangle$, introducing its expectation value to make a distinction between the averaged part (first term in the sum) and the fluctuation part (second term) of the charge channel. We take the following convention: $sign(\uparrow) = 1$ and $sign(\downarrow) = -1$. The contribution of the hopping term to the current can therefore be divided in three contribution: a charge excitation, a spin excitation and a pair excitation.

Hubbard I approximation neglects the spin and pair components as well as charge fluctuation and only retain the expectation value of the charge (first term in the sum) to only describe the simple propagation of a particle-hole excitation. In fact, the term neglected by this approximation are only terms that appears because the Hubbard operators are not commuting like the usual electronic ones. Indeed, we have:

$$\begin{cases} \{\xi_{i\sigma}, \xi_{i\sigma}^\dagger\} = 1 - n_{i\bar{\sigma}} \\ \{\eta_{i\sigma}, \eta_{i\sigma}^\dagger\} = n_{i\bar{\sigma}} \end{cases} \tag{40}$$

instead of the usual $\{c_{i\sigma}, c_{i\sigma}^\dagger\} = 1$. Thus, by neglecting these terms, the Hubbard I approximation implicitly assume the Hubbard operators are behaving exactly as usual electronic operators.

The currents under Hubbard I approximation then rewrite as:

$$\begin{cases} [\xi_{i\sigma}, H] \approx & -\mu\xi_{i\sigma} - (1 - \frac{n_i}{2})\sum_l t_{il}c_{l\sigma} \\ [\eta_{i\sigma}, H] \approx & -(\mu - U)\eta_{i\sigma} - \frac{n_i}{2}\sum_l t_{il}c_{l\sigma} \end{cases} \tag{41}$$

This approximation makes the problem solvable using operator while retaining partially the effect of the hopping term. We used the paramagnetic assumption to rewrite $\langle n_{i\bar{\sigma}}\rangle = \frac{n_i}{2}$. We can indeed use Hubbard operator to decompose the electronic operator and fully rewrite the current as a function of the Hubbard operators. In Fourier space, we obtain

$$\begin{pmatrix} [\xi_{k\sigma}, H] \\ [\eta_{k\sigma}, H] \end{pmatrix} = \begin{pmatrix} -\mu - (1 - \frac{n}{2})\epsilon_k & -(1 - \frac{n}{2})\epsilon_k \\ -\frac{n}{2}\epsilon_k & -(\mu - U) - \frac{n}{2}\epsilon_k \end{pmatrix} \begin{pmatrix} \xi_{k\sigma} \\ \eta_{k\sigma} \end{pmatrix} \tag{42}$$

In this equation ϵ_k is the Fourier transform of the hopping term and depends on the details of the lattice, and n is the averaged electron density.

Eq. (42) typically close the equation of motions of Green's function defined with Hubbard operators. Let us indeed consider the following Green's function:

$$S^{\alpha\beta}_{k\sigma}(\tau) = \theta_H(\tau)\langle\{\alpha_{k\sigma}(\tau), \beta^\dagger_{k\sigma}\}\rangle \tag{43}$$

Where α and β are Hubbard operators ($\in \{\xi_{k\sigma}, \eta_{k\sigma}\}$). The equation of motion of this equation is obtained by taking the time derivative. Using Heisenberg representation, this typically leads to the following equation:

$$\partial_\tau S^{\alpha\beta}_{k\sigma}(\tau) = \delta(\tau)\langle\{\alpha_{k\sigma}, \beta^\dagger_{k\sigma}\}\rangle + \theta_H(\tau)\langle\{[\alpha_{k\sigma}, H](\tau), \beta^\dagger_{k\sigma}\}\rangle \tag{44}$$

The anticommutator at the same time (with the dirac prefactor) can be exactly computed. We arrive at the following matricial equation, after a time Fourier transform:

$$\omega \begin{pmatrix} S^{\xi\xi}_{k\sigma} & S^{\xi\eta}_{k\sigma} \\ S^{\eta\xi}_{k\sigma} & S^{\eta\eta}_{k\sigma} \end{pmatrix} = \begin{pmatrix} 1-\frac{n}{2} & 0 \\ 0 & \frac{n}{2} \end{pmatrix} + \begin{pmatrix} -\mu-(1-\frac{n}{2})\epsilon_k & -(1-\frac{n}{2})\epsilon_k \\ -\frac{n}{2}\epsilon_k & -(\mu-U)-\frac{n}{2}\epsilon_k \end{pmatrix} \begin{pmatrix} S^{\xi\xi}_{k\sigma} & S^{\xi\eta}_{k\sigma} \\ S^{\eta\xi}_{k\sigma} & S^{\eta\eta}_{k\sigma} \end{pmatrix} \tag{45}$$

The first matrix corresponds to the dirac term in the equation of motion computed explicitly. To reconstruct the Hubbard Green's function on the right hand side we used $[\xi_{k\sigma}, H](\omega) \propto \xi_{k\sigma}(\omega)$. This matricial system can be solved. We can then use the relation between electronic and Hubbard operators $c_{i\sigma} = \xi_{i\sigma} + \eta_{i\sigma}$ to reconstruct the electronic Green's function $G_{k\sigma}(\tau) = \theta_H(\tau)\langle\{c_{k\sigma}(\tau), c^\dagger_{k\sigma}\}\rangle$ by summing the four Hubbard Green's function. We arrive at the following expression:

$$G_{k\sigma}(\tau) = \frac{1}{\omega + \mu + \epsilon_k + \Sigma_k(\omega)} \tag{46}$$

With $\Sigma_k(\omega)$ the self-energy given by:

$$\Sigma_k(\omega) = \frac{nU(\mu+\omega)}{(n-2)U + 2(\mu+\omega)} \tag{47}$$

The electronic Green's function can be rewritten in a more meaningful way by decomposing it as:

$$G_{k\sigma}(\tau) = \frac{Z^+_k}{\omega - E^+_k} + \frac{Z^-_k}{\omega - E^-_k} \tag{48}$$

With :

$$Z^\pm_k = \frac{1}{2}(1 \mp \frac{\epsilon_k + (1-n)U}{W_k}) \text{ and } E^\pm_k = \frac{1}{2}(U - \epsilon_k \pm W_k) - \mu \tag{49}$$

Where $W_k = \sqrt{U^2 + \epsilon_k^2 + 2(1-n)U\epsilon_k}$. With this latter form, it is clear that G presents two poles associated to $E^\pm_k$. $Z^\pm_k$ are the spectral weight (introduced qualitatively in Sec. 3.1.2) and renormalize

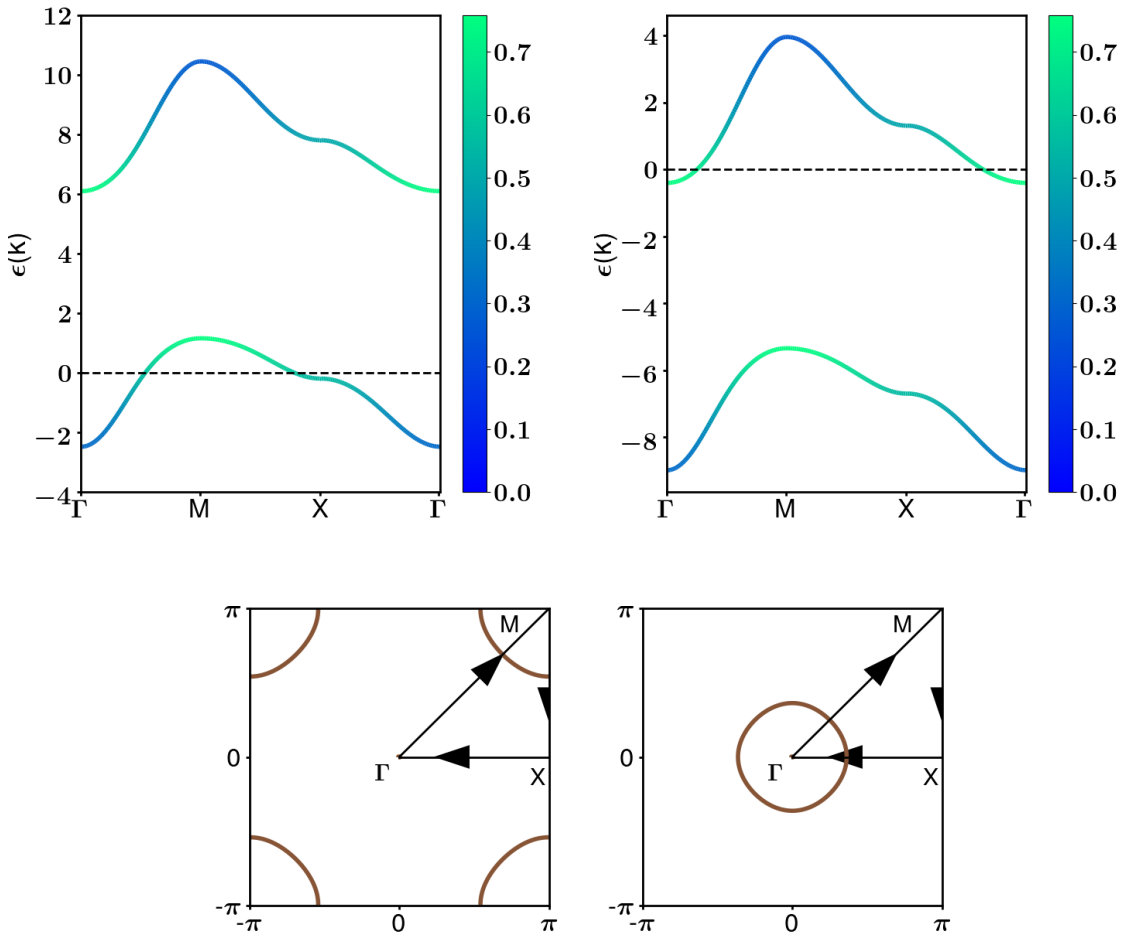

Figure 7: Bands (top) and Fermi surface (bottom) obtained with Hubbard I approximation at U=8t, t=1, (left) n=0.8, (right) n=1.1. The colors of the bands correspond to the spectral weight Z_k broadened by some small imaginary lifetime. The two poles of the electronic Green's function under Hubbard I approximation corresponds to the lower (E_k^-) and upper (E_k^+) Hubbard bands. When hole doped (n smaller than 1, left hand plots), the Fermi energy lies at the lower Hubbard bands. At half-filling, a jump of chemical potential occurs so that the upper Hubbard band gets filled when electron doped (n bigger than 1).

these two lower and upper Hubbard bands respectively. At half-filling (corresponding to setting n=1) we recover the qualitative derivation from Eq. (36), up to a sign convention on t. This form is reminiscent of the Green's function of a Fermi liquid theory, but there are two different quasi-particles weights associated to the two Hubbard bands and the fractionalization of the electronic operator in the two Hubbard operators. So while this is not a Fermi liquid anymore, Hubbard I approximation leads to a "correlated" Fermi liquid. The electronic Green's function appears as the sum of two Fermi liquids, with two quasi-particles, which are assumed to behave like the electronic operators in Hub-

bard I approximation.

In fig 7, we plot the bands $E_k^{\pm}$ and their spectral weight $Z_k^{\pm}$ at two different doping for a square lattice (therefore $\epsilon_k = 2t(cos(k_x) + cos(k_y))$, along with the associated Fermi Surface. The chemical potential is computed by mean of the Fermi Dirac distribution, since the Hubbard operators are assumed to have the same statistic as normal fermions. We observe a gap of the order of U (since $W_k \approx U$ if $U \gg t$) between the two bands. When moving from hole to electron doping (from n$\langle 1$ to n$\rangle 1$), the chemical potential jumps from the lower to the upper Hubbard band. Therefore, at half-filling the Hubbard I approximation describes the Mott-Insulator phase well since the chemical potential would lie in between the bands. The spectral weight is given by the color of the bands and will be discussed in Sec. 5.2.1. Let us finally note the Fermi surfaces can be extracted directly from the spectral function. We represent on fig. 7 the Fermi contour, given by the equation $E_k^{\pm} = 0$.

4.2.3 . Luttinger theorem and its breakdown with Hubbard-I approximation

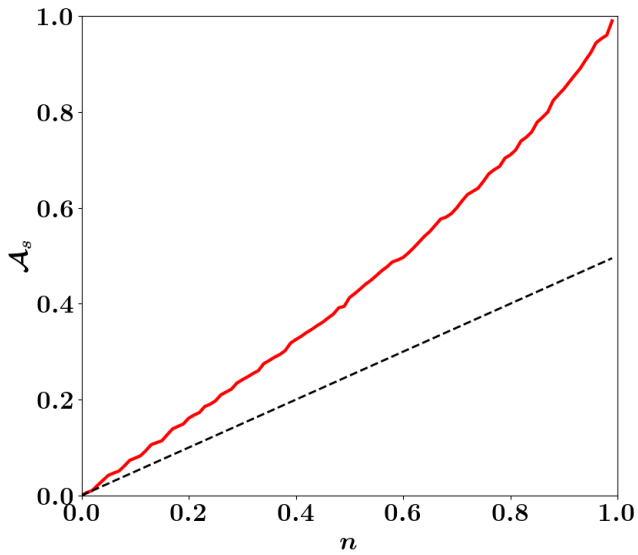

Figure 8: Area of the Fermi surface $\mathcal{A}_s$ represented as a function of the electron density n with Hubbard I approximation. The chemical potential is computed by mean of the Fermi Dirac distribution. A violation of Luttinger theorem (dashed-line) is observed at every doping.

As discussed in sec. 3.1.3, Luttinger theorem has broaden the Fermi gas concept of Fermi sea to the case of interacting fermions using adiabaticity. It states that the volume enclosed by the Fermi surface is invariant under interaction and is equal to the total number of fermions. This theorem is fundamental in the description of Fermi liquid theory (cf Sec. 3.1.2).

The range of validity of the theorem is however very debated, especially the requirements on the self-energy for the theorem to hold. This implies that Landau adiabatic assumption is not always adapted for some systems. Few references even make a distinction between the "hard" version of Luttinger theorem we just mentioned, and a "soft" version where the invariance with respect to interaction is lost [116]. Nevertheless, there is now a consensus that a necessary and sufficient condition

for the "hard" Luttinger theorem to hold is that the low energy excitation of the considered theory should be described by a Fermi liquid [26].

Even though Hubbard-I approximation can somewhat describe a "correlated" Fermi liquid as explained in Sec. 4.2.2, fig 8 shows Luttinger theorem is not verified. The reason is that there are two types of quasi-particles involved, the Hubbard operators, that are correlated (since in order to reconstruct the electronic Green's function they need to be summed). In addition, since Hubbard I wrongly assume these quasi-particle excitations behaves as normal Fermions, the real filling of these two lower and upper Hubbard bands is not described by a Fermi-Dirac distribution and causes Luttinger theorem to be even less likely to hold [116].

The composite operator scheme we will introduce in the next section goes beyond Hubbard-I approximation by correctly taking into account the non-electronic nature of the Hubbard operators and fixing the chemical potential and the filling of the bands accordingly.

4.3 . Kondo physics

4.3.1 . Kondo physics qualitatively

Kondo physics is a rich and broad topic, and is still nowadays an intensive research subject. In this section we only aim at providing a light introduction of the Kondo model in order to build an analogy for the orbital selective phase discussed in Sec. 6.

We consider a lattice of conduction electrons $c_{i\sigma}$ described by a tight-binding model of dispersion ϵ_k and nearest-neighbor hopping parameter t. The lattice is coupled at site 0 to a local impurity d_σ with a coupling constant λ. Strong interaction U_d are imposed on the impurity site to penalize double occupancy. The chemical potential of the impurity is given by ϵ_d. The situation is sketched for the one dimensional case on Fig 9.

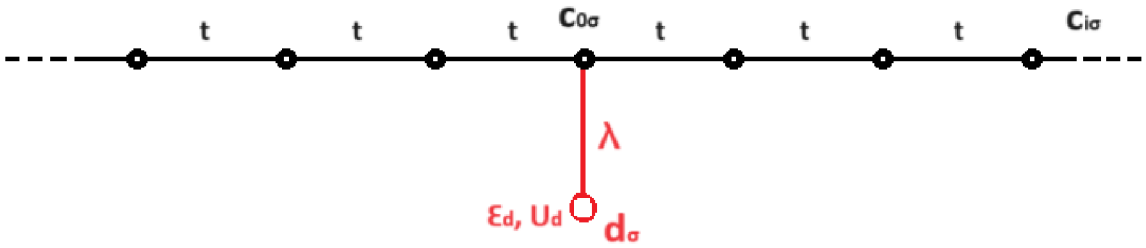

Figure 9: Sketch of the Anderson impurity model in 1D. A lattice of conduction electrons $c_{i\sigma}$ is coupled at site 0 with an impurity. The conduction sites can hop on nearest-neighbors sites with energy t. The impurity is coupled to the conduction lattice through the constant λ. The impurity site has chemical potential ϵ_d and is strongly interacting, making the formation of pairs on the impurity site penalized in energy by U_d.

The Hamiltonian used to describe this system is called the Anderson impurity model:

$$\begin{cases} H_{AI} & = H_{RLM} + U_d d^\dagger_\uparrow d_\uparrow d^\dagger_\downarrow d_\downarrow \\ H_{RLM} & = \sum_{k\sigma} \epsilon_k c^\dagger_{k\sigma} c_{k\sigma} + \sum_\sigma \left[\epsilon_d d^\dagger_\sigma d_\sigma - \lambda (d^\dagger_\sigma c_{0\sigma} + hc) \right] \end{cases} \tag{50}$$

H_{RLM} is called the resonant level model and exhibit a Fermi liquid behavior .The Kondo model is directly derived from the Anderson impurity model under a Schrieffer-Wolff transformation. For conciseness we will not give details of this transformation in this manuscript, but the derivation is presented in ref [117]. The Kondo Hamiltonian is given by:

$$H_K = \sum_k \epsilon_k c^\dagger_{k\sigma} c_{k\sigma} + J_K \mathbf{S}_d \cdot \mathbf{S}_c \tag{51}$$

With $\mathbf{S}_d$ a $\frac{1}{2}$ spin acting on the impurity and $\mathbf{S}_c$ the spin operator for the conduction electron, defined by:

$$S_c = \frac{1}{N} \sum_{kk'uv} c^\dagger_{ku} \frac{\sigma_{uv}}{2} c_{k'v} \tag{52}$$

With σ the Pauli matrices and J_K the exchange interaction and is given in term of Anderson impurity model parameters by:

$$J_K = 2\lambda^2 \left(-\frac{1}{\epsilon_d} + \frac{1}{\epsilon_d + U_d} \right) \tag{53}$$

The Kondo model is a mapping of the Anderson impurity problem to an interacting spin picture. This model is at the core of a rich and still debated physics. It is known for providing a good explanation to the Kondo effect, a rise of resistivity at very low temperature past a local minimum [118].

In Kondo physics, a relevant energy scale is the Kondo temperature T_K. This temperature is such that for $T_K \gg T$ the system behaves like a Fermi liquid and there is hybridization between the impurity and the conduction electron. On the other limit $T \gg T_K$, the impurity is not hybridize with the conduction electron and is local.

A renormalization group approach [17] can be used to show that T_K varies in $e^{-\frac{1}{J_K}}$. Therefore, T_K decreases as U_d gets stronger.

4.3.2 . Heavy Fermions and enlarged Fermi surface

We now consider a situation closer than what will be studied in the following: instead of a single impurity as described in Fig. 9, the system is now a lattice of impurities coupled to the lattice of conduction electrons, with a coupling constant λ at each site of the two lattices. The Anderson impurity lattice model now takes the following form:

$$H_{AIL} = \sum_k \left(\epsilon_k c^\dagger_{k\sigma} c_{k\sigma} + \epsilon^d_k d^\dagger_{k\sigma} d_{k\sigma} \right) + \sum_i \left(-\lambda (d^\dagger_{i\sigma} c_{i\sigma} + c^\dagger_{i\sigma} d_{i\sigma}) + U_d d^\dagger_{i\uparrow} d_{i\uparrow} d^\dagger_{i\downarrow} d_{i\downarrow} \right) \tag{54}$$

With ϵ_k^d the hopping in the impurity lattice. A Schrieffer-Wolff transformation in the $U_d \gg \lambda, \epsilon_k, \epsilon_k^d$ limit (so that the impurity lattice is at half-filling) leads once again to the Kondo-lattice model.

$$H_{KL} = \sum_k \epsilon_k c_{k\sigma}^\dagger c_{k\sigma} + J_K \sum_i \mathbf{S}_i^d \cdot \mathbf{S}_i^c \tag{55}$$

With J_k the exchange interaction, S_i^d a spin $\frac{1}{2}$ operator acting on site i of the impurity lattice and $S_i^c = \frac{1}{2} c_{iu}^\dagger \sigma_{uv} c_{iv}$. A Heisenberg Hamiltonian will also appear from the transformation but we do not consider it in this section.

We want to derive using a mean field approach an important property of such system to deepen the analogy with our observations in the two orbital Hubbard model. Namely, we want to prove in the strong correlations regime that the Fermi surface enclosed volume is enlarged due to hybridization between the conduction and impurities lattice. Using the spin representation, we can rewrite $\mathbf{S}^d$ as:

$$\mathbf{S}_i^d = f_{i\alpha}^\dagger \frac{\sigma_{\alpha\beta}}{2} f_{i\beta} \tag{56}$$

Where $f_{i\sigma}$ is a fermionic spinon and we enforce the strong correlation on the impurity lattice by mean of a Lagrange multiplier L to impose $f_{i\sigma}^\dagger f_{i\sigma} = 1$. Therefore, we perform a mean field decoupling by introducing the following parameters:

$$\begin{aligned} \mathcal{P} &= \frac{J_K}{N} \sum_k \langle f_{k\sigma}^\dagger f_{k\sigma} \rangle \\ \frac{1}{2} &= \frac{1}{N} \sum_k \langle f_{k\sigma}^\dagger f_{k\sigma} \rangle \\ \frac{n_c}{2} &= \frac{1}{N} \sum_k \langle c_{k\sigma}^\dagger c_{k\sigma} \rangle \end{aligned} \tag{57}$$

The $\frac{1}{2}$ factors are due to spin degenaracy. The first equation introduces the hybridization mean-field parameter. Second equation fixes the constraint on the spinons $f_{k\sigma}$, while third equation is used to fix the total electron density n_c. We first rewrite the Kondo-lattice model using the following relation on Pauli matrices:

$$\sigma_{\alpha\beta}\sigma_{\alpha'\beta'} = 2\delta_{\alpha\beta'}\delta_{\beta\alpha'} - \delta_{\alpha\beta}\delta_{\alpha'\beta'} \tag{58}$$

We arrive at the following form:

$$H_{KL} = \sum_k \epsilon_k c_{k\sigma}^\dagger c_{k\sigma} + \frac{J_K}{4} \sum_k \left(2 f_{k\sigma}^\dagger c_{k\sigma} c_{k\sigma'}^\dagger f_{k\sigma'} - f_{k\sigma}^\dagger f_{k\sigma} c_{k\sigma'}^\dagger c_{k\sigma'} \right) + L \sum_k f_{k\sigma}^\dagger f_{k\sigma} \tag{59}$$

The second term of the exchange term is just a shift to the chemical potential since one can apply $f_{k\sigma}^\dagger f_{k\sigma} = 1$. We now perform a mean-field decoupling of the first term:

$$f_{k\sigma}^\dagger c_{k\sigma} c_{k\sigma'}^\dagger f_{k\sigma} \approx \mathcal{P} c_{k\sigma'}^\dagger f_{k\sigma'} + \mathcal{P}^* f_{k\sigma}^\dagger c_{k\sigma} - |\mathcal{P}|^2 \tag{60}$$

Therefore the Kondo-lattice model rewrite in mean field as:

$$H_{KL}^{MF} \approx \sum_k (\epsilon_k c_{k\sigma}^\dagger c_{k\sigma} - \mathcal{P} f_{k\sigma}^\dagger c_{k\sigma} - \mathcal{P}^* c_{k\sigma}^\dagger f_{k\sigma}) + L \sum_k f_{k\sigma}^\dagger f_{k\sigma} - L\frac{N}{2} + \frac{|\mathcal{P}|^2 N}{J_k} \tag{61}$$

This Hamiltonian can be rewritten in the Nambu spinor $(c_{k\sigma} \quad f_{k\sigma})^T$, and diagonalizing it leads to the following eigenvalues:

$$E^{\pm} = \frac{\epsilon_k + L \pm \sqrt{(\epsilon_k - L)^2 + 4|\mathcal{P}|^2}}{2} \tag{62}$$

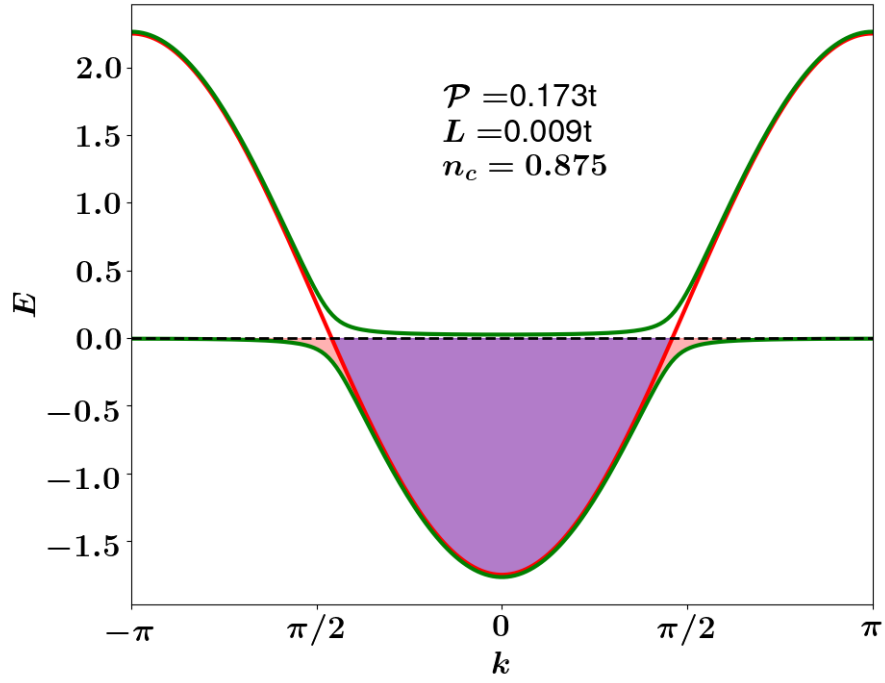

Figure 10: Dispersion of the 1D tight-binding model with $n_c = 0.875$ (red). In green the mean-field eigenvalues of the Kondo-lattice model are plotted. The parameters $\mathcal{P}$, L as well as the chemical potential have been computed self-consistently for an electron density $n_c = 0.875$. The red and the purple area represents the filled states of the mean-field Kondo lattice model, while the purple states are the one of the tight-binding. The Fermi momentum k_f is bigger for the Kondo lattice, resulting in an enlarged Fermi surface caused by hybridization.

The parameters L and $\mathcal{P}$ as well as the chemical potential can then be determined self-consistently by imposing Eq. 59. In Fig 10, we plot the tight-binding dispersion ϵ_k for the conducting electrons as well as $E^{\pm}$. For a non-zero $\mathcal{P}$ the enclosed volume by the Fermi surface is bigger than without hybridization. Therefore, a signature of hybridization is an enlargement of the Fermi surface.

4.3.3 . The competition of antiferromagnetism and hybridization

We now consider the effect of the Heisenberg term neglected in the previous section. This term is known to create anti-ferromagnetic or ferromagnetic order depending on the value of the exchange constant. In the case of the Kondo-Heisenberg model, the constant is known to be positive and therefore stabilize an anti-ferromagnetic order [119].

A competition between this order and hybridization is to be expected. Indeed, hybridization tends to favor electron delocalization, since it involves hopping processes between the impurity lattice and the conduction electrons. As a consequence, some effects such as spin flip or pairs or holes can arise from hybridization, effectively destroying the anti-ferromagnetic ordering. This competition has been extensively studied [120], and we won't give any details in this section as we will just build an analogy with this competition later on in Sec. 6.

5 . The Composite operators method

The composite operators method (COM) consists in introducing a specific set of operators in order to study a Hamiltonian in some particular regime where some terms can be neglected in the currents. In the following we will mainly focus on the Hubbard model. The composite operators we consider here are the same as the previously defined Hubbard operators. After introducing the method, we will study the Mott-insulator transition, and extend the method to superconductivity, longer-range hopping and sublattice (with the application to a 2 orbital Hubbard model with an inter-orbital hopping term).

5.1 . General framework

Starting from the one orbital Hubbard model Eq. (31), we introduce the following Hubbard operators, that exactly solve the equation of motion of the electronic Green's function in the atomic limit:

$$\psi_{i\sigma} = \begin{pmatrix} \xi_{i\sigma} \\ \eta_{i\sigma} \end{pmatrix} \quad \text{with} \quad \begin{cases} \xi_{i\sigma} = c_{i\sigma} - c_{i\sigma} n_{i\bar{\sigma}} \\ \eta_{i\sigma} = c_{i\sigma} n_{i\bar{\sigma}} \end{cases} \tag{63}$$

Where $\bar{\sigma}$ means we take a spin $\uparrow$ if $\sigma = \downarrow$ and a spin $\uparrow$ if $\sigma = \downarrow$. Hereafter, $\psi^1_{i\sigma} = \xi_{i\sigma}$ and $\psi^2_{i\sigma} = \eta_{i\sigma}$ denotes the first and second component of the spinor at site i and with spin σ. Before detailing how this set of composite operators solve the equation of motion in the atomic limit, we want to provide some physical interpretation to these operators. Let us consider a site i_0 and study the effects of $\xi_{i_0\sigma}$ and $\eta_{i_0\sigma}$. We obtain the following:

$$\begin{aligned} \xi_{i_0\sigma}|\uparrow\downarrow\rangle_{i_0} &= 0 & \eta_{i_0\sigma}|\uparrow\downarrow\rangle_{i_0} &= |\bar{\sigma}\rangle_{i_0} \\ \xi_{i_0\sigma}|\sigma\rangle_{i_0} &= |0\rangle_{i_0} & \eta_{i_0\sigma}|\sigma\rangle_{i_0} &= 0 \\ \xi_{i_0\sigma}|\bar{\sigma}\rangle_{i_0} &= 0 & \eta_{i_0\sigma}|\bar{\sigma}\rangle_{i_0} &= 0 \\ \xi_{i_0\sigma}|0\rangle_{i_0} &= 0 & \eta_{i_0\sigma}|0\rangle_{i_0} &= 0 \end{aligned} \tag{64}$$

These operators differ from the usual electronic operators, and will only affect specific site configurations. One can see the ξ_σ operator is going to act on the transition from an empty state to a single occupied site with spin σ. On the other hand, η_σ is a transforming a double occupied state to a single occupied state of spin $\bar{\sigma}$. The η_σ operator is therefore expected to be particularly important to treat the electron interaction terms.

5.1.1 . Atomic limit study

In the atomic limit, we do not consider hopping term t. The Hamiltonian is now local (each site is independent, and we can consider a site independent model) and is given by

$$H_{loc} = U \sum_i n_{i\uparrow} n_{i\downarrow} - \mu \sum_{i\sigma} n_{i\sigma} \tag{65}$$

Since the hamiltonian is now local, we can fix the consider site and work with the following hamiltonian:

$$H_{loc} = U n_\uparrow n_\downarrow - \mu(n_\downarrow + n_\uparrow) \tag{66}$$

The composite operator basis ψ can also be defined as site independant in the atomic limit:

$$\psi_\sigma = \begin{pmatrix} \xi_\uparrow \\ \eta_\uparrow \end{pmatrix} = \begin{pmatrix} c_\uparrow - c_\uparrow n_\downarrow \\ c_\uparrow n_\downarrow \end{pmatrix} \tag{67}$$

Let us start by introducing the 2×2 matrix composed of composite Green's function, with spins σ and σ' and defined for Matsubara times τ and τ' by decomposing the electronic Green's function

$$\begin{cases} G^{loc}_{\sigma\sigma'}(\tau,\tau') & = \langle\langle c_\sigma(\tau); c'_\sigma(\tau')\rangle\rangle = (S^{11}_{\sigma\sigma'})^{loc}(\tau,\tau') + (S^{12}_{\sigma\sigma'})^{loc}(\tau,\tau') + (S^{21}_{\sigma\sigma'})^{loc}(\tau,\tau') + (S^{22}_{\sigma\sigma'})^{loc}(\tau,\tau') \\ (\mathbf{S}^{nm}_{\sigma\sigma'})^{loc}(\tau,\tau') & = \langle\langle \psi^n_\sigma(\tau); (\psi^m_{\sigma'})^\dagger(\tau')\rangle\rangle_{loc} \end{cases} \tag{68}$$

Where, for two operators X and Y the double bracket notation is such that

$$\langle\langle X(\tau); Y(\tau')\rangle\rangle_{loc} = \theta_H(\tau - \tau')\langle\{X(\tau); Y(\tau')\}\rangle_{loc} \tag{69}$$

$\theta_H(\tau - \tau')$ is one if $\tau > \tau'$ and zero otherwise (Heaviside function). $\langle ... \rangle_{loc}$ denotes the thermal average (cf Eq. 11) taken with the Hamiltonian H_{loc} and $\{X(\tau); Y(\tau')\}$ is the anticommutator of X and Y. Since we are at thermal equilibrium we have $\mathbf{S}^{loc}_{\sigma\sigma'}(\tau,\tau') = \mathbf{S}^{loc}_{\sigma\sigma'}(\tau - \tau')$. From now on we fix τ' to zero as a choice of the origin of Matsubara time.

Eq. 68 has been obtained by decomposing the electronic operator in the definition of the Green's function: $c_\sigma = \xi_\sigma + \eta_\sigma$. We will now write in bold matrices in the ψ vector, and the superscript index will denotes the elements of these matrices. By differentiating with respect to τ the composite Green's function matrix, we get the following equations of motion

$$\frac{d}{d\tau}\mathbf{S}^{loc}_{\sigma\sigma'}(\tau) = \delta(\tau)\delta_{\sigma\sigma'}\langle\{\psi_\sigma(\tau); \psi^\dagger_\sigma(0)\}\rangle_{loc} + \delta_{\sigma\sigma'}\langle\langle[\psi_\sigma(\tau); H_{loc}]; \psi^\dagger_\sigma(0)\rangle\rangle_{loc} \tag{70}$$

Where $[A; B]$ is the usual commutator between two operators A and B. This commutator appears by considering the Heisenberg representation and by derivating it with respect to time.

For simplification purposes, we enforce a para-magnetic solution by adding $\delta_{\sigma\sigma'}$ prefactor, meaning that in the following the results remain unchanged whether we consider an up or a down spin for σ. The currents in the atomic limit are given by

$$J^{loc}_\sigma(\tau) = \frac{d}{d\tau}\psi_\sigma(\tau) = [\psi_\sigma(\tau); H_{loc}] = \mathbf{A}\psi_\sigma(\tau) \tag{71}$$

With

$$\mathbf{A} = \begin{pmatrix} \mu & 0 \\ 0 & U - \mu \end{pmatrix} \tag{72}$$

The equations of motion become

$$\frac{d}{d\tau}\mathbf{S}^{loc}_{\sigma\sigma'}(\tau) = \delta(\tau)\delta_{\sigma\sigma'}\langle\{\psi_\sigma(\tau);\psi^\dagger_\sigma(0)\}\rangle_{loc} + \mathbf{A}\,\mathbf{S}^{loc}_{\sigma\sigma'}(\tau) \tag{73}$$

By time Fourier transform we get

$$\mathbf{S}^{loc}_{\sigma\sigma'}(\omega) = \delta_{\sigma\sigma'}(\omega - \mathbf{A} + i0^+)^{-1}\mathbf{I}^{loc}_\sigma \tag{74}$$

With $\mathbf{I}^{loc}_\sigma = \langle\{\psi_\sigma;\psi^\dagger_\sigma\}\rangle_{loc}$ the normalization matrix. It is worth noting that the **I** matrix corresponds to the composite Green's function at equal time. 0^+ is a small positive parameter used for analytic continuation. This **I** matrix can be explicitly computed. A bit of algebra leads to

$$\mathbf{I}^{loc}_\sigma = \begin{pmatrix} 1-\langle n_\sigma\rangle_{loc} & 0 \\ 0 & \langle n_\sigma\rangle_{loc}\end{pmatrix} \tag{75}$$

We finally obtain

$$\mathbf{S}^{loc}_{\sigma\sigma}(\omega) = \delta_{\sigma\sigma'}\begin{pmatrix} \frac{1-\langle n_\sigma\rangle_{loc}}{\omega-\mu+i0^+} & 0 \\ 0 & \frac{\langle n_\sigma\rangle_{loc}}{\omega-U+\mu+i0^+}\end{pmatrix} \tag{76}$$

Finally, by Eq. 68, we can deduce the electronic Green's function

$$\begin{aligned} G^{loc}_{\sigma\sigma'}(\tau) =& \delta_{\sigma\sigma'}\langle\langle c_\sigma(\tau); c^\dagger_{\sigma'}\rangle\rangle_{loc} \\ =& \delta_{\sigma\sigma'}(S^{11\ loc}_\sigma(\tau) + S^{12\ loc}_\sigma(\tau) + S^{21\ loc}_\sigma(\tau) + S^{22\ loc}_\sigma(\tau)) \\ =& \frac{1-\langle n_\sigma\rangle_{loc}}{\omega-\mu+i0^+} + \frac{\langle n_\sigma\rangle_{loc}}{\omega-U-\mu+i0^+} \end{aligned} \tag{77}$$

Where $S^{nm\ loc}_\sigma = \langle\langle\psi^n_\sigma(\tau);\psi^m_\sigma(0)\rangle\rangle_{loc}$ denotes the (n,m) element of the 2x2 composite Green's function matrix. Therefore we have showed that the composite operators we introduced solve exactly the atomic limit. The electronic Green's function can be directly recovered.

At this level it is important to observe the connection with the lower and upper Hubbard bands picture we already introduced with Hubbard I approximation. Indeed, this electronic Green's function has two poles at $\omega = \mu$ and $\omega = \mu + U$. They both corresponds to flat bands (since there is no hopping or terms that introduce a k-dependency, the system is local). These two bands are separated by U. When turning on the hopping term as a perturbation, we can expect this two bands picture to remain slightly similar, although momentum dependant. This is in agreement with what we have seen in Sec. 4.2.2: the atomic limit picture is the precursor of the Hubbard bands.

5.1.2 . Composite operators approximation

Let us now consider the full Hamiltonian Eq. (31) that includes both the local term H_{loc} and the hopping term t. We consider the limit where $U \gg t$. Let's consider the effect of the hopping term on the current δJ, define as:

$$\delta J_{i\sigma} = [\psi_{i\sigma}, H - H_{loc}] = J_{i\sigma} - J^{loc}_{i\sigma} \tag{78}$$

Where the current operator in the atomic limit $J^{loc}_{i\sigma}$ is given by Eq. (71) and $J_{i\sigma} = [\psi_{i\sigma}, H]$ is the current operator taken with the full Hubbard Hamiltonian Eq. (31). Therefore, $\delta J_{i\sigma}$ is the current associated to the hopping term. Let's introduce the composite Green's function, now site dependent by:

$$\mathbf{S}_{ij\sigma\sigma'}(\tau) = \theta_H(\tau)\langle\{\psi_{i\sigma}(\tau); \psi^\dagger_{j\sigma'}\}\rangle \tag{79}$$

From now on, $\langle ...\rangle$ denotes the thermal averages taken with the full Hamiltonian. The site index are written as susbscript and the ψ indexes as superscript, but it is important to remember **S** is a matrix both in site and ψ elements. We will keep writing in bold the matrices with no superscripts.

We will again enforce a paramagnetic solution and consider a global $\delta_{\sigma\sigma'}$ factor in front of $\mathbf{S}_{ij\sigma\sigma'}(\tau)$. The equation of motion of this composite Green's function is :

$$\frac{d}{d\tau}\mathbf{S}_{ij\sigma\sigma'}(\tau) = \delta_{\sigma\sigma'}(\delta(\tau)\langle\{\psi_{i\sigma}; \psi^\dagger_{j\sigma}\}\rangle + \theta_H(\tau)\langle\{J_{i\sigma}(\tau); \psi^\dagger_{j\sigma}\}\rangle) \tag{80}$$

Which we rewrite as

$$\frac{d}{d\tau}\mathbf{S}_{ij\sigma\sigma'}(\tau) = \delta_{\sigma\sigma'}(\delta(\tau)\delta_{ij}\mathbf{I}_{i\sigma} + \theta_H(\tau)\mathbf{M}_{ij\sigma}(\tau)) \tag{81}$$

Where we introduced the normalization matrix **I** and the overlap matrix **M** respectively as

$$\begin{aligned} \mathbf{I}_{ij\sigma} &= \langle\{\psi_{i\sigma}, \psi^\dagger_{j\sigma}\}\rangle = \delta_{ij}\begin{pmatrix} 1 - \langle n_{i\bar{\sigma}}\rangle & 0 \\ 0 & \langle n_{i\bar{\sigma}}\rangle \end{pmatrix} \\ \mathbf{M}_{ij\sigma} &= \langle\{J_{i\sigma}, \psi^\dagger_{j\sigma}\}\rangle = \begin{pmatrix} m^{11}_{ij} & m^{12}_{ij} \\ m^{12}_{ij} & m^{22}_{ij} \end{pmatrix} \end{aligned} \tag{82}$$

Because of the hopping term, the total current $J_{i\sigma}$ is not proportional anymore to the composite operator basis $\psi_{i\sigma}$. We will not be able to solve the problem exactly as in the atomic limit. We thus need to do an approximation to truncate the equations of motion. Let us start by decomposing $\delta J_{i\sigma}$ as follow:

$$\delta J_{i\sigma} = \sum_l \mathbf{P}_{il\sigma}\psi_{l\sigma} + \delta\phi_{i\sigma} \tag{83}$$

The first term contains the part of $\delta J_{i\sigma}$ proportional to $\psi_{i\sigma}$ with a proportionality matrix **P**. $\delta\phi_{i\sigma}$ contains the non proportional part of $\delta J_{i\sigma}$. To solve the equations of motion for the composite Green's function matrix, we need to compute the **I** and **M** matrix. We directly computed the **I** matrix in Eq. 82.

The M matrix requires the total current $J_{i\sigma}$ that we can express with the decomposition of $\delta J_{i\sigma}$ we introduced

$$\begin{aligned} J_{i\sigma} =& \sum_l \mathbf{E}_{il\sigma}\psi_{l\sigma} + \delta\phi_{i\sigma} \\ \mathbf{E}_{il\sigma} =& \mathbf{A}\delta_{il} + \mathbf{P}_{il\sigma} \end{aligned} \tag{84}$$

The **E** matrix contains all the terms proportional to ψ in the total current (the local **A** matrix from the atomic limit terms is analogous to Eq. 72), and $\delta\phi_{i\sigma}$ contains all terms which are not, and comes exclusively from the hopping term.

With this rewriting, the **M** matrix is now given by the following expression

$$\mathbf{M}_{ij\sigma}(\tau) = \sum_l \mathbf{E}_{il\sigma}\langle\{\psi_{l\sigma}(\tau); \psi^\dagger_{j\sigma}\}\rangle + \langle\{\delta\phi_{i\sigma}(\tau); \psi^\dagger_{j\sigma}\}\rangle \tag{85}$$

When injecting in Eq. 81, we obtain the following equation :

$$\frac{d}{d\tau}\mathbf{S}_{ij\sigma\sigma'}(\tau) = \delta_{\sigma\sigma'}(\delta(\tau)\delta_{ij}\mathbf{I}_{i\sigma} + \sum_l \mathbf{E}_{il\sigma}\mathbf{S}_{lj\sigma}(\tau) + \theta_H(\tau)\langle\{\delta\phi_{i\sigma}(\tau); \psi^\dagger_{j\sigma}\}\rangle \tag{86}$$

the first term of Eq. 85 is proportional to $\mathbf{S}_{jl\sigma\sigma'}$. However the second term with the $\delta\phi_{i\sigma}$ current is not and will introduce higher-order Green's function in the equations of motion. Hence, an approximation is needed: we will assume that $\delta\phi_{i\sigma}$ is negligible:

$$\sum_l \mathbf{E}_{il\sigma}\langle\{\psi_{l\sigma}(\tau); \psi^\dagger_{j\sigma}\}\rangle \gg \langle\{\delta\phi_{i\sigma}(\tau); \psi^\dagger_{j\sigma}\}\rangle \tag{87}$$

Three main relations can be inferred directly from this approximation. First, the total current is now proportional to ψ by construction, with the proportionality matrix **E**:

$$J_{i\sigma}(\tau) \approx \sum_l \mathbf{E}_{il\sigma}\psi_{l\sigma}(\tau) \tag{88}$$

Second, considering the definition of the **M** matrix in Eq. 85 leads to the following relation between **E** and the **M** and **I** matrix, obtained by noticing that at $\tau = 0$ (equal time) $I_{lj\sigma} = \langle\{\psi_{l\sigma}(0); \psi^\dagger_{j\sigma}\}\rangle$:

$$\mathbf{M}_{ij\sigma} \approx \sum_l \mathbf{E}_{il\sigma}\mathbf{I}_{lj\sigma} \tag{89}$$

Thirdly, we can obtain an easy form for the composite Green's function matrix after a time Fourier transform, of the equation of motion under the main approximation Eq. 87 :

$$\sum_l \delta_{\sigma\sigma'}(\omega \mathbf{Id}_2 \delta_{il} - \mathbf{E}_{il\sigma})\mathbf{S}_{lj\sigma\sigma'} = \delta_{\sigma\sigma'}\delta_{ij}\mathbf{I}_{i\sigma} \tag{90}$$

Where $\mathbf{Id}_2$ is the 2 dimensional identity matrix. At this stage one has to be careful with the inversion of these matrices. When a product of these matrices occurs, it is both done on the sites and ψ index. The inversion one needs to consider is therefore not only on the ψ parts, but also on the sites. This means one must invert a (2N $\times$ 2N) matrix. We therefore obtain the following expression

$$\mathbf{S}_{ij\sigma\sigma'}(\omega) \approx \delta_{\sigma\sigma'} \sum_l [\omega \mathbf{Id}_2 - \mathbf{E}]^{-1}_{il} \mathbf{I}_{lj\sigma} \tag{91}$$

These three equations Eq. (88), (89) and (91) are direct consequence from the main approximation. We can also include higher order terms in the basis to go further in the approximation. This has been done in Ref. [121].

Let's finally note that Eq. (88) is similar to a Schrödinger equation for the composite operators (by remembering that $\frac{d}{d\tau}\psi_{i\sigma}(\tau) = J_{i\sigma} = [\psi_{i\sigma}(\tau), H]$). The **E** matrix therefore is a non-hermitian (due to the approximation Eq. (87)) energy matrix for the composite operators. This non-hermiticity still comes with real eigenvalues due to the following mathematical property: the product of a real and symmetric matrix by a diagonal matrix has real eigenvalues (cf Appendix A for proof).

5.1.3 . Building a self-consistency

The equations of motion of the composite Green's function matrix only depends on the **E**, **M** and **I** matrices under approximation Eq. 87. We can explicitly compute them. We already computed the **I** matrix in the previous section. We obtained:

$$I_{ij\sigma} = \langle\{\psi_{i\sigma}; \psi^\dagger_{j\sigma}\}\rangle = \delta_{ij} \begin{pmatrix} 1 - \frac{\langle n_i \rangle}{2} & 0 \\ 0 & \frac{\langle n_i \rangle}{2} \end{pmatrix} \tag{92}$$

Note that since this matrix is not an identity matrix, this indicates the commutation relation of the composite operators $\psi_{i\sigma}$ are different from the usual electronic operators $c_{i\sigma}$.

In order to perform a self-consistent scheme, we will introduce the 2×2 correlation function matrix define as

$$\mathbf{C}_{ij\sigma} = \langle \psi_{i\sigma} \psi^\dagger_{j\sigma} \rangle \tag{93}$$

The interest of introducing $\mathbf{C}_{ij\sigma}$ comes from fluctuation-dissipation theorem:

$$\mathbf{C}_{ij\sigma} = \int d\omega (1 - f_D(\omega)) \left(-\frac{1}{\pi}\right) Im(\mathbf{S}_{ij\sigma}(\omega)) \tag{94}$$

With $f_D = \frac{1}{Exp(\beta\omega)+1}$ the Fermi Dirac distribution. We now need to rewrite S in order to get an easy expression for its imaginary part. Let's introduce the matrix of eigenvectors Ω of **E** such that:

$$\Lambda = \Omega^{-1} E \Omega \tag{95}$$

Then, the equation of motion Eq. 91 becomes:

$$S^{nm}_{ij\sigma\sigma'}(\omega) \approx \delta_{\sigma\sigma'} \sum_{\substack{l_1\ l_2\ l_3 \\ u_1\ u_2\ u_3}} \Omega^{nu_1}_{il_1} ([\omega \mathbf{Id}_2 - \Lambda]^{-1})^{u_1 u_2}_{l_1 l_2} (\Omega^{-1}_{l_2 l_3})^{u_2 u_3} I^{u_3 m}_{l_3 j} \tag{96}$$

We now use the fact that $\omega Id_2 - \Lambda$ is a diagonal matrix, so

$$([\omega \mathbf{Id}_2 - \Lambda]^{-1})^{nm}_{il} = \delta_{il}\delta_{nm} \frac{1}{\omega - \epsilon^n_i} \tag{97}$$

Therefore, $\mathbf{S}_{k\sigma\sigma'}$ becomes

$$S^{nm}_{ij\sigma\sigma'}(\omega) \approx \delta_{\sigma\sigma'} \sum_{\substack{l\ l' \\ uu'}} \Omega^{nu}_{il} \frac{1}{\omega - \epsilon^u_l} (\Omega^{-1})^{uu'}_{ll'} I^{u'm}_{l'j} \tag{98}$$

Which can be rewritten as

$$\mathbf{S}^{nm}_{ij\sigma\sigma'}(\omega) = \delta_{\sigma\sigma'} \sum_{l} \sum_{u=1}^{2} \frac{(\boldsymbol{\sigma}^u_l)^{nm}_{ij}}{\omega - \epsilon^a_l} \tag{99}$$

With

$$(\boldsymbol{\sigma}^u_l)^{nm}_{ij} = \Omega^{nu}_{il} \sum_{u'l'} (\Omega^{-1})^{uu'}_{ll'} I^{u'm}_{l'j} \tag{100}$$

This expression simplifies in momentum space using translational invariance since this makes every term diagonal in momentum space (indeed, the sum over the sites can be rewritten as convolution products which are simple products in momentum space). Accordingly to ref. [122], we then get the simpler expression:

$$S^{nm}_{k\sigma\sigma'}(\omega) = \delta_{\sigma\sigma'} \sum_{u=1}^{2} \frac{(\sigma^u_k)^{nm}}{\omega - \epsilon^u_k} \tag{101}$$

With

$$(\boldsymbol{\sigma}^u_k)^{nm} = \Omega^{nu}_{k} \sum_{u'} (\Omega^{-1})^{uu'}_{k} I^{u'm}_{k} \tag{102}$$

Equation (101) is an usual form for the Green's function. Indeed, this looks like the Lehman representation we obtained in sec. 4.1.2. We now introduce a vanishing complex quantity to the frequency 0^+. Then, we use the Cauchy principal value distribution of the inverse function:

$$\frac{1}{x + i0^+} = Pv(\frac{1}{x}) - i\pi\delta(x) \tag{103}$$

Where Pv(x) denotes the Cauchy principal value of x. Applying this on Eq. (101) (using the fact that σ are spectral weight and are therefore real) and injecting it in Eq. (94) leads to :

$$\mathbf{C}_{k\sigma} = \frac{1}{2}\sum_{a=1}^{2}\left(1 + \tanh\frac{\beta\epsilon^a_{k\sigma}}{2}\right)\boldsymbol{\sigma}^a_{k\sigma} \tag{104}$$

Where $\beta = \frac{1}{k_B T}$ comes from the Fermi Dirac distribution. Eq. (104) is important because it shows that knowing the E matrix means one can express the correlation functions **C**. We know that from the **M** and **I** matrices we can obtain the energy matrix **E** using Eq. (89). Therefore, to close the system and build a proper self-consistent scheme, we know need to explicitly compute the **M** and **I** matrices and express them as a function of the correlation functions.

The **I** matrix has already been determined in Eq. (82). In order to compute **M**, we now compute explicitly the currents. Since the ψ basis is composed of the same Hubbard operators as the one introduced in Sec. 4.2.1, the currents have the same form that we remind here:

$$\begin{aligned} j^1_{i\sigma} =& -\mu\xi_{i\sigma} - \sum_l t_{il}\left(c_{l\sigma} - n_{i\bar{\sigma}}c_{l\sigma} + S_i^{sign(\bar{\sigma})}c_{l\bar{\sigma}} + sign(\bar{\sigma})\Delta_i c^\dagger_{l\bar{\sigma}}\right) \\ j^2_{i\sigma} =& -(\mu - U)\eta_{i\sigma} + \sum_l t_{il}\left(-n_{i\bar{\sigma}}c_{l\sigma} + S_i^{sign(\bar{\sigma})}c_{l\bar{\sigma}} + sign(\bar{\sigma})\Delta_i c^\dagger_{l\bar{\sigma}}\right) \end{aligned} \tag{105}$$

With $S_i^- = c^\dagger_{i\downarrow}c_{i\uparrow}$, $S_i^+ = c^\dagger_{i\uparrow}c_{i\downarrow}$ and $\Delta_i = c_{i\uparrow}c_{i\downarrow}$. We take the following convention: $sign(\uparrow) = 1$ and $sign(\downarrow) = -1$. The coefficients of the **M** matrix can then be expressed:

$$\begin{aligned} m^{11}_{ij} =& -\mu\left(1 - \frac{n_i}{2}\right)\delta_{ij} - \delta_{ij}\sum_l t\alpha^1_{il}e_{il} - t\alpha^1_{ij}(1 - \frac{n_i + n_j}{2} + p_{ij}) \\ m^{12}_{ij} =& \delta_{ij}\sum_l t\alpha^1_{il}e_{il} - t\alpha^1_{ij}\left(\frac{n_j}{2} - p_{ij}\right) \\ m^{22}_{ij} =& -(\mu - U)\frac{n_i}{2}\delta_{ij} - \delta_{ij}\sum_l t\alpha^1_{il}e_{il} - t\alpha^1_{ij}p_{ij} \end{aligned} \tag{106}$$

With

$$\begin{aligned} e_{ij} &= \langle\xi_{j\sigma}\xi^\dagger_{i\sigma}\rangle - \langle\eta_{j\sigma}\eta^\dagger_{i\sigma}\rangle \\ p_{ij} &= \langle n_{i\sigma}n_{j\sigma}\rangle + \langle S_i^- S_j^+\rangle - \langle\Delta_i\Delta_j^*\rangle \end{aligned} \tag{107}$$

$\alpha^1_{il} = \frac{t_{il}}{t}$ is equal to 1 if i and l are nearest neighbors, and 0 otherwise.

The parameter e contains correlations between neighboring composite operators and will mainly re-normalize the chemical potential because it always appear in M in front of a δ_{ij}. The p parameter contains charge-charge, spin-spin and pair-pair correlations and contain most of the physics of the interactions.

We now use the translational invariance of the system: each parameters with a dependence in two sites i and j will only depend on the distance between these two sites $i - j$. Hence we get

$$\begin{aligned} e_{ij} =& e_{i-j} \\ p_{ij} =& p_{i-j} \\ \mathbf{M}_{ij} =& \mathbf{M}_{i-j} \end{aligned} \tag{108}$$

We assume lattice inversion and rotation (C_4) symmetries and we take n, p and e as constants

$$\begin{aligned} n_i &= n \\ p_{i\pm\delta_x} &= p_{i\pm\delta_y} = p \\ e_{i\pm\delta_x} &= e_{i\pm\delta_y} = e \end{aligned} \tag{109}$$

Under these assumptions the coefficients of the **M** matrix become

$$\begin{aligned} m_{ij}^{11} &= -\mu\left(1-\frac{n}{2}\right)\delta_{ij} - \delta_{ij}4te - t\alpha_{ij}^{1}(1-n+p) \\ m_{ij}^{12} &= \delta_{ij}4te - t\alpha_{ij}^{1}\left(\frac{n}{2}-p\right) \\ m_{ij}^{22} &= -(\mu-U)\frac{n}{2}\delta_{ij} - \delta_{ij}4te - t\alpha_{ij}^{1}p \end{aligned} \tag{110}$$

And the **E** matrix defined by Eq. (89) is given by

$$\mathbf{E}_{ij} = \begin{pmatrix} \frac{2}{2-n}m_{ij}^{11} & \frac{2}{n}m_{ij}^{12} \\ \frac{2}{2-n}m_{ij}^{12} & \frac{2}{n}m_{ij}^{22} \end{pmatrix} \tag{111}$$

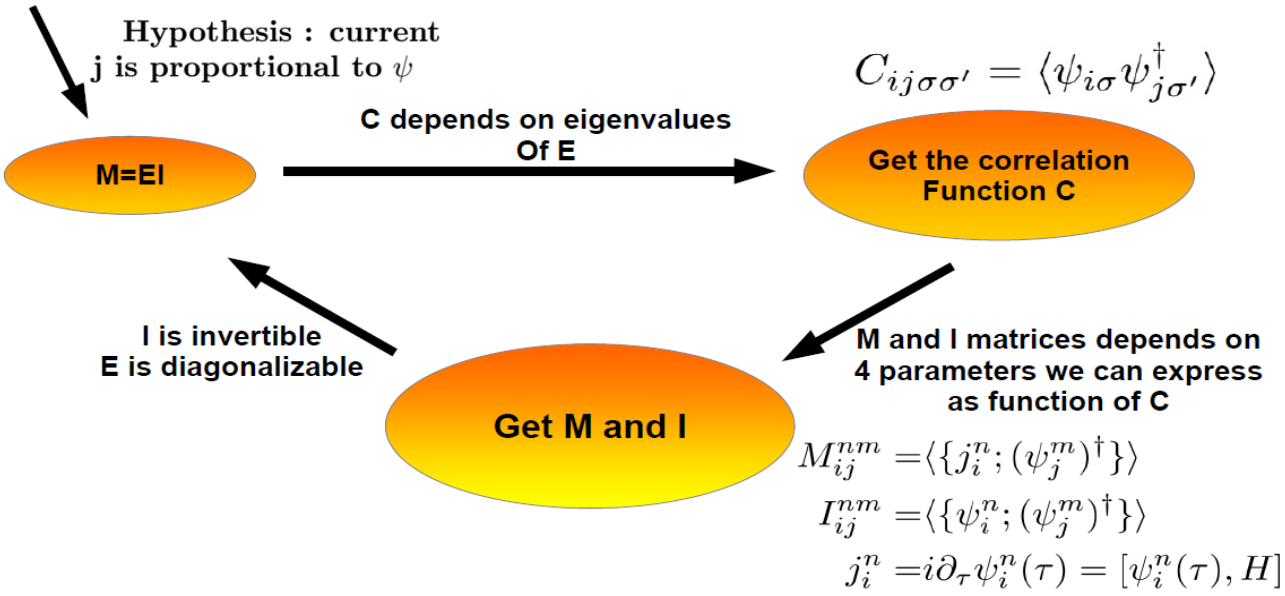

Figure 11: The self consistency loop. Our hypothesis on the currents allows us to get a relation between the **M** and **I** matrices (Eq. (89)). The energy matrix **E** is diagonalizable. We can express correlation functions as a function of its eigenvalues with Eq. (104). Then, we can rewrite the **M** and **I** matrices in term of these correlations functions and do a self-consistency (Eq. (112)).

This matrix is diagonalizable and Eq. (104) allows to relate the correlation function $\mathbf{C}_{ij\sigma} = \langle\psi_{i\sigma}\psi^{\dagger}_{j\sigma}\rangle$ with the eigenvalues of the E matrix. Thus in order to close the system the only thing left to do is expressing the parameters in the **M** and **I** matrices as a function of the correlation functions. Since

e and n are one-body parameters, they can easily be expressed. Expressing p as a function of the correlations functions is not so direct since it is composed of two-bodies operators. Following the step of L. Roth [101], we express p as a function of correlation functions by mean of equations of motion. In appendix B are all of the details of Roth decoupling applied to p. After some algebra, the final expression of the parameters appearing in **M** and **I** as a function of the correlation functions are

$$\begin{cases} e &= C^{11} - C^{22} \\ n &= 2(1 - C_0^{11} - 2C_0^{12} - C_0^{22}) \\ p &= \frac{n^2}{4} - \frac{\rho_1}{1-\phi^2} - \frac{\rho_1}{1-\phi} - \frac{\rho_3}{1+\phi} \end{cases} \quad \text{With} \quad \begin{cases} \phi &= -\frac{2}{2-n}(C_0^{11} + C_0^{12}) + \frac{2}{n}(C_0^{12} + C_0^{22}) \\ \rho_1 &= \frac{2}{2-n}(C^{11} + C^{12})^2 + \frac{2}{n}(C^{22} + C^{12})^2 \\ \rho_3 &= \frac{4}{n(2-n)}(C^{11} + C^{12})(C^{22} + C^{12}) \end{cases} \tag{112}$$

In this equation $\mathbf{C}_0 = \mathbf{C}_{ii}$ are constants by translational invariance. and $\mathbf{C} = \mathbf{C}_{ij} = \mathbf{C}_{i-j}$ is treated as e and p in Eq. (109) using lattice inversion and rotation (C_4) symmetry, so it is also a constant but different from $\mathbf{C}_0$.

The system has now been closed. For simplicity (namely due to Eq. (101)) we will perform the numerical study in momentum space. In Fig. 11, we represented the self-consistency pattern. Starting from initial guess for e, n and p, we compute the **M** and **I** matrices. We can then obtain **E** and diagonalize it. Then, using Eq. (104), we can relate the correlation functions with the eigenvalues of **E**. Finally, using the self consistent Eq. (112), we compute again e, p and n. We stop when $f(x) - x < \delta$ where $x = (e, p, \mu)$ and f are given in Eq. (112). We chose $\delta = 10^{-8}$. Once the system converges, we use the parameters (e, p, μ) to compute the electronic Green's function using the relation between **S** and G:

$$\begin{aligned} G_k(\omega) =& S_k^{11}(\omega) + S_k^{12}(\omega) + S_k^{21}(\omega) + S_k^{22}(\omega) \\ =& \sum_{l=1}^{2} \frac{(\sigma^l)_k^{11} + (\sigma^l)_k^{12} + (\sigma^l)_k^{21} + (\sigma^l)_k^{22}}{\omega - \epsilon_k^l + i0^+} \end{aligned} \tag{113}$$

Where the $\boldsymbol{\kappa}$ act as spectral weights and are defined in Eq. (102) and ϵ^1 and ϵ^2 are the eigenvalues of the **E** matrix, and can be built from the parameters (e, p, μ).

Finally the composite operator method can be compared with the Hubbard I approximation, wich is also known to exhibit a Mott-insulator transition as long as $U \neq 0$ [53] (cf Sec 4.2.2). It is however a less refined assumption than the composite operator method because it completely neglects some components of the currents and assume the Hubbard operators behave like electrons (see Sec. 4.2.2). Albeit under the approximation from Eq. 87, the composite operator treatment consider the full expression of the current and the non-electron like algebra of the Hubbard operators. It can thus only be considered as more refined than Hubbard I.

5.2 . Mott-insulator transition

5.2.1 . Bands and Fermi surfaces

The method presented in the previous subsection use a decoupling scheme initially developped by L. Roth for the expression of the parameter p. The converged solutions obtained with this self-consistency have the notable drawback of having an on-site correlation function C_0^{12} non zero while it should analytically be zero due to Pauli principle. Indeed, we can see that by explicit computation:

$$
\begin{aligned}
C_0^{12} &= \langle \xi_{i\sigma} \eta_{i\sigma}^\dagger \rangle \\
&= \langle c_{i\sigma} c_{i\sigma}^\dagger n_{i\bar{\sigma}} + c_{i\sigma} c_{i\bar{\sigma}}^\dagger c_{i\sigma}^\dagger c_{i\bar{\sigma}} n_{i\bar{\sigma}} \rangle \\
&= \langle -c_{i\sigma} (c_{i\bar{\sigma}}^\dagger)^2 c_{i\sigma}^\dagger (c_{i\bar{\sigma}})^2 \rangle \\
&= 0
\end{aligned}
\tag{114}
$$

It is important to note that this Pauli violation of C_0^{12} not being zero after numerical convergence gets smaller with increasing U and is exactly zero at half-filling [122]. Furthermore, Roth decoupling does not introduce any other approximation: in appendix B, the only approximation used to express the p parameter using Roth decoupling is the main composite operator approximation Eq. (87) that is already assumed in the method itself.

In references [123] [122], another self-consistency have been suggested. Instead of considering a self-consistent equation on the p parameter, $C_0^{12} = 0$ is explicitly imposed and p is allowed to vary freely to satisfy this condition. From now on, we will call "Roth scheme" the self-consistency using Roth decoupling, and "Pauli scheme" the one imposing $C_0^{12} = 0$ instead.

In this section we now compare the two schemes and their respective solutions with nearest-neighbours. In Fig 12 we start by plotting the eigenvalues of the E matrix for two schemes. It is important to note that we found a unique solution for Roth scheme, and two solution for Pauli scheme, that we will call "COM1" and "COM2" accordingly to ref. [122]. The eigenvalues of the E matrix can be understood as the bands obtained after the composite operator treatment. Indeed in Eq. (113) one can note the eigenvalues of the E matrix corresponds to the poles of the electronic Green's function, with a spectral weight given by Eq. (102). In red on Fig 12 we plot the U=0, tight-binding dispersion for comparison.

The solutions have two Hubbard bands associated with the two eigenvalues of the energy matrix, split by the interaction strength U. The COM2 and Roth solutions exhibit Mott insulator physics at half-filling as the chemical potential resides between the two bands. In contrast, contrary to the conventional understanding, the COM1 solution represents a metallic phase at half-filling for $t = 1$, $U = 8t$. Consequently, COM1 cannot be deemed a physically viable solution for the Hubbard model in strong coupling regimes.

The COM2 solution always presents two holes pockets, leading to two Fermi Surfaces in Fig. 13. This is unexpected, as this has never been observed by ARPES experiments for strongly correlated materials such as cuprates where this treatment of the Hubbard model is relevant. However, in Ref. [121] the basis has been extended to take into account dynamical corrections of the self-energy. The lifetime of the second hole pocket is then computed and happens to be small, which can explain why it is not observed experimentally. Finally, the Roth solution (Fig. 12c) has the advantages of presenting only one hole pocket and a maximum at (π, π). This maximum is consistent with the tight-binding bands. COM2 bands have a minimum at (π, π) which can also comes as a surprise because it leads to a solution completely different from the non-interactive one.

It is also important to notice the so called "waterfall" feature. This consists in a loss of spectral weight on the lower Hubbard band around $M = (\pi, \pi)$, and an increase on the upper band at the same momentum. The spectral weight, overlapped in colors on Fig 14, is defined as the excitation of the system when adding or removing an electron. It is obtained by plotting the spectral function

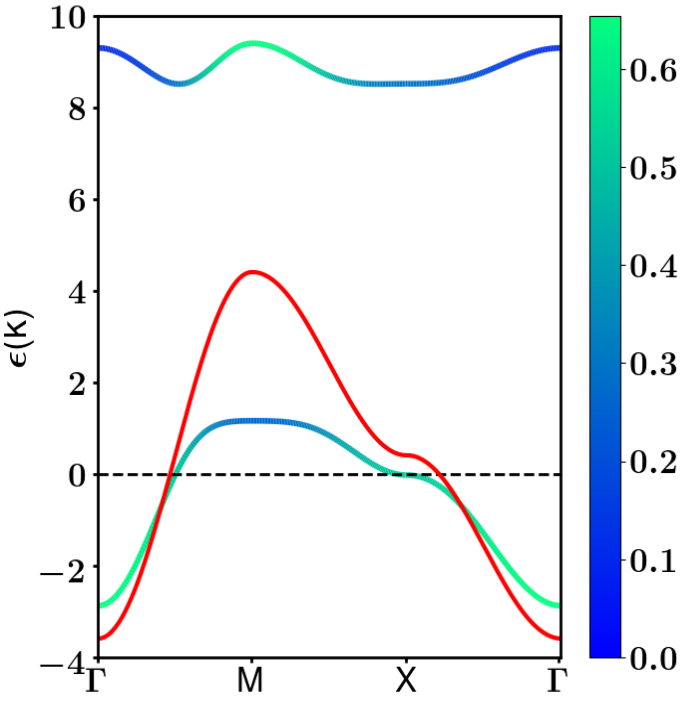

(a) Roth Minimization.

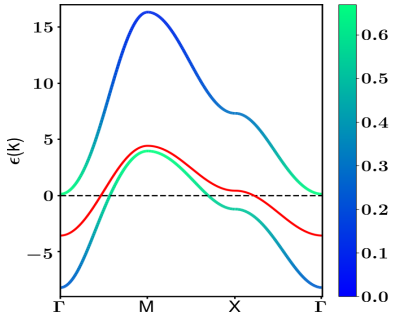

(b) First Pauli solution (COM1)

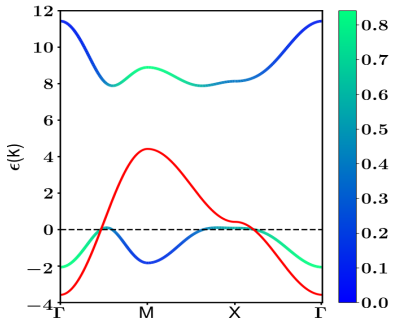

(c) Second Pauli solution (COM2)

Figure 12: (a), (b), (c): Bands along high symmetry points with $t = 1, U = 8t, T = 0, n = 0.8$ for (a) Pauli COM1 solution, (b) Pauli COM2 solution, (c) Roth solution. The non interacting (tight-binding) band is in red. The composite operator treatment of the interaction splits it into 2 Hubbard bands obtained for every solutions. We overlapped in color the spectral function $A(k, \omega)$ along high symmetry points. At half filling the chemical potential lies in between the two Hubbard bands and we get a Mott insulator, except for COM1 that is therefore considered unphysical. The shape of the COM1 Hubbard bands is also similar to the non-interacting band, they are simply splitted by U. We observe a flattening of the bands around X=$(\pi, 0)$ for both COM2 and Roth solution.

$A_k(\omega)$, which is defined as the imaginary part of the electronic Green's function. The waterfall effect is currently under debate of being an universal features in cuprates [124, 125].

The waterfall effect has already been observed with Hubbard I approximation, and the same transfer of spectral weight around M is observable on Fig. 7. According to [57], the following interpretation can be given in the context of lower and upper Hubbard bands: in momentum space, when hole doping close the half-filling, the only available states lies near momentum close to (π, π) since the lower Hubbard band presents a maximum. Therefore, upon adding an electron, the excitation can only happen around this momentum. For electron density close to half-filling, this excitation has high chances to create a double occupied states, thereby costing an energy U to the system, and trans-

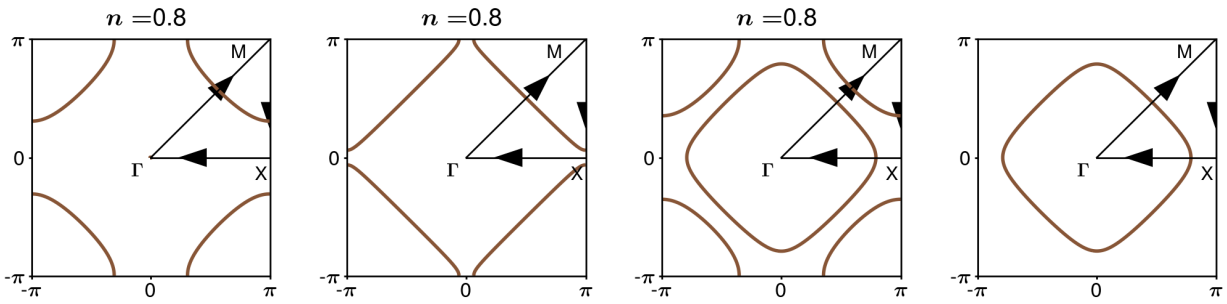

Figure 13: From left to right we plot the Fermi surfaces (imaginary part of Eq. (113) at $\omega = 0$, here we show the contour line $\epsilon_k = 0$) of COM1, Roth, COM2 and the non-interacting (tight-binding) case respectively at n=0.8, t=1, T=0 and U=8t (0 for the non-interacting case). COM2 solution exhibits two hole pockets around (0,0) and (π, π). The two dispersions obtained from the Pauli minimization we obtain are analogous to Ref. [122]. The Fermi surface of Roth solution is diamond-like and would corresponds to half-filling if Luttinger theorem would hold.

fering the excitation to the upper Hubbard band at the same momentum. This is consistent with 12 which is at 20% electron density and exhibit much less spectral weight on the upper Hubbard band around M symmetry point than on fig 14 which is closer to half-filling.

Once reaching half filling, the Roth and the COM2 solution bands become alike, and are plotted on Fig. 14. The chemical potential has a degenerate range of value it can take within the gap, and the system is a Mott-insulator.

Close to half filling (2% hole doping), the Roth solution exhibits a second small hole pocket at (π, π) that can be observed both on the bands of 14 on the Fermi surface on Fig. 15. This second hole pocket around (π, π) may be the consequence of the paramagnetic assumption $\langle n_{i\uparrow} \rangle = \langle n_{i\downarrow} \rangle = \frac{n}{2}$. It appears around half filling where we know the antiferromagnetic phase dominates [126]. The wave-vector (π, π) is associated with antiferromagnetism, so this second hole pocket might be an instability of the system because we neglected it.

5.2.2 . Density of states and Luttinger theorem

In the previous section we arrived to the conclusion that COM1 is not a good solution. While the presence of the second hole pocket at every filling that COM2 exhibit is unusual for strongly correlated materials such as cuprates, both COM2 and Roth are indeed Mott insulator at half-filling and metallic away from half-filling, as well as exhibiting the well known "waterfall" feature.

In this section we focus on the study of the density of states and the validity of Luttinger theorem.

In Fig. 16, we plot it as a function of energy for several doping with the Roth and COM2 solutions respectively. The density of states has been computed from the spectral function using the following formula

$$\mathcal{D}(\omega) = \frac{1}{N^2} \sum_{k_x, k_y = 1}^{N} \left(-\frac{1}{2\pi} \right) Im(G(\mathbf{k}, \omega)) \tag{115}$$

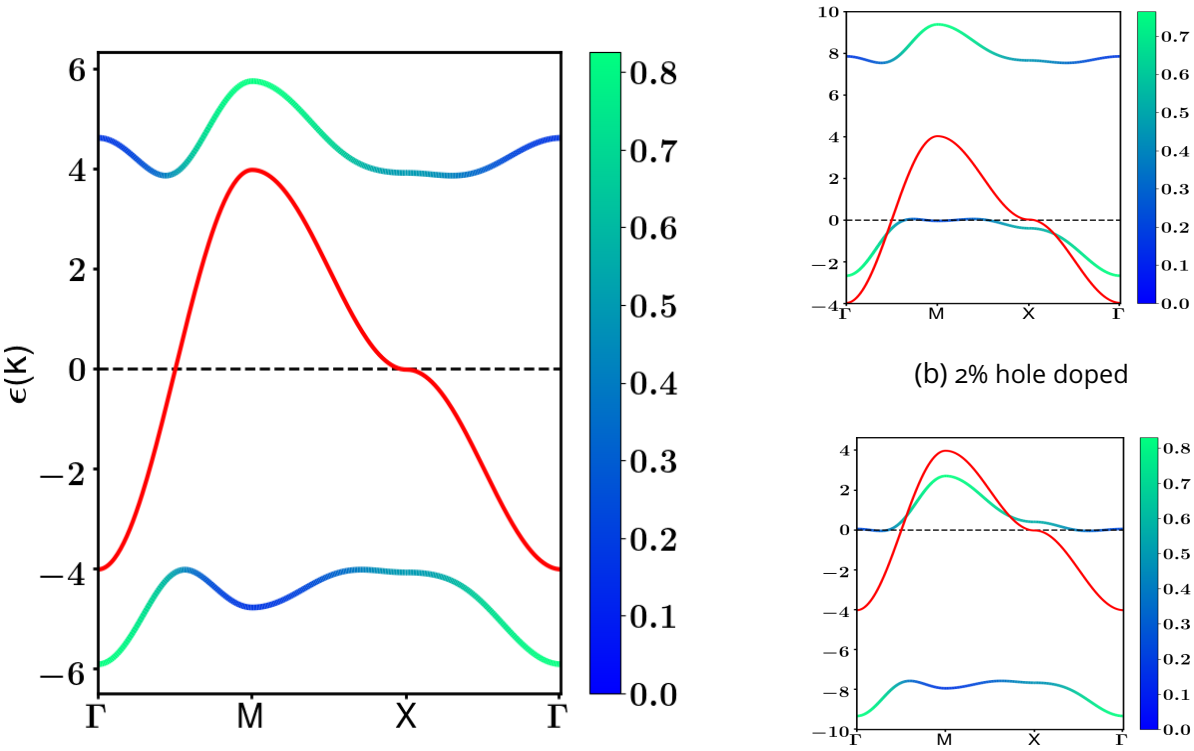

(a) Half-filling.

(b) 2% hole doped

(c) 2% electron doped

Figure 14: (a) Bands obtained at half-filling with COM2 and Roth (both solution leads to the same bands). (b) and (c) Bands obtained by Roth minimization in the neighboorhood of half filling (2% hole and electron doped respectively).

Where N denotes the number of considered points for sampling k_x and k_y and G is the electronic Green's function introduced in eq. 113.

At half filling we do not have any states at the Fermi energy for both Roth and COM2, since the model leads to a Mott insulator for this doping and the chemical potential lies in between the upper and lower Hubbard bands. Close to the Hubbard gap two peaks can be distinguished. Usually, in 2D a Van Hove singularity can only appear at a saddle point, not at a maximum or a minimum of the dispersion. But these two peaks may be interpreted as a remnant of the tight-binding, U=0 model. Indeed, as seen in Sec. 4.1.3, if only considered with nearest-neighbors, the Van Hove singularity lies at half-filling. Here, at half-filling both COM2 and Roth density of states presents some peaks around the gap, as if the tight-binding Van-Hove singularity have been "split" in two by the interaction. This is possible thanks to the spectral weight in Eq. 102 that can renormalize the density of states. These peaks near the edges of the gap seems to be a characteristic of Mott-Physics and the transfer of spectral weight usually occuring [127].

For every doping except half-filling, a third peak is also observable for Roth solution and corre-

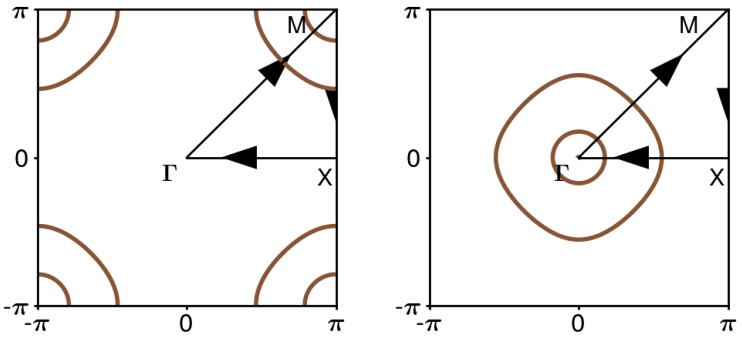

Figure 15: Fermi Surfaces of Roth solution at n=0.98 (left) and n=1.02 (right). A second hole-pocket appear close at these dopings for Roth solution near. We assume this is a consequence of the paramagnetic assumption since it is centered on (π, π) when hole-doped. This second hole pocket disappear after 3-4% hole or electron doping.

sponds to the Van Hove singularity. It is indeed associated to a saddle point of the dispersion on Fig. 12 around $(\pi, 0)$. The Fermi energy is exactly at this Van Hove peak at n=0.8 or n=1.2. In term of Fermi surface for a square lattice the Van Hove singularity corresponds to the doping below which the Fermi Surface is centered on $(0, 0)$ and above which it is centered on (π, π). In Fig. 17 we confirm the peak observed on the density of states away from the gap peaks is indeed following this behavior. Note the COM2 solution has no such peaks. This is consistent with the absence of saddle point in the dispersion.

Regarding the Mott transition, we see at half filling no quasiparticle peak is observed around the Fermi energy. Instead, the density of states is closer to what was observed with determinantal quantum Monte Carlo simulation (DQMC) in Ref. [29]. DQMC is a stochastic algorithm which allows under some limitations to perform direct studies of complex condensed matter problems. As predicted by DQMC in Ref [29], at doping close to half-filling we only observe a transfer of spectral weight between the lower and upper Hubbard band occurs, changing the density of states, without creating a quasiparticle peak at the Fermi energy at half filling. Therefore in this regime where $U \gg t$ the density of states of the lower and upper Hubbard bands are the only contribution.

We now turn our attention to the Luttinger theorem. This theorem states that the volume enclosed by the Fermi surface is proportional to the electron density [128]. The regime of validity of Luttinger theorem is still a very debated topic [129, 130, 131]. To compute the volume enclosed by the Fermi surface, we can use the spectral function at the Fermi energy, defined from the electronic Green's function Eq. (113). The $\boldsymbol{\sigma}$ act as spectral weights of the electronic Green's function. The Fermi surface is therefore given by the spectral function at the Fermi energy (corresponding to $\omega = 0$):

$$\begin{aligned} A_k(\omega = 0) &= -\frac{1}{\pi} Im(G_k(\omega = 0)) \\ &= \sum_l [(\sigma^l)_k^{11} + (\sigma^l)_k^{12} + (\sigma^l)_k^{21} + (\sigma^l)_k^{22}] \delta(\epsilon_k^l) \end{aligned} \tag{116}$$

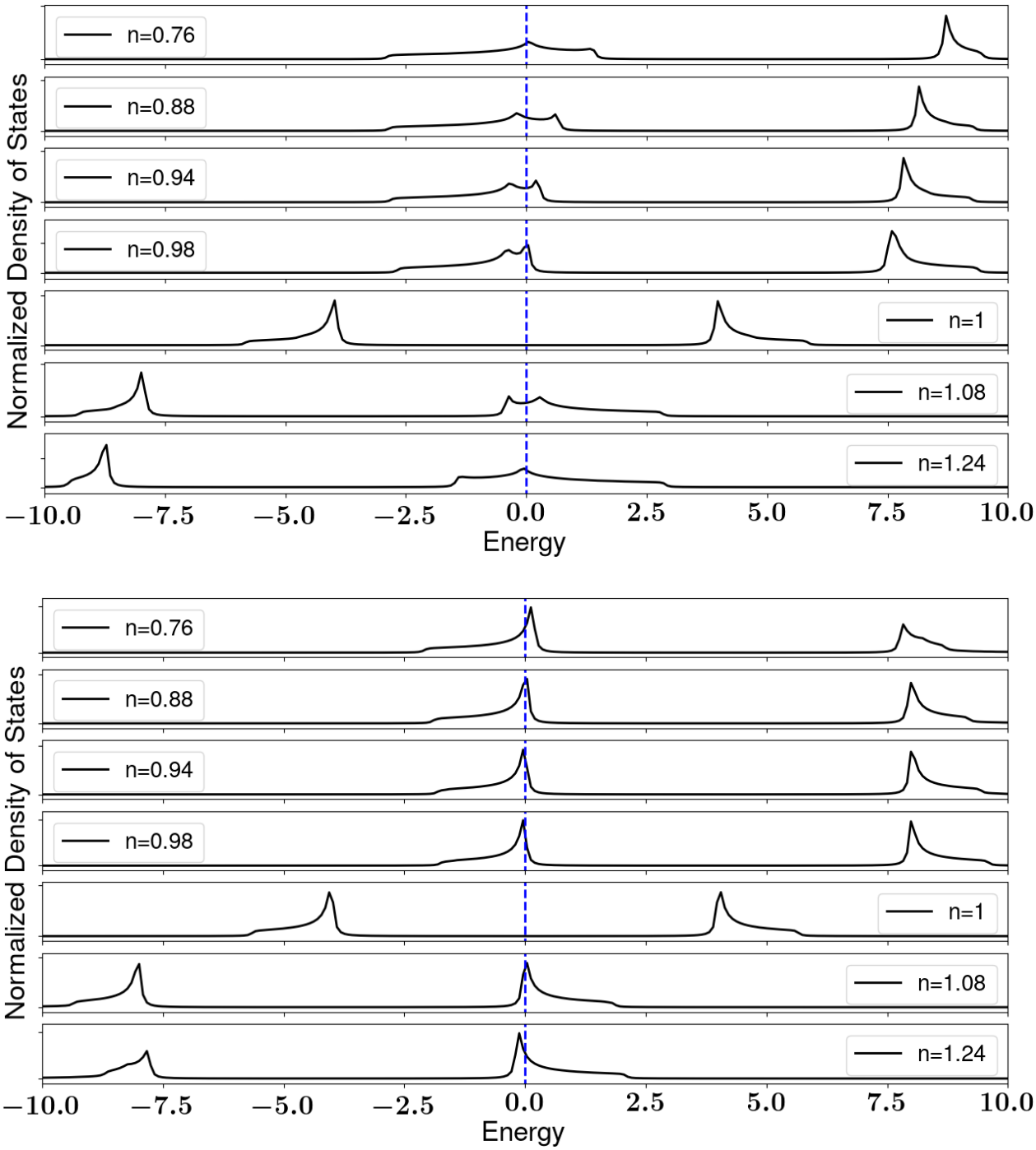

Figure 16: Density of states in energy with parameters $t = 1, U = 8t$ and $T = 0$, of Roth solution (top) and COM2 solution (bottom) with nearest neighbors. From top to bottom the filling is respectively: n=0.76, 0.88, 0.92, 0.98, 1 (half filling), 1.08 and 1.24. The blue line corresponds to the chemical potential.

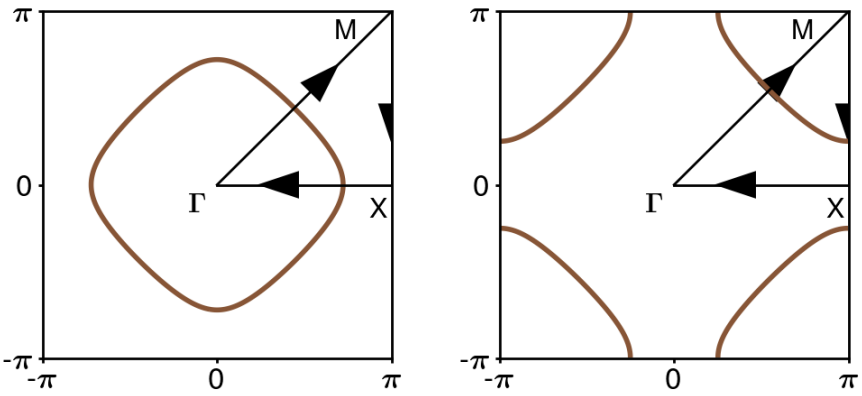

Figure 17: Fermi Surface obtained with Roth solution, at n=0.7 and n=0.9.The chemical potential or the Fermi energy coincides with the Van Hove singularity for some specific electron density (here n=0.8). Below the singularity the Fermi surface is centered around $(0, 0)$, and above the singularity it is centered around (π, π)

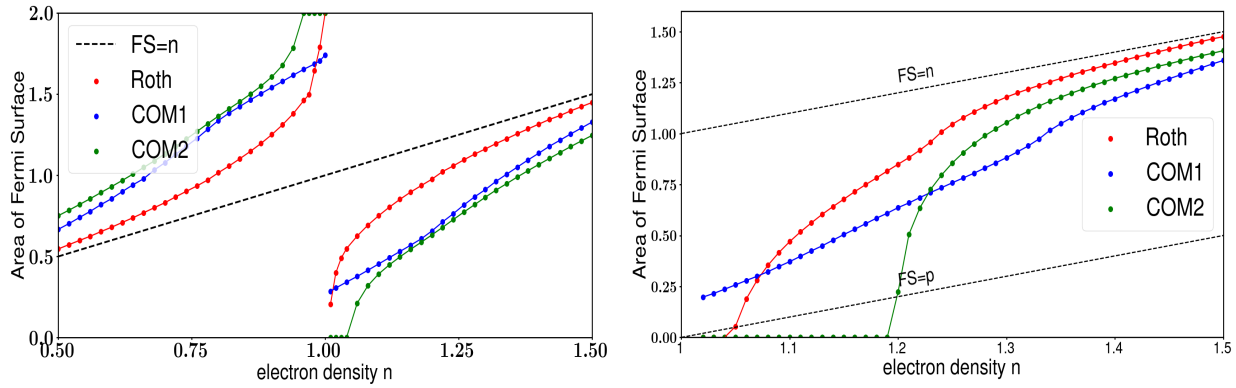

(a) Luttinger Violation at U=8t, T=0

(b) Luttinger violation at U=10t, T=0.5

Figure 18: Area of Fermi surface as a function of doping. It is computed using Eq. (117). We observe a violation of Luttinger theorem for all solutions. The two figures are obtained at (a) $T = 0$K ($\beta \approx 10^5 t$) and $U = 8t$, (b) $\beta = 2t$ and U=10t to make a comparison with what was obtained in Ref. [29] from Determinantal Monte Carlo. The solutions are proportional to the electron density only asymptotically (the curves and the black dotted line “FS=n" associated to Luttinger theorem are not parallel). The system is in a “Luttinger breaking phase".

Thus, the Fermi contour is the set of points associated to a vanishing ϵ^l_{ij}. Therefore a way to compute the enclosed area A_{FS} is simply by considering the following equation

$$A_{FS}^{l} = \frac{1}{N^2} \sum_{k_x,k_y=1}^{N} \theta_H(\epsilon_k^l) \tag{117}$$

Note in this last equation we do not have the sum over the two eigenvalues. Indeed, one must only consider the bands that are not completely filled (the empty bands are at a positive energy so will not be counted), so l has to been chosen accordingly. For instance, in the electron-doped regime the lower band is going to be filled, so l must correspond to the eigenvalue of the upper band in order to not count the fully filled lower Hubbard band in the area of the Fermi Surface.

Fig. 18 reveals that the Luttinger theorem is violated. This violation is analogous to what was observed by Ref. [29] using determinantal quantum Monte-Carlo simulations. In Fig. 18, we plot Luttinger violation observed with the same parameters as in Ref. [29] (U=10t and β=2). We obtain analogous results: while none of the solutions we considered are precisely similar to what was observed with determinantal quantum Monte-Carlo, we have the same overall behavior. Our curves are not parallel to the black dotted line representing the Luttinger theorem (where Fermi surface area equals electron density). The system is in a “Luttinger breaking phase". Contrary to results of Ref. [29]which indicates a critical density after which Luttinger theorem holds, with composite operators the theorem seems broken at every doping and verified only asymptotically at maximum and minimum doping. This violation is expected, given the non-fermionic commutation relation of the composite operators: the model is not describing a Fermi liquid.

5.2.3 . Parameters study and particle-hole symmetry

In this section, we consider the individual effect and physical meaning of the self-consistent parameter, and verify how and if they enforce particle-hole symmetry.

We first start by providing a physical interpretation of the effect of the parameters on the system. In fig. 19, we plot the three self-consistent parameters as a function of the electron density at $U = 8t$, $t = 1$ and T=0.

The chemical potential is a well known physical quantity : it fixes the filling of the bands accordingly to the electron density that we fix as an external parameter. It is nonetheless worth mentioning the jump at half-filling (corresponding to electron density $n = 1$) it makes for the COM2 and Roth solution. This is in agreement with the band study: this chemical potential gap is of the order of U and therefore corresponds to the lower Hubbard band being filled and the upper Hubbard band starting to be filled. COM1 does not exhibit this behavior, as we concluded it is not a Mott-insulator close to half-filling and is not a good physical solution.

The parameter e is defined as follow:

$$e = \langle \xi_{j\sigma} \xi_{i\sigma}^{\dagger} \rangle - \langle \eta_{j\sigma} \eta_{i\sigma}^{\dagger} \rangle \tag{118}$$

where i and j are nearest-neighbors. We remind the ξ operator represents the transition from an empty to a singly occupied state, and the η parameter the transition from a single to a doubly occupied state. Hence $\xi_{j\sigma}\xi_{i\sigma}^{\dagger}$ moves a σ electron from single occupied state j to empty state i: it corresponding to a hole propagating to nearest neighbors. On the other hand, $\eta_{j\sigma}\eta_{i\sigma}^{\dagger}$ destroys the double occupied state on j and create a pair on site i. It is thus associated with pair propagation.

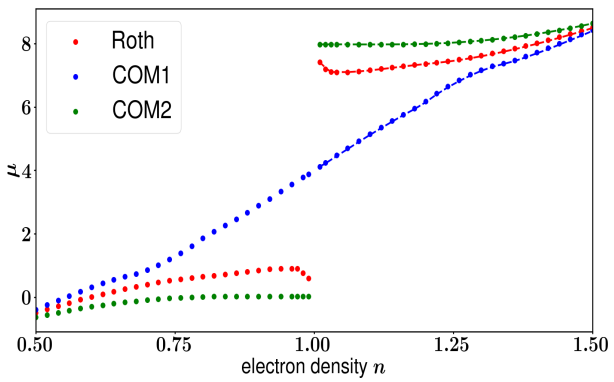

(a) Chemical potential

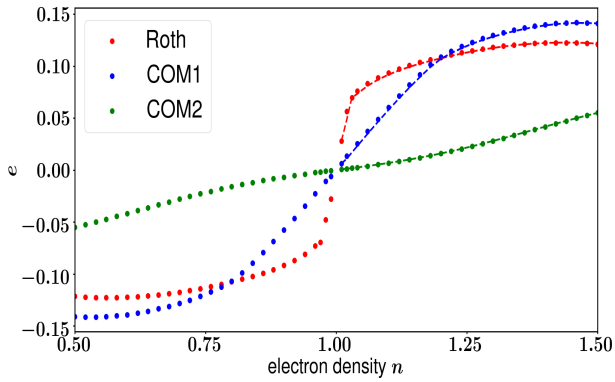

(b) Parameter e

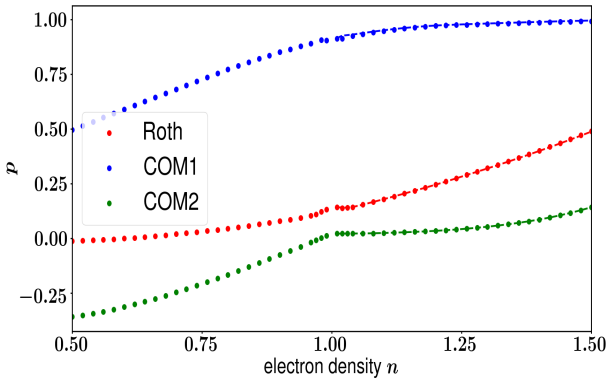

(c) Parameter p

Figure 19: (a), (b) and (c): parameters as a function of doping for each solution. The dash lines in the electron dope ($n >$1) region are the particle-hole symmetric (128) of their equivalent in the hole doped region.

Therefore, if e counts the number of hole propagating without creating a pair minus the number of pair propagating without creating a hole. As a consequence, this parameter vanishes exactly at half-filling because of the Mott-Insulator physics: no hole or pairs can propagate. The main contribution of e to the dispersion will be to renormalize the chemical potential.

The p parameter involves two-bodies correlations. We remind it is defined as:

$$p = \langle n_{i\sigma} n_{j\sigma} \rangle + \langle S_i^- S_j^+ \rangle - \langle \Delta_i \Delta_j^* \rangle \tag{119}$$

It represents the interaction both in the charge, the spin and pair sector. Because it only involves nearest neighbors processes, it can have many effects both on the shape or bandwidth of the dispersion. A notable drawback of the Pauli scheme is due to the fact p is free to vary since Pauli scheme replaced the self-consistent Roth decoupling equation on p to enforce Pauli principle. However, the Roth decoupling detailed in Appendix B does not make any other assumptions than the main composite operator assumption we made at the beginning in Eq. 87.

This decoupling is therefore consistent with the method and should always be equal to the p parameter. But the converged value of p with the Pauli scheme is not matching the value of p one would

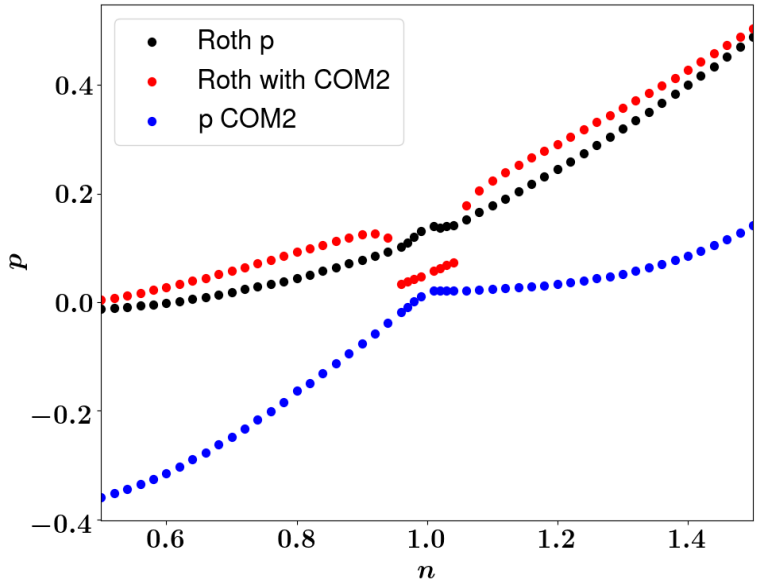

Figure 20: Parameter p with Roth scheme (black) as a function of electron density n. In blue we plot the p parameter after convergence for COM2 solution. Then, in red we display the value of p with Roth decoupling using the converged self-consistent parameters from COM2 solution. Since the red and blue curves are not matching, COM2 solution is not respecting Roth decoupling. This is unexpected, as the decoupling involves no other approximation than the main COM approximation we already make in the method.

obtain if we compute it from Roth decoupling using the converged Pauli correlation functions. This issue shows that Pauli scheme is not giving consistent results with the composite operator approximation. The Pauli violation seems to come from the main approximation Eq. 87 itself. For this reason, the Roth scheme appears as the best scheme to consider.

Let us now check the validity of particle-hole symmetry with the method. It is well known that the Hubbard model with nearest neighbour hoppings only is particle-hole symmetric. This symmetry exchanges particles and holes with the transformation

$$c_{i\sigma} \to (-1)^i c_{i\sigma}^\dagger \qquad c_{i\sigma}^\dagger \to (-1)^i c_{i\sigma} \tag{120}$$

We could also have taken another convention for this transformation without any $(-1)^i$, as long as we change t to -t to keep the Hamiltonian invariant. Applied to the composite operators one can show that it becomes

$$\eta_{i\sigma} \to (-1)^i \xi_{i\sigma}^\dagger \quad \xi_{i\sigma} \to (-1)^i \eta_{i\sigma}^\dagger \tag{121}$$

With the paramagnetic assumption, the particle-hole transformation is rewritten

$$\begin{aligned} &\langle c_{i\sigma}^\dagger c_{i\sigma} \rangle \to \langle c_{i\sigma} c_{i\sigma}^\dagger \rangle \\ \Leftrightarrow\ &\frac{n}{2} \to 1 - \frac{n}{2} \end{aligned} \tag{122}$$

Hence applying the particle-hole transformation on electronic filling gives $n \to 2-n$. The transformation changes the self-consistent parameters μ, p and e (Eq. (107)) as follow:

For the chemical potential, we use the invariance under particle-hole symmetry of the Hubbard Hamiltonian. We obtain

$$\begin{aligned} H =& \sum_{ij\sigma} t_{ij} c^\dagger_{i\sigma} c_{j\sigma} + U \sum n_{i\uparrow} n_{i\downarrow} + \mu \sum_{i\sigma} n_{i\sigma} \\ &\to \sum_{ij\sigma} t_{ij} (-1)^{i+j} c_{i\sigma} c^\dagger_{j\sigma} + U \sum_i (-1)^{4i} c_{i\uparrow} c^\dagger_{i\uparrow} c_{i\downarrow} c^\dagger_{i\downarrow} - \mu \sum_{i\sigma} (-1)^{2i} c_{i\sigma} c^\dagger_{i\sigma} \\ &= \sum_{ij\sigma} t_{ij} c^\dagger_{j\sigma} c_{i\sigma} + U \sum_i (1 - n_{i\downarrow} - n_{i\uparrow} + n_{i\uparrow} n_{i\downarrow}) + \mu \sum_{i\sigma} n_{i\sigma} \\ &= \sum_{ij\sigma} t_{ij} c^\dagger_{i\sigma} c_{j\sigma} + U \sum_i n_{i\uparrow} n_{i\downarrow} + (\mu - U) \sum_{i\sigma} n_{i\sigma} + cste \end{aligned} \tag{123}$$

Thus, to keep the Hamiltonian invariant and therefore have under the particle-hole transformation $H \to H$, we need to impose

$$\mu(2-n) = -(\mu(n) - U) \tag{124}$$

For e and p we work directly with their respective definitions

$$\begin{aligned} e =& \langle \xi_{i\sigma} \xi^\dagger_{j\sigma} \rangle - \langle \eta_{i\sigma} \eta^\dagger_{j\sigma} \rangle \\ p =& \langle n_{i\sigma} n_{j\sigma} \rangle + \langle S^+_i S^-_j \rangle - \langle \Delta_i \Delta^*_j \rangle \end{aligned} \tag{125}$$

We use the particle-hole relations of the composite operators Eq. (121). For e we obtain

$$\begin{aligned} e(2-n) &\to (-1)^{i+j} (\langle \eta^\dagger_{i\sigma} \eta_{j\sigma} \rangle - \langle \xi^\dagger_{i\sigma} \xi_{j\sigma} \rangle) \\ &= \langle \eta_{j\sigma} \eta^\dagger_{i\sigma} \rangle - \langle \xi_{j\sigma} \xi^\dagger_{i\sigma} \rangle \\ &= -(\langle \xi_{i\sigma} \xi^\dagger_{j\sigma} \rangle - \langle \eta_{i\sigma} \eta^\dagger_{j\sigma} \rangle) \\ &= -e(n) \end{aligned} \tag{126}$$

We didn't kept the terms with δ_{ij} because e and p always appear with a t_{ij} prefactor and $t_{ij} = 0$ if $i = j$. We used the fact that i and j are always nearest neighbors to get $(-1)^{i+j} = -1$. For p, we have

$$\begin{aligned} p &\to (-1)^{2i+2j} \langle c_{i\sigma} c^\dagger_{i\sigma} c_{j\sigma} c^\dagger_{j\sigma} + c_{i\uparrow} c^\dagger_{i\downarrow} c_{j\downarrow} c^\dagger_{j\uparrow} - c^\dagger_{i\uparrow} c^\dagger_{i\downarrow} c_{j\downarrow} c_{j\uparrow} \rangle \\ &= \langle c_{j\sigma} c^\dagger_{j\sigma} - n_{i\sigma} c_{j\sigma} c^\dagger_{j\sigma} + S^-_i S^+_j - \Delta^*_j \Delta_i \rangle \\ &= \langle 1 - n_{j\sigma} - n_{i\sigma} + n_{i\sigma} n_{j\sigma} + S^+_j S^-_i - \Delta_i \Delta^*_j \rangle \\ &= 1 - \frac{n}{2} - \frac{n}{2} + p(n) \\ &= (1-n) + p(n) \end{aligned} \tag{127}$$

Therefore the particle-hole relation for the self-consistent parameters are the following

$$\begin{aligned} e(2-n) &= -\,e(n) \\ p(2-n) &= p(n) + (1-n) \\ \mu(2-n) &= U - \mu(n) \end{aligned} \tag{128}$$

In Fig. 19a, 19b and 19c we plot e, p and μ as a function of doping for the three solutions we studied (COM1, COM2 and Roth). The dashed-lines on the electron-doped region is the value the parameter must have to satisfy the particle-hole relations Eq. (128). We see that particle-hole symmetry is respected for every parameters for the three solutions.

We obtain a different result from Ref. [122]. It is possible to have a particle-hole symmetric solution which violates Pauli principle. This is indeed the case of the Roth solution which has a non vanishing C_0^{12} despite the fact it is zero analytically. The solution is particle-hole symmetric as long as C_0^{12} is not put to zero by hand in the self-consistent equations it must appear both in the equation of n and in the ϕ term in the equation of p.

Finally, note that applying this transformation on the composite bands ϵ^1 and ϵ^2 leads to

$$\begin{aligned} \epsilon_k^1(2-n) &= -\,\epsilon_{k+(\pi,\pi)}^2(n) \\ \epsilon_k^2(2-n) &= -\,\epsilon_{k+(\pi,\pi)}^1(n) \end{aligned} \tag{129}$$

5.3 . Superconductivity and Longer range hoppings

5.3.1 . Extension to superconductivity

Superconductivity can be studied by extending the initial basis. The new spinor ψ to consider is

$$\psi = \begin{pmatrix} \xi_{i\sigma} \\ \eta_{i\sigma} \\ \xi_{i\bar{\sigma}}^\dagger \\ \eta_{i\bar{\sigma}}^\dagger \end{pmatrix} \tag{130}$$

The method described before in Sec. 5 remains the same except for the **I** and **M** matrix which are now 4×4 matrices. Since we have chosen to make comparisons with cuprates when we will include longer range hoppings, we consider in this section only the case of d-wave superconductivity. Therefore, $\langle c_{i\uparrow} c_{i\downarrow} \rangle = 0$. Within this new basis, two currents add up to the two previously define in Eq. (105). After a bit of computation, we get the M and I matrices

$$I_{ij} = \delta_{ij} \begin{pmatrix} 1-\frac{n_i}{2} & 0 & 0 & 0 \\ 0 & \frac{n_i}{2} & 0 & 0 \\ 0 & 0 & 1-\frac{n_i}{2} & 0 \\ 0 & 0 & 0 & \frac{n_i}{2} \end{pmatrix} \qquad M_{ij} = \begin{pmatrix} m_{ij}^{11} & m_{ij}^{12} & m_{ij}^{13} & -m_{ij}^{13} \\ m_{ij}^{12} & m_{ij}^{22} & -m_{ij}^{13} & m_{ij}^{13} \\ m_{ij}^{13} & -m_{ij}^{13} & -m_{ij}^{11} & -m_{ij}^{12} \\ -m_{ij}^{13} & m_{ij}^{13} & -m_{ij}^{12} & -m_{ij}^{22} \end{pmatrix} \tag{131}$$

We used the paramagnetic assumption: $\langle n_{i\sigma} \rangle = \frac{n_i}{2}$. The coefficient of the M matrix m_{ij}^{11}, m_{ij}^{12} and m_{ij}^{22} are the same as in Eq. (106). In addition, the coefficient m_{ij}^{13} is defined by:

$$m_{ij}^{13} = -t\gamma_{ij}\theta_{ij} \tag{132}$$

γ_{ij} is a d-wave form factor we artificially added to enforce d-wave superconductivity. It is such that $\gamma_{i,i\pm\delta_y} = -\gamma_{i\pm\delta_x,i} = 1$ where δ_x/δ_y is the lattice constant along x/y axis.

The parameter θ is given by

$$\theta_{ij} = \langle c_{i\sigma} c_{i\bar{\sigma}} n_{j\sigma} \rangle \tag{133}$$

There is more in θ_{ij} than just superconductivity. For the sake of giving an intuition of this, we apply Wick theorem on θ_{ij} (this cannot be done since Wick theorem is only valid for weak correlations but it will give an insight of the physics)

$$\begin{aligned}\theta_{ij} =& \langle c_{i\sigma} c_{i\bar{\sigma}} \rangle n_{j\sigma} - \langle c_{i\sigma} c^\dagger_{j\sigma} \rangle c_{i\bar{\sigma}} c_{j\sigma} \\ &+ \langle c_{i\sigma} c_{j\sigma} \rangle c_{i\bar{\sigma}} c^\dagger_{j\sigma} - \langle c_{i\bar{\sigma}} c_{j\sigma} \rangle c_{i\sigma} c^\dagger_{j\sigma} + ...\end{aligned} \tag{134}$$

From this hand wavy decoupling it appears θ_{ij} is composed of superconducting channels (showed by the charge 2 correlations of type $\langle cc \rangle$), but also of bond-charge ($\langle c^\dagger_{i\sigma} c_{j\sigma} \rangle$) and spin flip hopping ($\langle c^\dagger_{i\sigma} c_{j\bar{\sigma}} \rangle$) channels. Since we impose d-wave symmetry by mean of the d-wave γ_{ij} factor in Eq.(132), all the superconducting channels except the one associated to the d-wave symmetry $\langle c_{i\bar{\sigma}} c_{j\sigma} \rangle$ will be assumed to be negligible. θ_{ij} can therefore been seen as an anomalous d-wave superconductivity mean field parameter, and it also involves spin and charge correlations. Since we consider singlet pairing, we have

$$\langle c_{i\sigma} c_{i\bar{\sigma}} n_{j\sigma} \rangle = \langle c^\dagger_{i\bar{\sigma}} c^\dagger_{i\sigma} n_{j\sigma} \rangle \tag{135}$$

We can still apply translational invariance to treat p, n and e as a constant. We can do likewise for θ. The self-consistent equations remain the same for n and e since they are only one body correlations. However extending the basis changes the self-consistent equations of p_{ij} and θ_{ij}. We obtain (cf appendix C for details)

$$\begin{cases} p &= \frac{n^2}{4} - \frac{\rho_1 + \phi\rho_2}{1-\phi^2} - \frac{\rho_1 - \rho_2}{1-\phi} - \frac{\rho_3}{1+\phi} \\ \theta &= \frac{\zeta}{1+\phi} \end{cases} \tag{136}$$

With

$$\begin{cases} \phi &= -\frac{2}{2-n}(C_0^{11} + C_0^{12}) + \frac{2}{n}(C_0^{12} + C_0^{22}) \\ \rho_1 &= \frac{2}{2-n}(C^{11} + C^{12})^2 + \frac{2}{n}(C^{22} + C^{12})^2 \\ \rho_2 &= \frac{2}{2-n}(C^{13} + C^{14})^2 + \frac{2}{n}(C^{23} + C^{24})^2 \\ \rho_3 &= \frac{4}{n(2-n)}(C^{11} + C^{12})(C^{22} + C^{12}) \\ \zeta &= \frac{2}{2-n}(C^{11} + C^{12})(C^{13} + C^{14}) + \frac{2}{n}(C^{12} + C^{22})(C^{23} + C^{24}) \end{cases} \tag{137}$$

Let us note that this decoupling is not unique. Several choices can be made (an example of this can be found in appendix C). These choices give similar results but tend to overestimate or underestimate some quantities, depending on which regime we consider [132]. Following the original suggestion of L. Roth [101], we should symmetrize the different possible decoupling. Beside the size of the matrices,

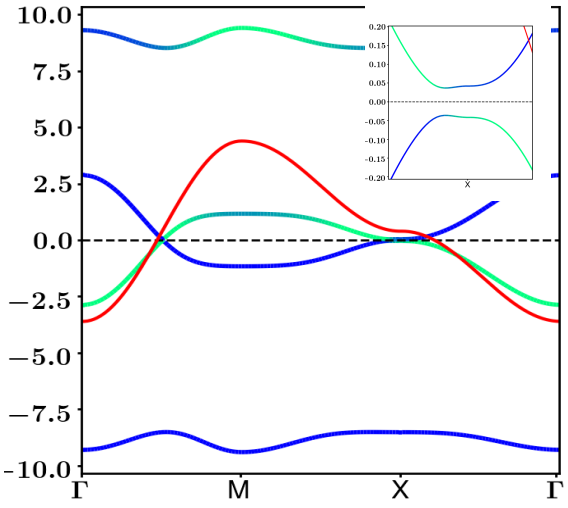

(a) Bands for the Roth solution

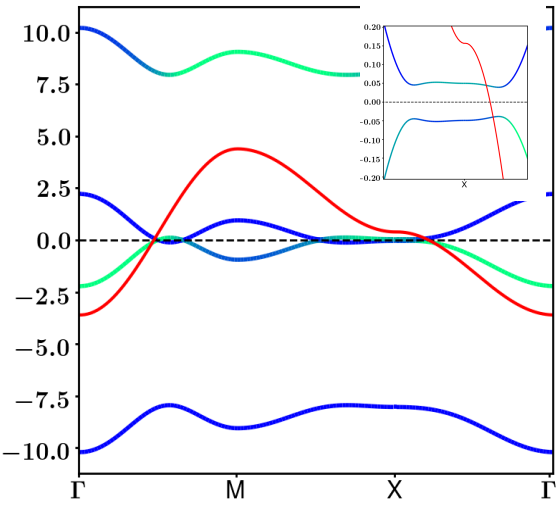

(b) Bands for the COM2 solution

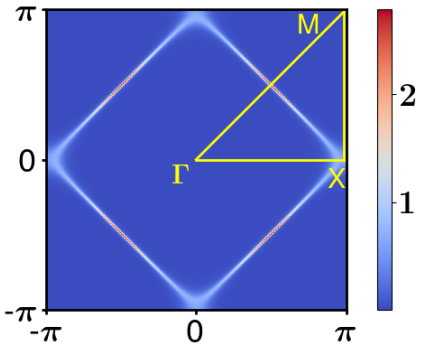

(c) Fermi Surface for the Roth solution

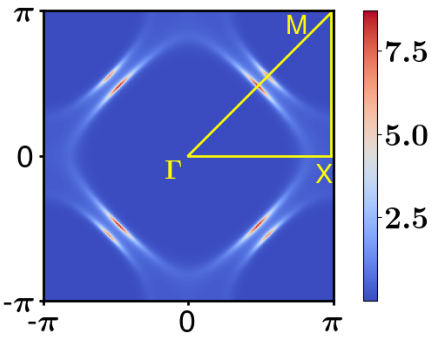

(d) Fermi Surface for the COM2 solution

Figure 21: Bands and Fermi Surface with superconductivity at $t = 1$, $U = 8t$ and $T = 0$ respectively for (a) Roth solution at $n = 0.8$ (b) COM2 at $n = 0.9$. These are the respective doping at which superconductivity is maximum. We observe a doubling of the bands associated to the doubling of the basis. The spectral weight, overlapped in colors is also particle-hole symmetric. The insets on the top plots correspond to a zoom around zero energy of the bands: we see a gap opening at **k**=$(\pi, 0)$. There is no gap opening between **k**=$(0, 0)$ and **k**=(π, π) because of d-wave symmetry. The associated Fermi surfaces of (c) and (d) have been plotted with some broadening, as it is made only of one nodal point between Γ due to d-wave symmetry and the gap opening.

everything else remain the same: the expression of $\boldsymbol{\sigma}$ from Eq. (102) remains unchanged, but will involve 4×4 matrices.

On Fig. 21 we plot the bands for the Roth and COM2 solutions. There is a doubling of the bands

due to the particle-hole symmetry of the basis: we have four distincts eigenvalues ϵ^l of the E matrix verifying the property $\epsilon^1 = -\epsilon^3$ and $\epsilon^2 = -\epsilon^4$. Beside this doubling, the bands are almost unmodified compared to what we had without superconductivity. Only one difference can be seen: a gap opening at $(\pi, 0)$. We performed a zoom around zero energy in order to see the gap better on the insets. The presence of the gap also appears on the Fermi surface: there is less weight near the $(\pi, 0)$ compared to what we had in Fig. 12 without superconductivity.

On Fig. 22a, we plot the parameter θ as a function of the electron density n for the COM2 and the Roth solutions. The dashed-line corresponds to the usual d-wave superconducting order parameter $\Delta^d_{ij} = \langle c_{i\sigma} c_{j\bar{\sigma}} \rangle$. We can recover it directly from the correlation functions involving nearest-neighbors $C^{nm}_{ij} = \langle \psi^n_i (\psi^m_j)^\dagger \rangle$ using the following equation

$$\Delta^d_{ij} = C^{13}_{ij} + C^{14}_{ij} + C^{23}_{ij} + C^{24}_{ij} \tag{138}$$

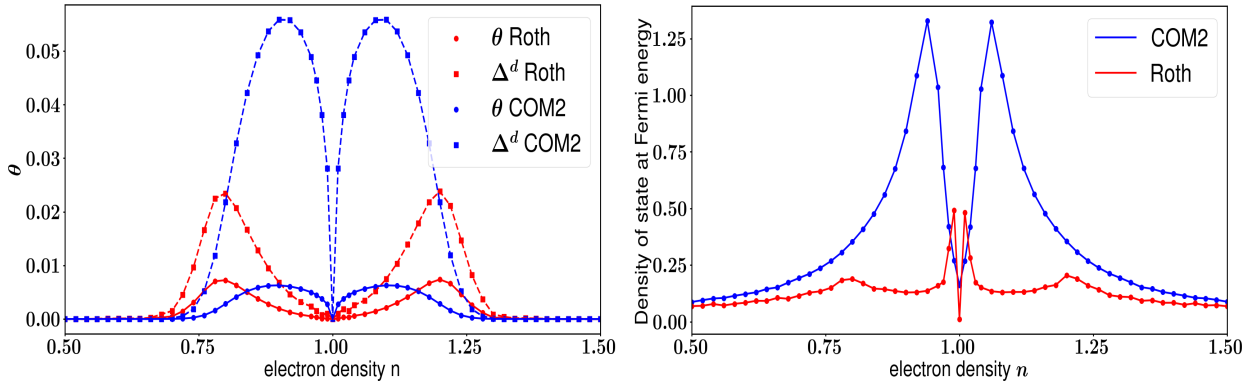

(a) θ and Δ^d parameters as a function of n

(b) Density of states at the Fermi Energy.

Figure 22: (a): Anomalous superconducting mean field parameter θ as a function of doping for Roth minimization and Pauli minimization (COM2 solution). θ satisfy particle-hole symmetry in both cases. The dashed lines corresponds to the d-wave superconducting order parameter Δ^d. (b): Density of states at the Fermi energy with no superconductivity. We see a clear correlation between enhancement of the density of states and superconductivity. θ and Δ^d are maximum at the Van Hove singularity. It lies at n=0.8 for Roth and around n=0.9 for COM2, as shown in Fig. 21.

The maximum of θ and Δ^d are at the same electron density. For the Roth solution this corresponds to n=0.8, while for the COM2 solution it is around n=0.9. We already showed that n=0.8 corresponds to the Van Hove singularity for the Roth solution in the discussion of Fig. 16 and 17. This is in agreement with other studies [105] [102]. The same phenomenon occurs for the COM2 solution. In Fig. 21 we plotted the bands and Fermi surfaces for the COM2 solution at n=0.9 where superconductivity is maximum. Beside the gap opening, the band for COM2 exhibits some flatness at $(\pi, 0)$ and its Fermi Surface is almost diamond-like. We plot the density of states at the Fermi energy as a function of electron density on Fig. 22b. Let us note we did not considered superconductivity to compute this density of states (otherwise there would be a superconducting gap). The density of states was computed using Eq. (115) at $\omega = 0$. There is a clear correspondence between the maximum of superconductivity and

of the density of states at the Fermi energy, both for Roth (at n=0.8) and COM2 (at n=0.9). For the Roth solution a maximum can be found near half-filling but this maximum is associated with Mott physics and does not improve superconductivity because it is too close to half-filling. The local maximum at n=0.8 due to Van Hove singularity is the one relevant in the enhancement of superconductivity.

We checked that the θ parameter also verifies the following particle-hole symmetry

$$\theta \to \theta^* \tag{139}$$

In order to satisfy particle-hole symmetry, there must be another maximum of θ, therefore another Van Hove singularity in the electron doped regime. On Fig. 22b, we indeed see another peak both for superconductivity and the density of states in the $n > 1$ area. They correspond to the particle-hole symmetric of the peaks in the hole doped region.

In this method, the gap opening observed on the bands in Fig. 21 is of the order of Δ^d, as it is expected. The value of θ affects both superconductivity and the density n, since θ involves both quantities.

5.3.2 . Bands and Luttinger theorem with longer ranged hopping

We now want to consider the effect of higher hopping terms in order to get closer to more realistic materials. We want to see if the results we had with nearest-neighbours hoppings on the bands, the validity of the Luttinger theorem and superconductivity are modified by further hoppings. Including at least next nearest neighbors in the model is enough to break the particle-hole symmetry. We will only consider the Roth solution in this section, since COM2 and COM1 solutions have been studied with next-nearest neighbors in Ref. [123], and Roth presents Fermi surface closer to what is observed by ARPES for cuprates.

From now on we will consider four different sets of tight-binding parameters all corresponding to a square lattice as described in Fig. 23.

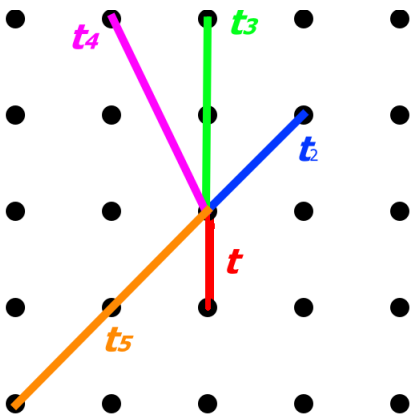

Figure 23: Representation of the five longer ranged hopping parameter considered in this section for a square lattice.

These tight-binding parameters correspond to cuprates Bi2212 and LSCO, which are strongly correlated. Their values, taken from Ref. [133],are given in Table 1. They are such that the energy for a

tight binding model of a square lattice is given by

$$\begin{aligned}\epsilon_{tb}(k) = 2t(cos(k_x) + cos(k_y)) + 4t_2 cos(k_x)cos(k_y) + 2t_3(cos(2k_x) + cos(2k_y)) \\ + 4t_4(cos(k_x)cos(2k_x) + cos(2k_x)cos(k_y)) + 4t_5 cos(2k_x)cos(2k_y)\end{aligned} \tag{140}$$

In the following we will normalize every plots so we have t=1 (we will divide every tight binding parameter by t in absolute value).

	t	t_2	t_3	t_4	t_5
tb1	-0.2956	0.0818	-0.0260	-0.0280	0.0255
tb2	-0.3399	0.1184	-0.0397	0.0086	0.0006
tb3	-0.2941	0.0731	0.0048	-0.0325	0.0035
tb4	-0.3912	0.0370	-0.0294	-0.0350	-0.0087

Table 1: Values of the 4 tight bindings we are going to consider. tb1 is based on an ARPES fit of Bi2212. tb2 corresponds to the bonding surface of Bi2212, tb3 is a modified version of tb2 to get a flatter band and tb4 corresponds to underdoped LSCO.

In this section we include hoppings up to t_5 and study the bands and Fermi surface behavior. With additional hopping terms, only the expression of the matrix **M** changes. In addition to the α^1_{il} parameter appearing in Eq. (106) higher hopping terms will appear in the **M** matrix. It becomes

$$\begin{aligned} m^{11}_{ij} =& -\mu(1-\frac{n_i}{2})\delta_{ij} - \sum_{k=1}^{N} t\left[\alpha^k_{ij}(1-\frac{n_i+n_j}{2}+p_{ij}) + \delta_{ij}\sum_l \alpha^k_{il}e_{il}\right] \\ m^{12}_{ij} =& \sum_{k=1}^{N} t\left[\alpha^k_{ij}(\frac{n_j}{2}-p_{ij}) - \delta_{ij}\sum_l \alpha^k_{il}e_{il}\right] \\ m^{22}_{ij} =& -(\mu-U)\frac{n_i}{2}\delta_{ij} + \sum_{k=1}^{N} t\left[\alpha^k_{ij}p_{ij} - \delta_{ij}\sum_l \alpha^k_{il}e_{il}\right] \end{aligned} \tag{141}$$

where

$$\begin{cases} \alpha^N_{il} &= 1 \quad \text{if i and l are } \overbrace{\text{next-...}}^{N-1 \text{ times}} \text{-nearest neighbour} \\ \alpha^N_{il} &= 0 \quad \text{Otherwise} \end{cases} \tag{142}$$

Each new hopping considered adds a term in the tight-binding Hamiltonian which is then added in the **M** matrix. The parameters p and e depend on bonds i-j, so we should make a distinction between e^1_{ij} with i and j nearest neighbors (NN), e^2_{ij} with i and j next nearest neighbors (NNN)... e^n_{ij} and p^n_{ij} will be associated with their corresponding hopping as in Fig. 23. Translational invariance still allows us to treat e^1, e^2,...,e^5, p^1, p^2,...,p^5 as constants. Correlation functions $\mathbf{C}_{ij} = \langle\psi_i;\psi^\dagger_j\rangle$ are at different sites too, so we will also have to make a distinction in the self-consistent equations between $\mathbf{C}^1$ for NN, $\mathbf{C}^2$ for NNN and so on.

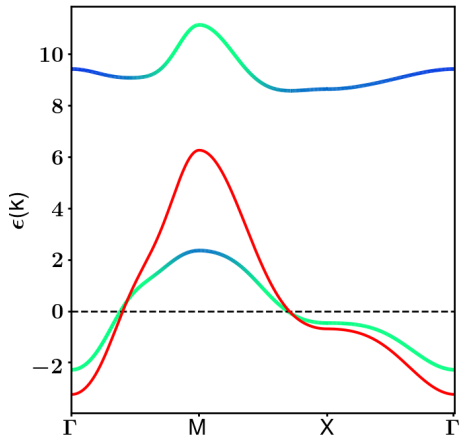

(a) tb1: ARPES fit Bi2212

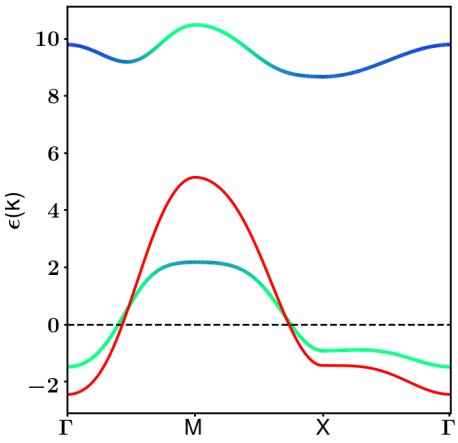

(b) tb2: fit of bonding surface of Bi2212

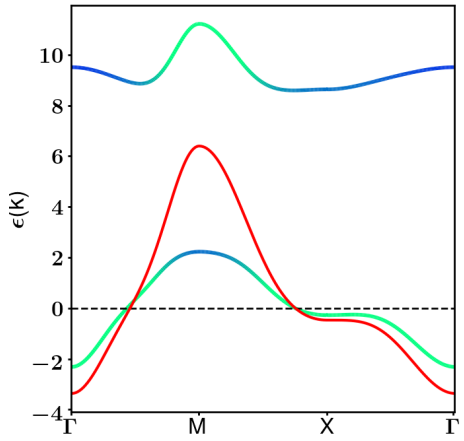

(c) tb 3: Modified tb2 (cf [133])

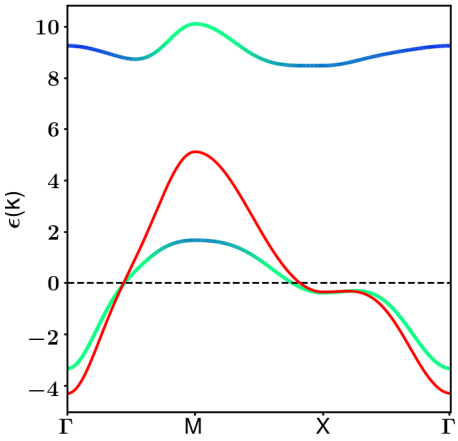

(d) tb 4: underdoped LSCO

Figure 24: Bands obtained using Roth minimization with hoppings up to order 5. The overlapped colors are the spectral weight, and the same waterfall feature as described in Sec. 5.2.1 is observed. The tight bindings parameters are taken from Ref [133] and are given in table I. The red line is the non-interactive, tight binding dispersion. We consider n=0.8 and U=8t.

Fig. 24 presents the bands we obtain for Roth solutions for the four sets of tight-binding parameters in Table. (1). In Fig. 25 and 26 we plotted respectively the Fermi surfaces obtained with the method and the Fermi surfaces of the non-interactive tight-binding dispersions (corresponding to Eq. (140)). In the hole doped regime, the Fermi surface we obtained from the Roth solution has the same general shape as the non interacting Fermi Surface. This is expected since despite being non-interactive, the tight-binding parameter taken from table 1 are fitted from ARPES experiment of

strongly correlated materials. The composite operators method produces Fermi surfaces that appear to be smaller/larger than the tight-binding ones. This is in agreement with the violation of the Luttinger theorem observed with nearest-neighbour hopping, and indicates that it is still violated with further hoppings. We checked the opposite situation is accordingly observed in electron doped area: the Fermi Surface obtained with the method is at a lower doping than the non interacting one. Let us note that although the specific shape of the dispersions are different due to the characteristics of the considered tight-binding parameters, the symmetry point are the same (one saddle point, one maximum and one minimum).

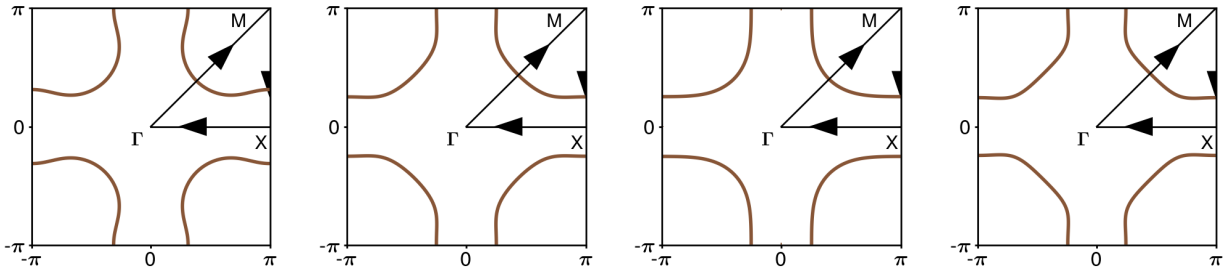

Figure 25: Fermi Surfaces renormalized by the composite operator methods using Roth minimization with the parameters of Ref [133]. We consider n=0.8 and U=8t. Top left: tb1, top right: tb2, bottom left: tb3, bottom right: tb4.

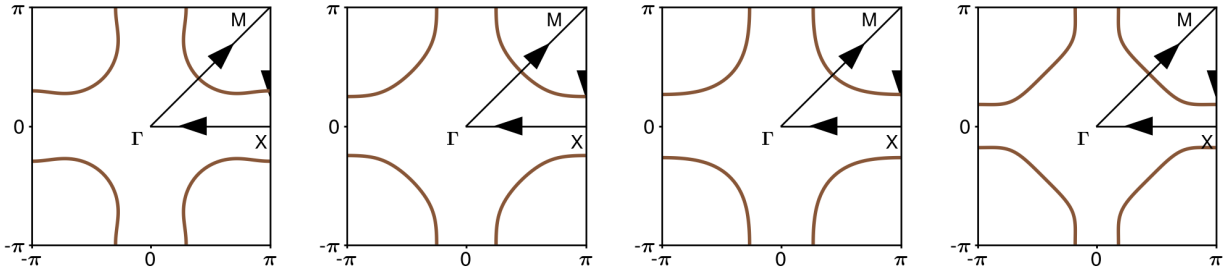

Figure 26: Non interacting (NI) Fermi Surfaces for the parameters of Ref [133] at 20% hole doping. Top left: tb1, top right: tb2, bottom left: tb3, bottom right: tb4.

In the following we study the particle-hole symmetry and the Luttinger theorem violation with next-nearest neighbours. For the sake of simplicity we restrict ourselves to next-nearest neighbors in this part. Next-nearest neighbors hopping parameter t_2 breaks translational invariance because of the hopping term of the Hamiltonian which transform as follow:

$$\sum_{ij} t_{ij} c^{\dagger}_{i\sigma} c_{j\sigma} \rightarrow -\sum_{ij} t_{ij} (-1)^{i+j} c^{\dagger}_{i\sigma} c_{j\sigma} \tag{143}$$

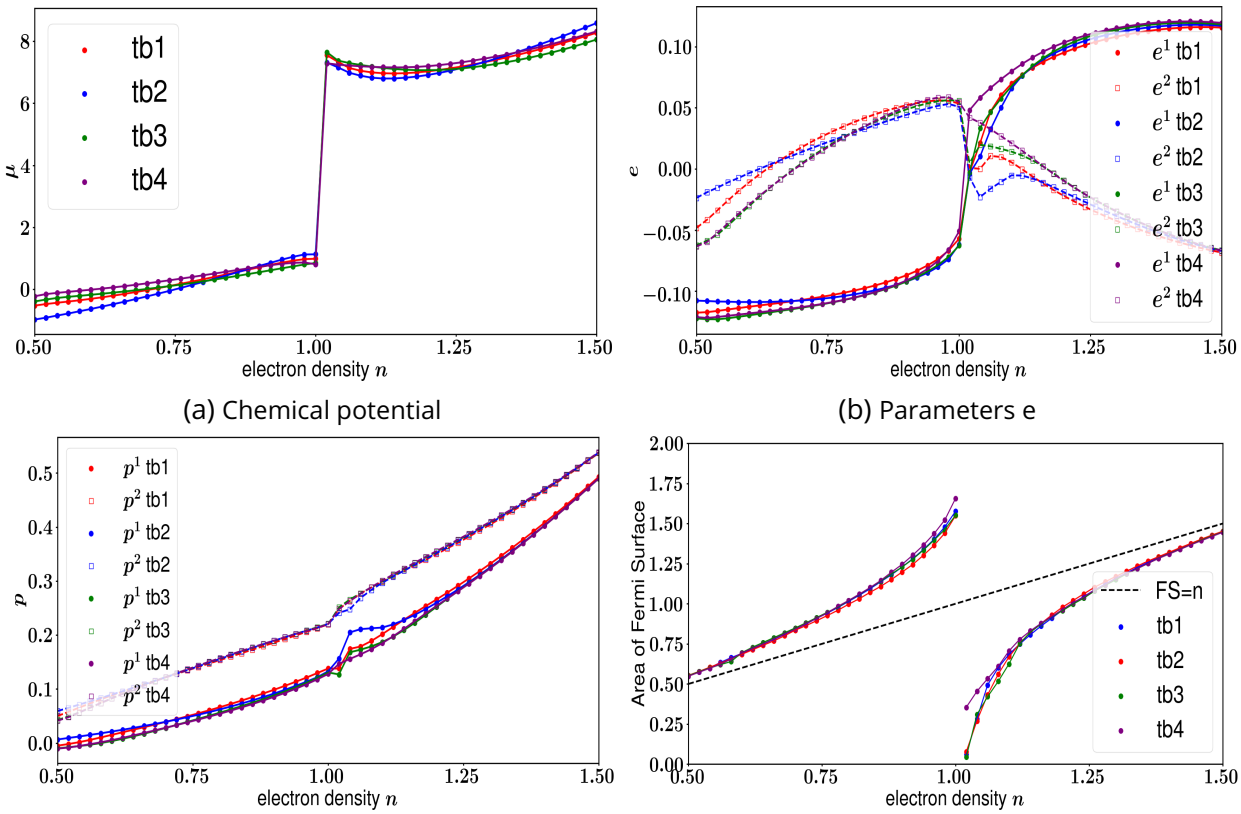

(a) Chemical potential

(b) Parameters e

(c) Parameters p

(d) Luttinger Violation

Figure 27: (a), (b) and (c) :Parameters as a function of doping for each tight binding with next nearest neighbors. The circles corresponds to p1 and e1 (NN) while the squares corresponds to p2 and e2 (NNN). (d) : Luttinger violation for each tight binding.

For i and j next-nearest neighbour we have $(-1)^{i+j} = 1$. The Hamiltonian is therefore not invariant if t_2 is included because it changes sign. We are now going to check the parameters are indeed not going to follow the particle-hole symmetry. An interesting question is to know whether the nearest-neighbor quantities like e^1 and p^1 are still particle-hole symmetric or if they are affected by the presence of t_2.

For n and μ, the transformation is the same as with the nearest neighbors case:

$$\begin{aligned} n &\to 2 - n \\ \mu &\to U - \mu \end{aligned} \tag{144}$$

For the bond variables e_{ij} and p_{ij}, we already know the transformation for p^1 and e^1. The only difference for p^2 and e^2 comes from the $(-1)^{i+j}$ term. p^2 will not be affected because it involves only two bodies operators. Thus only e^2 has an additional minus sign under the transformation. Therefore

the particle-hole transformation on the parameters leads to:

$$\begin{aligned} p^1 &\to 1 - n + p^1 \\ p^2 &\to 1 - n + p^2 \\ e^1 &\to -e^1 \\ e^2 &\to e^2 \end{aligned} \tag{145}$$

In Figs. 27a, 27b and 27c we plot the parameters μ, e and p as a function of doping for the four considered tight-binding parameters of Table. (1), only considering t and t_2. Parameters e^2 and p^2 indeed break the particle-hole symmetry from Eq. (145). The chemical potential, as well as e^1 and p^1 behave as in the nearest neighbor case, so they remain particle-hole symmetric.

Finally we can again study the Luttinger theorem. In Fig. 27d, the area of the Fermi surface is plotted as a function of electron density. Interestingly we observe an analogous behavior as in the nearest-neighbor case. The Luttinger violation does not seem to be affected by the presence of next-nearest neighbors hoppings and is barely changed when we modify tight-binding parameters. As already mentioned before, the Luttinger theorem is strongly violated around half filling and is recovered further away. This confirms why in the previous section the Fermi surfaces seemed to be at a higher doping than the electron density we considered when we are in the hole doped regime (and conversely, at a lower doping in the electron doped regime).

5.3.3 . Superconductivity with longer ranged hoppings

In this section we again consider hoppings up until t_5, and we implement superconductivity. We will assume again a d-wave symmetry and only consider nearest-neighbor pairing. As before, the **M** and **I** matrices become 4x4 and have the same symmetries as the nearest neighbours case. The **I** matrix is independent of t and t' and is thus the same as before. The main difference is that the coefficients m_{ij}^{11}, m_{ij}^{12} and m_{ij}^{22} are now given by Eq. (141). m_{ij}^{13} stays identical to its expression in the nearest neighbor case since we only consider superconductivity for nearest neighbors. Therefore m_{ij}^{13} is proportional to the θ parameter, defined the same way as previously ($\theta_{ij} = \langle c_{i\uparrow} c_{i\downarrow} n_{j\sigma} \rangle$).

In Fig. 28a, the θ and Δ^d parameters are plotted as a function of electron density for the four tight-binding parameters with the Roth solution. Since we have included further neighbors, θ is not particle-hole symmetric anymore. In Fig. 28b, we plotted the density of states at the Fermi energy without superconductivity using Eq. (115) at $\omega = 0$ (in order to see the peaks with no superconducting gap). In Fig. 28c and 28d, we plotted without and with superconductivity the bands at electron densities corresponding to the maximum of the density of states for tb3 when the system is hole doped ($n \approx 0.6$). The bands with no superconductivity on 28c are flats at the Fermi energy. This proves that the maximum of Fig. 28b correspond to the Van Hove singularity. On 28d we see in the inset the gap at $(\pi, 0)$ is again of the order of $2\Delta^d$. The maximum of the θ and Δ^d parameters are thus at the same electron density as the Van Hove singularity. Hence, the situation is the same as in the nearest-neighbor case. In Table 2 we give the electron densities associated to the Van Hove singularities for the four sets of tight-binding parameters. Let us note there is no proportionality between the peak in the density of states and Δ^d: it is different for every set of tight-binding parameters. This is seemingly a consequence of the electronic correlations which are treated differently for each tight-binding parameters as a consequence of the main approximation of the method Eq. (88).

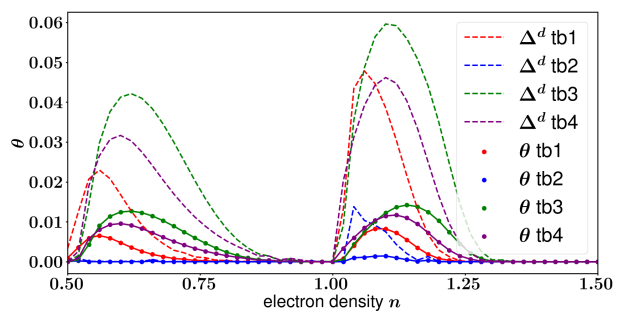

(a) θ and Δ^d

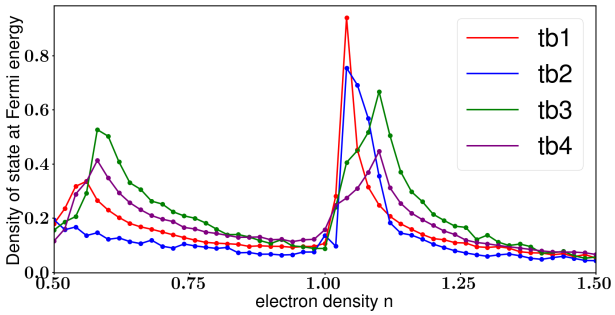

(b) Density of states at the Fermi energy

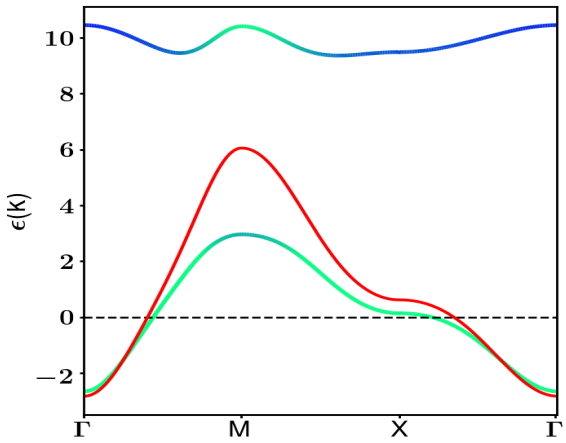

(c) no superconductivity

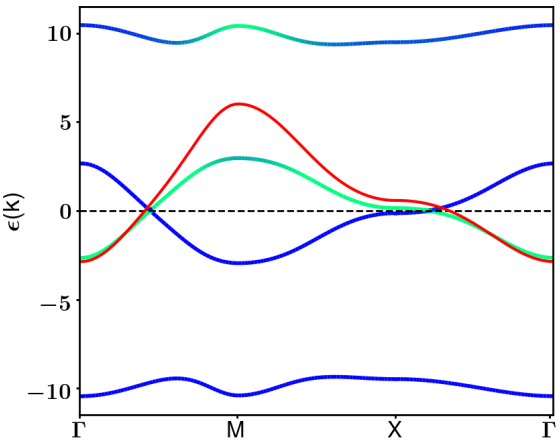

(d) with superconductivity

Figure 28: (a): Anomalous superconducting order parameter θ as a function of doping for the four sets of tight bindings parameters with Roth minimization. The dashed line corresponds to the usual d-wave superconducting order parameter we rebuilt from the correlation function. We are at U=8t. (b): Density of states (with no superconductivity in order to see the peaks) at the Fermi energy. The 2 peaks corresponds to the 2 Van Hove singularity in hole and electron doping respectively. To illustrate this the bottom plots (c) and (d) are the bands at the Van Hove singularity with tight binding parameters tb3 at n=0.6 respectively with: (c) no superconductivity, where we clearly see the flat band associated to Van Hove singularity (d) with superconductivity, the gap is located around X and is of the order of Δ^d.

The most striking feature is that superconductivity in the method seems to be induced by the proximity of the Van Hove singularity. This was already the case with nearest neighbors but this property seems unaffected by further hopping terms. For cuprates there exist a consensus that antiferromagnetism is the interaction necessary to explain the pairing mechanism [134]. This has also the advantage to explain why experimentally superconductivity is observed around 15% hole doping. Since this method predicts superconductivity only close to the Van Hove singularity, it is non zero at some doping values which does not correspond to what is expected. This flaw is maybe a

	tb1	tb2	tb3	tb4
Van Hove (electron)	1.04	1.05	1.10	1.11
Van Hove (hole)	0.57	0.45	0.6	0.58

Table 2: Electron density at which there is a Van Hove singularity at the chemical potential. At this values a flat band lies at the Fermi energy and the associated Fermi surface is diamond like. These singularities occur both in electron and in hole.

consequence of the main hypothesis of the method: it is maybe necessary to consider dynamical corrections to the self-energy in order to observe a different behavior for superconductivity.

6 . Two orbital Hubbard model with inter-orbital hopping

6.1 . Description of the model and limit case studies

6.1.1 . Model and physical motivations

Unlike in cuprates, in iron-based superconductors, there is no Mott-Insulator phase close to the superconductor phase. Instead, there is a metallic phase with spin order. In this context, the question of the reconstruction of the Fermi Surface due to electron interactions have been extensively studied [135] [136]. A local loss of spectral weight in the Fermi surface upon doping or temperature change has been observed. It is associated to the unhybridization of one of the d orbital (usually d_{xy}) [137]. Such phase has been called orbital Selective Mott phase (OSMP). The main ways to describe this phase involves either Hund's coupling [76] or Hubbard interaction with inter-orbital hopping [138].

In this section we will show an OSMP phase was achieved with a two orbitals Hubbard Hamiltonian with an inter-orbital hopping term by mean of composite operator method. We consider the following Hamiltonian:

$$H = -\sum_{ij\alpha\sigma} t_{ij}^{\alpha} c_{i\alpha\sigma}^{\dagger} c_{j\alpha\sigma} - \sum_{i\sigma\alpha} \mu^{\alpha} n_{i\alpha\sigma} - \lambda \sum_{i\sigma} (c_{ix\sigma}^{\dagger} c_{iy\sigma} + c_{iy\sigma}^{\dagger} c_{ix\sigma}) + \sum_{i\alpha} U^{\alpha} n_{i\alpha\uparrow} n_{i\alpha\downarrow} \tag{146}$$

Where $c_{i\alpha\sigma}^{\dagger}$ creates an electron on site i with spin $\sigma \in \{\uparrow, \downarrow\}$ on orbital $\alpha \in \{x, y\}$. $c_{i\alpha\sigma}$ will destroy such electron, and $n_{i\alpha\sigma}$ is 1 if an electron is on the lattice at site i on orbital α with spin σ, and 0 otherwise. t_{ij}^{α} is the intra orbital kinetic energy, with chemical potential μ^{α}. The λ term is a inter-orbital hopping. Finally, U^{α} denotes the intra-orbital Coulomb repulsion. We start by studying the limit case (atomic limit and non-interacting, since the $\lambda = 0$ limit has been studied in the previous section and would simply lead to two identical orbital following the same physics as detailed in Sec. 5).

6.1.2 . Non-interacting limit (no U)

In the non-interacting limit, we do not consider any Coulombian interaction. In this case, the Hamiltonian becomes:

$$H_{NI} = -\sum_{ij\alpha\sigma} t_{ij}^{\alpha} (c_{i\alpha\sigma}^{\dagger} c_{j\alpha\sigma} + c_{j\alpha\sigma}^{\dagger} c_{i\alpha\sigma}) - \lambda \sum_{i\sigma} (c_{ix\sigma}^{\dagger} c_{iy\sigma} + c_{iy\sigma}^{\dagger} c_{ix\sigma}) - \sum_{i\sigma\alpha} \mu^{\alpha} n_{i\alpha\sigma} \tag{147}$$

This Hamiltonian is diagonalizable in Fourier space. To simplify the picture we consider in this section a 1D chain. Thus, it can be rewritten as:

$$\begin{cases} H_{NI} &= \sum_{k} \mathcal{H}_k \\ \mathcal{H}_k &= \sum_{\alpha\sigma} \epsilon_k^{\alpha} (c_{k\alpha\sigma}^{\dagger} c_{k\alpha\sigma} - \lambda \sum_{k\sigma} (c_{kx\sigma}^{\dagger} c_{ky\sigma} + c_{ky\sigma}^{\dagger} c_{kx\sigma}) \end{cases} \tag{148}$$

With $\epsilon_k^{\alpha} = -2t^{\alpha} cos(k) - \mu^{\alpha}$ the tight-binding dispersion for a 1D chain. Introducing the Nambu spinor $c_i = (c_{ix} c_{iy})$ the Hamiltonian rewrite:

$$\mathcal{H}_k = \begin{pmatrix} \epsilon_k^x & -\lambda \\ -\lambda & \epsilon_k^y \end{pmatrix} \tag{149}$$

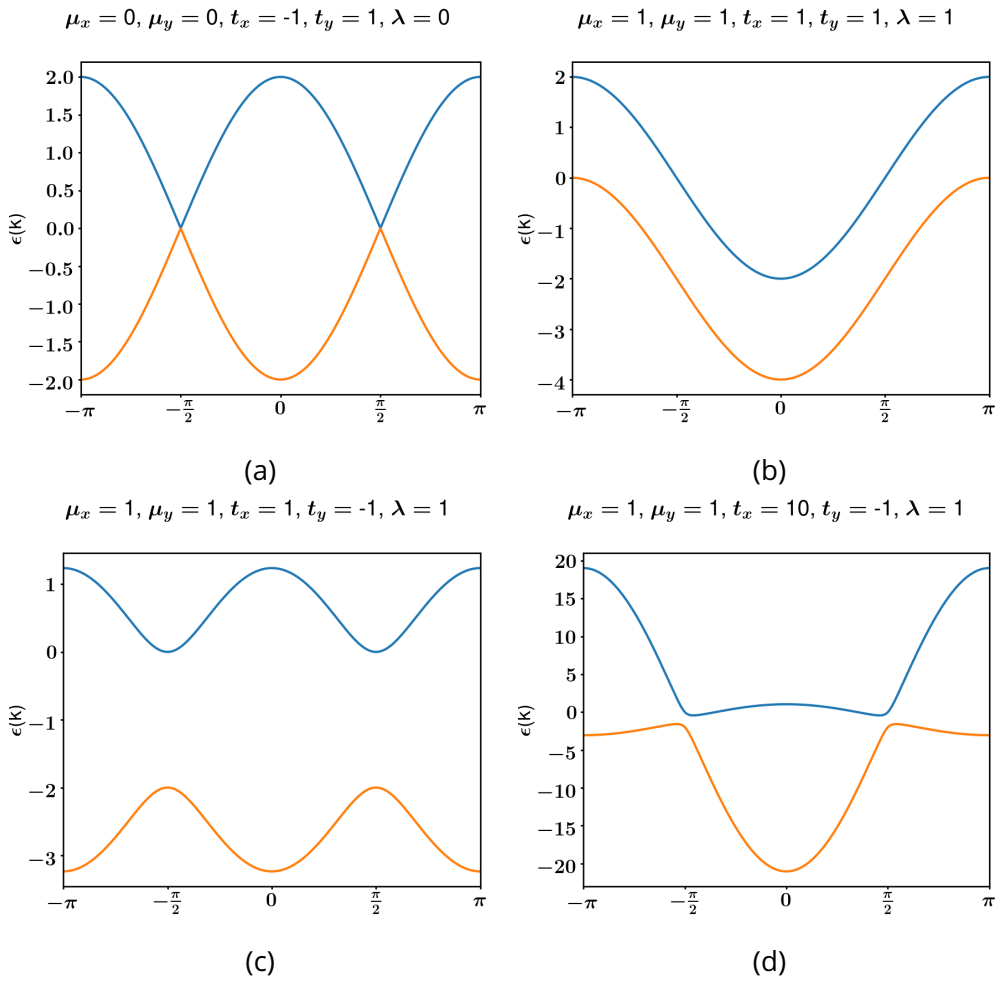

Figure 29: Bands of the 1D chain with no interaction for various values of the parameters. (a) In the absence of λ and for $t_x = -t_y$ the eigenvalues are particle-hole symmetric as one can expect. (b) A splitting is created because of λ of the two bands. (c) & (d) λ systematically opens a gap of 2λ, whatever the bandwidth or chemical potential (as long as they are taken equal).

Spin is not considered in this basis because $\mathcal{H}_k$ is spin degenerate (the off diagonal blocks connecting σ to $\bar{\sigma}$ are equal to zero). Therefore, the two spin-degenerate eigenvalues of this Hamiltonian are:

$$e_k^{\pm} = \frac{\epsilon_k^x + \epsilon_k^y \pm \sqrt{(\epsilon_k^x - \epsilon_k^y)^2 + 4\lambda^2}}{2} \tag{150}$$

This expression simplifies in the case $t^x = t^y$ and $\mu^x = \mu^y$ into:

$$e_k^{\pm} = \epsilon_k \pm \lambda \tag{151}$$

In that case, the non interacting limit bands are composed of two tight-binding bands split by a gap of 2λ.

It is also instructive to consider the situation with $t^x \neq t^y$. In Fig. 29 we plot various parameters regimes. At vanishing λ, the two eigenvalues are degenerate (particle-hole symmetric if $t_x = -t_y$) and describe the regime of Sec. 5. λ splits the band and opens up a gap of different size depending on the values of $\mu^x - \mu^y$ and $t^x - t^y$ as shown by Eq. 150. This gap is thus always observable but for larger bandwidth may appear negligible.

It is important to note that these bands are not directly associated to orbitals but to combination of these orbitals. The eigenvectors of these bands indeed involve a mixture of the x and y orbitals.

6.1.3 . Atomic limit (no t)

In the atomic limit term, the bands are now local. Therefore there won't be any momentum dependency and we have discrete energy levels. For simplicity, we will then consider one site with its two orbitals. The Hamiltonian in this limit (at $\mu = 0$ and $U^x = U^y$ for simplification) is:

$$H_{AL} = -\lambda \sum_{\sigma} (c^{\dagger}_{x\sigma} c_{y\sigma} + c^{\dagger}_{y\sigma} c_{x\sigma}) + U \sum_{\alpha} n_{\alpha\uparrow} n_{\alpha\downarrow} \tag{152}$$

Let us first notice that the total number of charges commutes with this Hamiltonian. The total hamiltonian is block diagonal in the charge sector. Thus we can consider independently each of these block matrices associated to a certain number of charges (0 for the doubly empty site to 4 for the doubly occupied).

At half-filling we consider the following charge 2 basis:

$$\mathcal{B}_2 = \{|\uparrow\downarrow_x, 0_y\rangle, |0_x, \uparrow\downarrow_y\rangle, |\uparrow_x, \downarrow_y\rangle, |\downarrow_x, \uparrow_y\rangle\} \tag{153}$$

The state $|\sigma_x, \sigma_y\rangle$ is not relevant because the application of H_{AL} to it always make it vanish. The Coulomb term is going to give 0 if we apply the two states with single occupied orbitals. The two doubly occupied states are eigenvector of this term with eigenvalue U. Meanwhile the λ term transform two single occupied orbital into one double occupied orbital and the other one empty. Therefore, in the $\mathcal{B}_2$ basis, we have:

$$H^2_{AL} = \begin{pmatrix} U & 0 & -\lambda & -\lambda \\ 0 & U & -\lambda & -\lambda \\ -\lambda & -\lambda & 0 & 0 \\ -\lambda & -\lambda & 0 & 0 \end{pmatrix} \tag{154}$$

The eigenvalues of this hamiltonian are:

$$\begin{cases} e_0 = 0 \\ e_U = U \\ e_{\pm} = \frac{U \pm \sqrt{U^2 + 16\lambda^2}}{2} \end{cases} \tag{155}$$

In the case of a large U, e_0 and e_U correspond to the lower and upper Hubbard bands from the Mott-Insulator physics. It is important to note that e_0 is three fold degenerate because of the $|\sigma_x, \sigma_y\rangle$ states. Then,

$$\begin{cases} e_+ \approx U + 4\frac{\lambda^2}{U} \\ e_- \approx -4\frac{\lambda^2}{U} \end{cases} \tag{156}$$

$e_\pm$ represents the gap opened by λ. In the $U \to \infty$ limit, this gap tends to 0 and $e_- \to 0$, $e_+ \to U$, only the lower and upper Hubbard bands picture remain.

In the other limit where λ dominates over U, we have

$$\begin{cases} e_+ & \approx 2\lambda + \frac{U}{2} + \frac{U^2}{16\lambda} \\ e_- & \approx -2\lambda + \frac{U}{2} - \frac{U^2}{16\lambda} \end{cases} \tag{157}$$

Interestingly, in this limit U is not completely washed out by λ in the sense that e_0 and e_U remain different than $e_\pm$ in the $\lambda \to \infty$ limit.

If we only consider one electron, the charge 1 basis is:

$$\mathcal{B}_1 = \{|\uparrow_x, 0_y\rangle, |0_x, \uparrow_y\rangle, |\downarrow_x, 0_y\rangle, |0_x, \downarrow_y\rangle\} \tag{158}$$

In this basis, the Hamiltonian rewrite:

$$H^1_{AL} = \begin{pmatrix} 0 & -\lambda & 0 & 0 \\ -\lambda & 0 & 0 & 0 \\ 0 & 0 & 0 & -\lambda \\ 0 & 0 & -\lambda & 0 \end{pmatrix} \tag{159}$$

In case of three electrons, the charge 3 basis is:

$$\mathcal{B}_3 = \{|\uparrow\downarrow_x, \uparrow_y\rangle, |\uparrow\downarrow_x, \downarrow_y\rangle, |\uparrow_x, \uparrow\downarrow_y\rangle, |\downarrow_x, \uparrow\downarrow_y\} \tag{160}$$

The Hamiltonian in this basis is:

$$H^3_{AL} = \begin{pmatrix} U & 0 & -\lambda & 0 \\ 0 & U & 0 & -\lambda \\ -\lambda & 0 & U & 0 \\ 0 & -\lambda & 0 & U \end{pmatrix} \tag{161}$$

In the charge 1 channel the eigenvalues of H^1_{AL} are doubly degenerate (because of the spin) and given by :

$$e^1_{pm} = \pm\lambda \tag{162}$$

In the charge 3 channel, the eigenvalues are still doubly degenerate because of the spin (there is always one pair, and a possible degeneracy of spin of the unpaired electron) and are given by:

$$e^3_\pm = U \pm \lambda \tag{163}$$

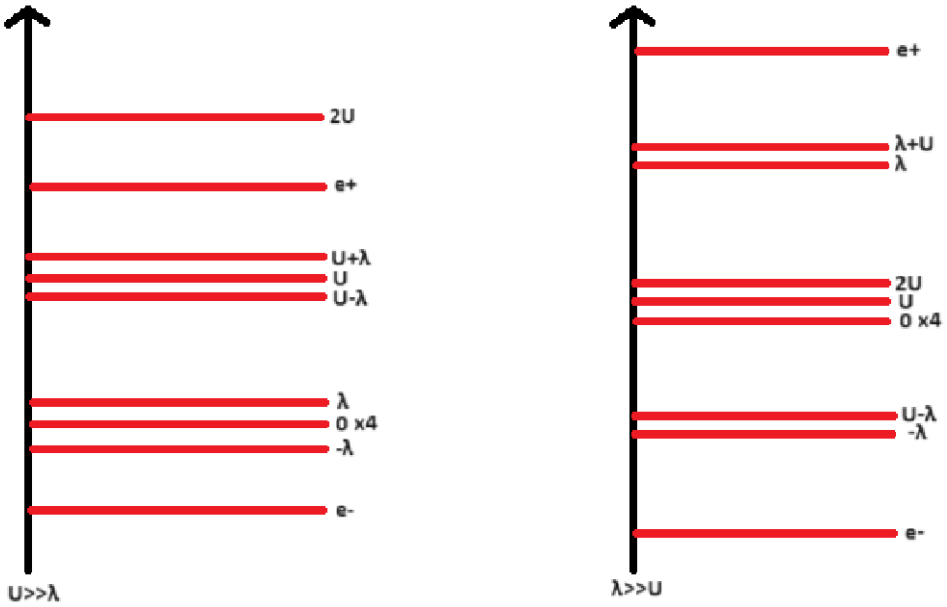

Figure 30: Schematic of the spectrum of the system in the atomic limit. The 0 energy level is three fold degenerate. The states are depicted for $U \gg \lambda$ (right) and $\lambda \gg U$ (left).

Both the charge 1 and charge 3 channels presents two doubly degenerated eigenvalues due to a spin degeneracy. The three electron case is analogous to the 1 electron case, but it is the hole that is doubly degenerated. Let us finally note that the energy of the system is 0 in the charge 0 channel and 2U in the charge 4 channel. Therefore, we can represent the spectrum of this model in Fig. 30

In both limit cases, the ground-state is given by the $e_- = \frac{U-\sqrt{U^2+16\lambda^2}}{2}$ eigenvalue. In the $\mathcal{B}_2$ half-filling basis given in Eq. (158), eigenvector $|-\rangle$ associated to e_- is given by:

$$|-\rangle = \frac{4\lambda}{U+\sqrt{U^2+16\lambda^2}}|\uparrow\downarrow_x, 0_y\rangle + \frac{4\lambda}{U+\sqrt{U^2+16\lambda^2}}|0_y, \uparrow\downarrow_y\rangle + |\uparrow_x, \downarrow_y\rangle + |\uparrow_x, \downarrow_y\rangle \tag{164}$$

Although this eigenvector is non normalized, we see in the $U \gg \lambda$ case the first two components vanishes, and only the singlet states have a weight. This is in agreement with Mott-Insulator physics, pair formation are avoided. If U is large but not infinite, some double occupations are still possible when λ is non zero. We now want to know whether it is possible to have a Mott insulator on only one orbital and a metal on the other orbital away from half-filling.

6.2 . Composite operator treatment and phase diagram

6.2.1 . Extending the theory to two orbitals

We want to study the strongly correlated limit of this hamiltonian in the following regime: $U^x = U^y = U \gg \lambda$, $t_x = t_y = t$. For simplicity we also consider $\mu_x = \mu_y = \mu$. We choose this regime to verify whether spontaneous orbital symmetry breaking can be observed only with this regime. The two orbital Hubbard Hamiltonian is now given by

$$H = -\sum_{ij\alpha\sigma} t_{ij} c^{\dagger}_{i\alpha\sigma} c_{j\alpha\sigma} - \mu \sum_{i\sigma\alpha} n_{i\alpha\sigma} - \lambda \sum_{i\sigma} (c^{\dagger}_{ix\sigma} c_{iy\sigma} + c^{\dagger}_{iy\sigma} c_{ix\sigma}) + U \sum_{i\alpha} n_{i\alpha\uparrow} n_{i\alpha\downarrow} \tag{165}$$

α is the orbital quantum number and can be either x or y. We introduce the following basis which is adapted to this limit because it commutes with the interaction terms:

$$\psi_{i\sigma} = \begin{pmatrix} \xi_{ix\sigma} \\ \eta_{ix\sigma} \\ \xi_{iy\sigma} \\ \eta_{iy\sigma} \end{pmatrix} \tag{166}$$

With:

$$\begin{cases} \xi_{i\alpha\sigma} & = c_{i\alpha\sigma} - c_{i\alpha\sigma} n_{i\alpha\bar{\sigma}} \\ \eta_{i\alpha\sigma} & = c_{i\alpha\sigma} n_{i\alpha\bar{\sigma}} \end{cases} \tag{167}$$

As usual with the method, it is important to notice that $c_{i\alpha\sigma} = \xi_{i\alpha\sigma} + \eta_{i\alpha\sigma}$.

The same equation of motion approach can be performed by introducing the 4×4 composite Green's function matrix defined by:

$$\mathbf{S}_{ij\sigma\sigma'}(\tau) = \langle\langle \psi_{i\sigma}(\tau); \psi^{\dagger}_{j\sigma'} \rangle\rangle = \theta_H(\tau) \langle\{\psi_{i\sigma}(\tau); \psi^{\dagger}_{j\sigma'}\}\rangle \tag{168}$$

From now on we will assume a paramagnetic solution, therefore we will take $\sigma' = \sigma$. The connection between **S** matrix and the electronic Green's function G appears from the relation $c_{i\alpha\sigma} = \xi_{i\alpha\sigma} + \eta_{i\alpha\sigma}$, and is now involving different matrix element depending on the considered orbital:

$$\begin{cases} G_{ijxx\sigma}(\tau) & = S^{11}_{ij\sigma} + S^{12}_{ij\sigma} + S^{21}_{ij\sigma} + S^{22}_{ij\sigma} \\ G_{ijyy\sigma}(\tau) & = S^{33}_{ij\sigma} + S^{34}_{ij\sigma} + S^{43}_{ij\sigma} + S^{44}_{ij\sigma} \\ G_{ijxy\sigma}(\tau) & = S^{13}_{ij\sigma} + S^{14}_{ij\sigma} + S^{23}_{ij\sigma} + S^{24}_{ij\sigma} \end{cases} \tag{169}$$

$G_{ijxx\sigma}$ and $G_{ijyy\sigma}$ are the usual electronic Green's function for their respective orbitals, while $G_{ijxy\sigma}$ is an inter-orbital electronic Green's function and will be useful for studying hybridization.

We perform the same equation of motion scheme and apply the usual composite operator approximation (Eq. 173) to obtain the usual relation between the **M** and **I** matrices:

$$\mathbf{M}_{ij\sigma} \approx \sum_{l} \mathbf{E}_{il\sigma} \mathbf{I}_{lj\sigma} \tag{170}$$

Where

$$\begin{aligned} \mathbf{I}_{ij\sigma} &= \langle\{\psi_{i\sigma}; \psi^{\dagger}_{j\sigma}\}\rangle \\ \mathbf{M}_{ij\sigma}(\tau) &= \langle\{J_{i\sigma}(\tau); \psi^{\dagger}_{j\sigma}\}\rangle \end{aligned} \tag{171}$$

$J_{i\sigma}(\tau)$ is the total current defined by:

$$J_{i\sigma}(\tau) = \partial_\tau \psi_{i\sigma}(\tau) = [\psi_{i\sigma}(\tau), H] \tag{172}$$

Under the main approximation of the composite operators method it simplify to:

$$J_{i\sigma}(\tau) \approx \sum_l \mathbf{E}_{il} \psi_l(\tau) \tag{173}$$

Finally, with the main hypothesis and translational invariance, we obtain in Fourier space the following equation of motion for the composite Green's function:

$$\mathbf{S}_{ij\sigma} = \sum_l [\omega \mathbf{Id}_4 - \mathbf{E}]^{-1}_{il} \mathbf{I}_{lj\sigma} \tag{174}$$

The presence of the λ and t terms constrain us to neglect terms in the total current which are non proportional to ψ. However, the currents are exactly proportional to the composite operators in the atomic limit. As such, the Hubbard operators provides a good description of the Mott insulator phase and are appropriate to study excitations around half-filling. Therefore the current truncation is assumed to be a good hypothesis in the vicinity of the Mott phase.

The self-consistent loop then remain the same as depicted on Fig. 11: using fluctuation-dissipation theorem an equation between the correlation functions $\mathbf{C}_{ij\sigma} = \langle \psi_{i\sigma} \psi^\dagger_{j\sigma} \rangle$ and the eigenvalues of the $\mathbf{E}$ matrix can be obtained, and the self-consistency loop is closed by expressing the elements of the E matrix as a function of these $\mathbf{C_{ij\sigma}}$. From the results of our analysis of Roth and Pauli solutions in Sec. 5, we will only consider Roth solution in this section as we showed it is more physical.

We thus explicitly compute the $\mathbf{I}$ and $\mathbf{M}$ matrix (which allows to obtain $\mathbf{E}$). We start with the $\mathbf{I}$ matrix:

$$\mathbf{I}_{ij\sigma} = \langle \{\psi_{i\sigma}, \psi^\dagger_{j\sigma}\} \rangle = \delta_{ij} \begin{pmatrix} 1 - \frac{n_{ix}}{2} & 0 & 0 & 0 \\ 0 & \frac{n_{ix}}{2} & 0 & 0 \\ 0 & 0 & 1 - \frac{n_{iy}}{2} & 0 \\ 0 & 0 & 0 & \frac{n_{iy}}{2} \end{pmatrix} \tag{175}$$

To compute the **M** matrix we need first to explicitly compute the currents. From now on we will assume $\sigma = \uparrow$ and we will not write σ anymore. Note that the equations will be the same if $\sigma = \downarrow$.

$$\begin{aligned} j^1_i &= -\mu^x \xi_{ix\uparrow} - \sum_j t^x_{ij}(c_{jx\uparrow} + \Pi_{ijx}) - \lambda(c_{iy\uparrow} + \Gamma_{ixy}) \\ j^2_i &= -(\mu^x - U^x)\eta_{ix\uparrow} + \sum_j t^x_{ij}\Pi_{ijx} + \lambda\Gamma_{ixy} \\ j^3_i &= -\mu^y \xi_{iy\uparrow} - \sum_j t^y_{ij}(c_{jy\uparrow} + \Pi_{ijy}) - \lambda(c_{ix\uparrow} + \Gamma_{iyx}) \\ j^4_i &= -(\mu^y - U^y)\eta_{iy\uparrow} + \sum_j t^y_{ij}\Pi_{ijy} + \lambda\Gamma_{iyx} \end{aligned} \tag{176}$$

With:

$$\begin{aligned}\Pi_{ij\alpha} &= -n_{i\alpha\downarrow}c_{j\alpha\uparrow} + S^-_{i\alpha}c_{j\alpha\downarrow} - \Delta_{i\alpha}c^\dagger_{j\alpha\downarrow}\\ \Gamma_{i\alpha\alpha'} &= -n_{i\alpha\downarrow}c_{i\alpha'\uparrow} + S^-_{i\alpha}c_{i\alpha'\downarrow} - \Delta_{i\alpha}c^\dagger_{i\alpha'\downarrow}\\ \Delta_{i\alpha} &= c_{i\alpha\uparrow}c_{i\alpha\downarrow} \quad S^-_{i\alpha} = c^\dagger_{i\alpha\downarrow}c_{i\alpha\uparrow}\end{aligned} \tag{177}$$

Finally, the explicit expression of the **M** matrix is:

$$\mathbf{M}_{ij} = \begin{pmatrix} m^{11}_{ijx} & m^{12}_{ijx} & m^{13}_{ij} & m^{14}_{ij} \\ (m^{12}_{ijx})^* & m^{22}_{ijx} & m^{23}_{ij} & m^{24}_{ij} \\ (m^{13}_{ij})^* & (m^{23}_{ij})^* & m^{11}_{ijy} & m^{12}_{ijy} \\ (m^{14}_{ij})^* & (m^{24}_{ij})^* & (m^{12}_{ijy})^* & m^{22}_{ijy} \end{pmatrix} \tag{178}$$

With :

$$\begin{aligned}
m^{11}_{ij\alpha} &= \delta_{ij}\left(-\mu^\alpha(1-\frac{n_{i\alpha}}{2}) - \sum_l t^\alpha_{il}e_{il\alpha} - \lambda e^{\alpha\bar{\alpha}}_{i\alpha}\right) - t^\alpha_{ij}\left(1 - n_{i\alpha} + p_{ij\alpha}\right)\\
m^{12}_{ij\alpha} &= \delta_{ij}\left(\sum_l t^\alpha_{il}e_{il\alpha} + \lambda e^{\alpha\bar{\alpha}}_{i\alpha}\right) - t^\alpha_{ij}\left(\frac{n_{i\alpha}}{2} - p_{ij\alpha}\right)\\
m^{22}_{ij\alpha} &= \delta_{ij}\left(-(\mu^\alpha - U^\alpha)\frac{n_{i\alpha}}{2} - \sum_l t^\alpha_{il}e_{il\alpha} - \lambda e^{\alpha\bar{\alpha}}_{i\alpha}\right) - t^\alpha_{ij}p_{ij\alpha}\\
m^{13}_{ij} &= -\lambda\delta_{ij}\left(1 - \frac{n_{ix}+n_{iy}}{2} + p_{ixy}\right) \qquad m^{23}_{ij} = -\lambda\delta_{ij}\left(\frac{n_{ix}}{2} - p_{ixy}\right)\\
m^{14}_{ij} &= -\lambda\delta_{ij}\left(\frac{n_{iy}}{2} - p_{ixy}\right) \qquad m^{24}_{ij} = -\lambda\delta_{ij}p_{ixy}
\end{aligned} \tag{179}$$

With $\bar{\alpha} = Y$ if $\alpha = X$ and conversely. Hence, since $\mathbf{E} = \mathbf{M}\,\mathbf{I}^{-1}$, we know the **E** matrix will depend on the 9 following parameters to be determined self-consistently:

$$\begin{aligned}
n_{i\alpha} &= \langle c^\dagger_{i\alpha\sigma}c_{i\alpha\sigma}\rangle\\
e_{\alpha\beta} &= \langle \xi_{j\alpha\sigma}\xi^\dagger_{i\beta\sigma}\rangle - \langle \eta_{j\alpha\sigma}\eta^\dagger_{i\beta\sigma}\rangle + \langle \eta_{\beta\sigma}\xi^\dagger_{\alpha\sigma}\rangle - \langle \eta_{\alpha\sigma}\xi^\dagger_{\beta\sigma}\rangle\\
p_{\alpha\beta} &= \langle \hat{n}_{i\alpha\sigma}\hat{n}_{j\beta\sigma}\rangle + \langle S^-_{i\alpha}S^+_{j\beta}\rangle - \langle \Delta_{i\alpha}\Delta^\dagger_{j\beta}\rangle
\end{aligned} \tag{180}$$

We have used translational invariance and C^4 rotational symmetry in order to consider these parameters as site independents constants, the same way as in Sec. 5. Furthermore, since they are physical observable we will assume these parameters are real. We will do likewise for correlation functions. Now we have to express these parameters as a function of the correlation functions to close the system. We define the on site and on bonds 4×4 correlation function matrices as:

$$C^{nm}_0 = C^{nm}_{ii} = cste \qquad C^{nm} = C^{nm}_{ij} = cste \tag{181}$$

We remind that i and j are now always considered as nearest neighbors.

It is easy to express all the one-body parameters as a function of the correlation functions, one simply has to decompose the electronic into composite operators. We get:

$$\begin{aligned} n_x &= 2(1 - C_0^{11} - C_0^{12} - C_0^{21} - C_0^{22}) & n_y &= 2(1 - C_0^{33} - C_0^{34} - C_0^{43} - C_0^{44}) \\ e_x &= C^{11} - C^{22} & e_y &= C^{33} - C^{44} \\ e_{xy} &= C_0^{31} + C_0^{41} - C_0^{23} - C_0^{24} & e_{yx} &= C_0^{13} + C_0^{23} - C_0^{41} - C_0^{42} \end{aligned} \tag{182}$$

For p_x, p_y and p_{xy} we use Roth decoupling as mentioned earlier. The details of the computations of p_x, p_y and p_{xy} can be found in appendix D. The self-consistent equations for p_x and p_y are as follow:

$$\begin{aligned} p_x &= \frac{(n_x)^2}{4} - \frac{\rho_x'}{1-(\phi_x)^2} - \frac{\rho_x'}{1-\phi_x} - \frac{\rho_x}{1+\phi_x} \\ p_y &= \frac{(n_y)^2}{4} - \frac{\rho_y'}{1-(\phi_y)^2} - \frac{\rho_y'}{1-\phi_y} - \frac{\rho_y}{1+\phi_y} \end{aligned} \tag{183}$$

With :

$$\begin{aligned} \rho_x' &= \alpha_x(C^{11} + C^{12})^2 + \beta_x(C^{12} + C^{22})^2 & \rho_y' &= \alpha_y(C^{33} + C^{34})^2 + \beta_y(C^{34} + C^{44})^2 \\ \rho_x &= (\alpha_x + \beta_x)(C^{11} + C^{12})(C^{22} + C^{12}) & \rho_y &= (\alpha_y + \beta_y)(C^{33} + C^{34})(C^{44} + C^{34}) \\ \phi_x &= -\alpha_x(C_0^{11} + C_0^{12}) + \beta_x(C_0^{22} + C_0^{12}) & \phi_y &= -\alpha_y(C_0^{33} + C_0^{34}) + \beta_y(C_0^{44} + C_0^{34}) \end{aligned} \tag{184}$$

And:

$$\alpha_x = \frac{2}{2 - n_x} \qquad \beta_x = \frac{2}{n_x} \qquad \alpha_y = \frac{2}{2 - n_y} \qquad \beta_y = \frac{2}{n_y} \tag{185}$$

Similarly to superconductivity in Sec 5.3.1, several Roth decoupling are possible for p_{xy}. Indeed, a term such as $\Delta_x \Delta_y^*$ can be decouple by considering the x or the y channel (details on this arbitrariness can be found in appendix D). However the two channels must be equal because of translational invariance ($\Delta_x \Delta_y^* = \Delta_y \Delta_x^*$). Therefore, following the original paper or Roth (ref [101]), we will again symmetrize these equations. We then get the following equation:

$$p_{xy} = \frac{1}{2} \sum_{\alpha \in (xy)} \frac{\Omega_0^\alpha - \Omega_{\bar{\alpha}}}{1 - (\phi_\alpha)^2} - \left(\frac{\Omega_\alpha}{1 - \phi_{\bar{\alpha}}} + \frac{\Omega_\alpha'}{1 + \phi_{\bar{\alpha}}} \right) \tag{186}$$

With:

$$\begin{aligned} \Omega_0^x &= \frac{n_y}{2}[\alpha_x(C_0^{11} + C_0^{21}) - 1](-1 + \phi_x) & \Omega_0^y &= \frac{n_x}{2}[\alpha_y(C_0^{33} + C_0^{43}) - 1](-1 + \phi_y) \\ \Omega_x &= \alpha_x(C_0^{31} + C_0^{32})^2 + \beta_x(C_0^{41} + C_0^{42})^2 & \Omega_y &= \alpha_y(C_0^{13} + C_0^{23})^2 + \beta_y(C_0^{14} + C_0^{24})^2 \\ \Omega_x' &= (\alpha_x + \beta_x)(C_0^{31} + C_0^{32})(C_0^{41} + C_0^{42}) & \Omega_y' &= (\alpha_y + \beta_y)(C_0^{13} + C_0^{23})(C_0^{14} + C_0^{24}) \end{aligned} \tag{187}$$

The self-consistency is now closed: starting from initial guess for the 9 parameters defined in Eq. (180), we compute the eigenvalues of the 4×4 **E** matrix. Then, we use fluctuation-dissipation theorem (Eq. 104) to compute the correlation function, that we use to self-consistently obtained new set of parameters.

6.2.2 . Phase diagram

Rather than the n_x and n_y parameters of Eq. (180), we will fix the global electron density $n = n_x + n_y$ (between 0 and 4 due to spin and orbital). The chemical potential μ will be the self-consistent parameter that vary, but is constrained by the following self-consistent equation:

$$n = n_x + n_y = 2(2 - C_0^{11} - C_0^{12} - C_0^{21} - C_0^{22} - C_0^{33} - C_0^{34} - C_0^{43} - C_0^{44}) \tag{188}$$

Then, the electron density on each orbital can be recover by considering the following self-consistent parameter:

$$\delta n = n_x - n_y = 2(C_0^{33} + C_0^{34} + C_0^{43} + C_0^{44} - C_0^{11} - C_0^{12} - C_0^{21} - C_0^{22}) \tag{189}$$

Therefore, instead of fixing n_x and n_y, we fix the total electron density n and the difference of electron density between the orbital δn. If δn converges to zero, the two orbitals have the same density.

The calculation are done on a square lattice of dimension 300×300 with periodic boundary conditions. In Fig 31A we present the phase diagram as a function of total electron density n and inter orbital hopping λ for $U = 20t$ in the hole-doped regime (n smaller than 2). Two solution can be obtained: the orbital uniform phase (OUP) exists everywhere in this phase diagram and is characterized by a vanishing δn and $e_x = e_y$, $p_x = p_y$, $e_{xy} = e_{yx}$. When $\lambda = 0$ this phase is analogous to what was described in Sec. 5.2.1 (with Roth scheme).

For lower values of λ in the vicinity of half-filling, the δn parameter converges to values such that one orbital electron density is close to half-filling, and the other one such that $n = n_x + n_y$. Therefore, we call this phase Orbital Selective Mott Phase (OSMP). We will offer a better characterization of the OSMP in Sec. 6.3. The red line on the phase diagram correspond to the limit beyond which the OSMP cannot be stabilized anymore: the system can then only converge to the OUP. On Fig 31B we plotted the δn parameter for several total electron density n: each line color corresponds to a specific total electron density associated with the colored dashed lines of the phase diagram. For low values of λ and close to half-filling, δn is such that one orbital α is close to half-filling: $n_\alpha = \frac{n \pm \delta n}{2} \approx 1$. This regime thus corresponds to the OSMP. The chosen Mott orbital can be picked randomly, thus δn can converge both with a positive or negative sign. A drop to zero is then observed when entering the OUP phase, where $n_x = n_y$. This drop is therefore associated to the red line of the phase diagram.

On Fig 31C, the energy per site of the two phases are plotted for several total density, again following the same color code as Fig 31B. The dashed line corresponds to the energy per site of the OUP while the continuous one is the OSMP. The energy per site E_s is defined as follow:

$$\langle H \rangle = \sum_i E_s(i) \tag{190}$$

To compute it, we start from the full expression of the 2 orbital Hubbard Hamiltonian at site i:

$$H_i = -\sum_{\delta\alpha\sigma} t^\alpha c^\dagger_{i\alpha\sigma} c_{i+\delta\alpha\sigma} - \sum_{\sigma\alpha} \mu^\alpha n_{i\alpha\sigma} - \lambda \sum_\sigma (c^\dagger_{ix\sigma} c_{iy\sigma} + c^\dagger_{iy\sigma} c_{ix\sigma}) + \sum_\alpha U^\alpha n_{i\alpha\uparrow} n_{i\alpha\downarrow} \tag{191}$$

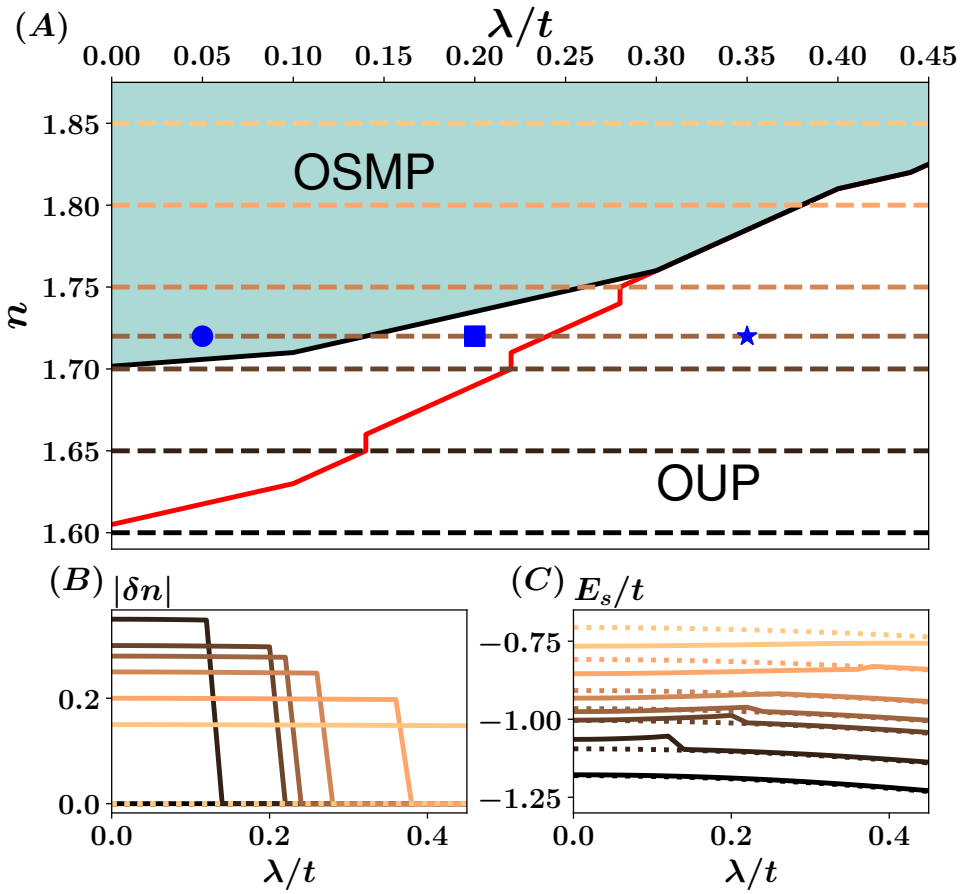

Figure 31: (A): Phase diagram at $U = 20t$, $t = 1$ and $T = 0$ of the system as a function of total electron density n and inter orbital hopping λ in the hole doped regime. The orbital uniform phase (OUP) exists across the whole diagram: it is characterized by a vanishing δn (meaning that $n_x = n_y$), and allows to recover the results from Sec. 5 at $\lambda = 0$. An Orbital Selective Mott Phase (OSMP) emerges for smaller λ and is such that one orbital has a half-filled electron density and the other one is such that the sum of the orbital density gives back n. The red line represents the limit of stability of the OSMP. (B): value of the difference of orbital electron density δn as a function of λ/t for several density associated to the colored lines (A). An abrupt drop to zero can be seen and corresponds to the red line of (A): the OSMP cannot be stabilize anymore. (C) represent the energy per site of the OUP (dashed) and the OSMP (continuous line) as a function of λ/t for electron density associated to the colored lines of (A). The values of (λ, n) such that the OSMP has a lower energy per site is represented by the green area on (A). Between the red and black line, OSMP is metastable.

where δ runs over the nearest neighbours of site i. We now consider the expectation value and re-express each term as a function of the correlation function $C^{nm} = \langle \psi_i^n (\psi_{i+\delta}^m)^\dagger \rangle$ and $C_0^{nm} = \langle \psi_i^n (\psi_i^m)^\dagger \rangle$. For the hoppings terms (weather it is the t or the λ term), we simply use $c_i = \xi_i + \eta_i$ and commutes the operator which are at different sites or orbital to obtain:

$$\begin{cases} \langle H_t \rangle & = \sum_{\delta\sigma} \left(t^x (C^{11} + C^{12} + C^{21} + C^{22}) + t^y (C^{33} + C^{34} + C^{43} + C^{44}) \right) \\ \langle H_\lambda \rangle & = \lambda \sum_{\sigma} (C_0^{31} + C_0^{32} + C_0^{41} + C_0^{42} + C_0^{13} + C_0^{23} + C_0^{14} + C_0^{24}) \end{cases} \tag{192}$$

Then, we simplify this expression using the paramagnetic assumption, the C^4 rotationnal invariance and the fact that $C_0^{41} = (C_0^{14})^*$. We obtain:

$$\begin{cases} \langle H_t \rangle & = 2z[t^x (C^{11} + C^{12} + C^{21} + C^{22}) + t^y (C^{33} + C^{34} + C^{43} + C^{44})] \\ \langle H_\lambda \rangle & = 4\lambda (C_0^{13} + C_0^{23} + C_0^{14} + C_0^{24}) \end{cases} \tag{193}$$

Where z is the coordination number, and is 4 for a square lattice. The expectation value of the interacting term can be derived by replacing the c by ξ and η:

$$\langle H_U \rangle = U(\frac{n_x + n_y}{2} - C_0^{21} - C_0^{43} - C_0^{22} - C_0^{44}) \tag{194}$$

Finally the expectation value of the chemical potential is just a shift of energy and should not be consider to compute the ground-state energy. Finally, the expression of the energy per site is:

$$\begin{aligned} E_i = {} & 2z[t^x (C^{11} + C^{12} + C^{21} + C^{22}) + t^y (C^{33} + C^{34} + C^{43} + C^{44})] + 4\lambda (C_0^{13} + C_0^{23} + C_0^{14} + C_0^{24}) \\ & - U(\frac{n_x + n_y}{2} - C_0^{21} - C_0^{43} - C_0^{22} - C_0^{44}) \end{aligned} \tag{195}$$

Fig 31C reveals the energy per site of the OSMP is smaller than the OUP at low λ and closer to half-filling. On the phase diagram of Fig 31A, we report with the black line the area where the OSMP becomes energetically favorable (green area). In the white area between the black and red lines, the OSMP is stabilized for low λ but not favorable compared to the OUP phase: it is in a metastable state. We will now study these two phases more in depth.

6.2.3 . Bands and hybridization

In the context of the two orbital Hubbard model, hybridization corresponds to the tendency of electrons to delocalize between orbitals. This information can be extracted from the orbitally resolved spectral function $A_{\alpha\beta} \propto -Im(G_{\alpha\beta})$ where α and β runs over x and y orbitals and $G_{\alpha\beta}$ denotes one of the four Green's function introduced in Eq. 169. In Fig 32 We display the bands at electron density $n = 1.72$ for three different values of λ corresponding to the blue stars of fig. 32. The color of the bands represent the difference $A_{xx} - A_{yy}$. This is the tendency of the associated (energy, momentum) set to be localized on the x (green) or on the y (blue) orbital. As in Sec. 5, bands corresponds to the eigenvalues of the E matrix and are the poles of the electronic Green's function for both orbitals. Let us note we zoom around the Fermi energy to display the lower Hubbard bands, and we show as an inset the upper Hubbard bands.

Fig 32A and 32B display the OSMP bands for $\lambda = 0.06$ and $\lambda = 0.2$, respectively corresponding to the stable and metastable region of the OSMP. Among the two lower Hubbard bands, one of them

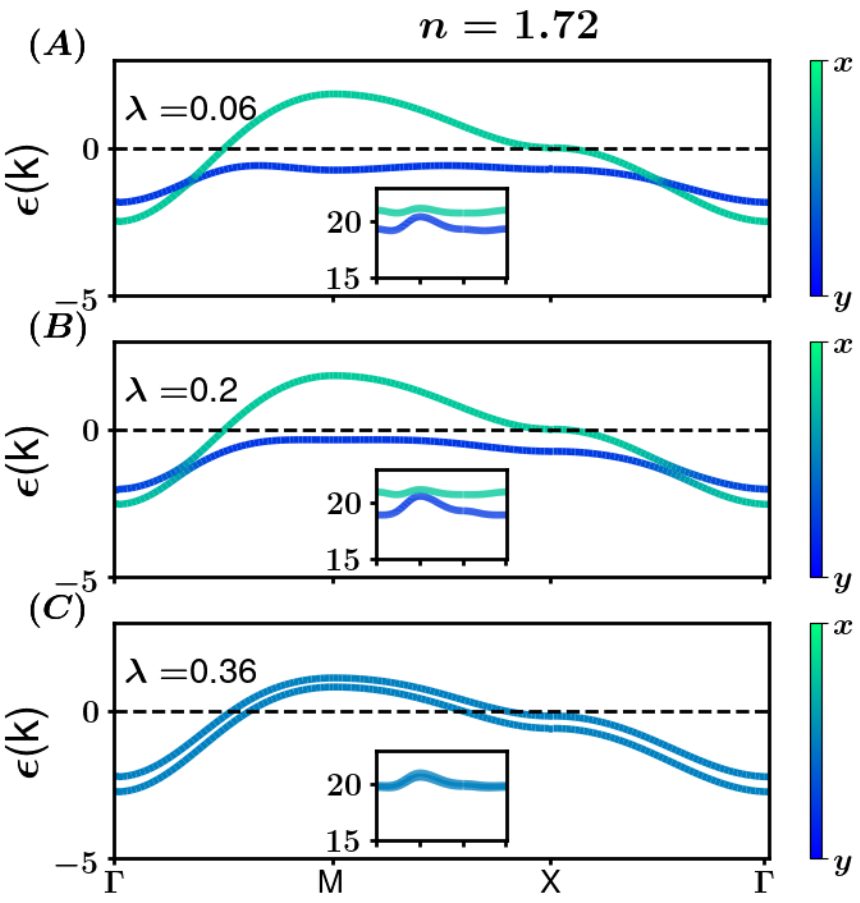

Figure 32: Bands along high symmetry points of the square lattice associated to $n = 1.72$ and $U = 20t$ for three values of λ. (A) and (B) depicts the OSMP respectively in the stable and metastable region while (C) is the OUP. The two bands observed corresponds to the lower Hubbard band splitted in two because of the orbital degree of freedom and λ. The upper Hubbard bands are also splitted in two and represented as an inset for each figure. The colors of the bands depicts the difference $A_{xx} - A_{yy}$. A very blue or green color indicates strong localization on one of the orbital. (A) and (B) presents a fully filled and orbitally localized band, hence it is indeed "Orbital Selective Mott Phase". Hybridization is however not exactly zero and is enhanced with λ around the crossing points of the bands. In (C), $A_x - A_y$ is zero, and the bands are uniformly hybridized, but not degenerated due to the presence of λ.

is fully filled and below the Fermi energy. A clear difference in color appears, meaning that $A_x - A_y$ is very positive for a band and negative for the other one. Thus, in the OSMP bands are mostly associated to an orbital. We can then conclude that the band under the Fermi energy is the Mott band where one of the orbital (here, the y orbital as the Mott band is in blue) electron density is close to

one. It is however important to note that only at exactly $\lambda = 0$, the bands are fully unhybridized. A very small hybridization is observed at the crossing points of the band and gets larger with λ, until it breaks completely the OSMP. Expectingly, the electron density of the Mott orbital is driven slightly away (but remain close) to half-filling whenever hybridization increase. OSMP therefore appears as a spontaneous orbital symmetry breaking.

In the OUP displayed on fig. 32C, the hybridization increased so much that the Mott band disappear completely and gets fully hybridized, resulting in $A_x = A_y$ everywhere. At $\lambda = 0$, the two lower Hubbard bands are degenerated and show analogous behavior as in Sec. 5. However the degeneracy is lifted with λ. Beside having the same electron density for both orbital ($\delta n = 0$), the OUP orbital parameters are also equal ($e_x = e_y$, $p_x = p_y$, $e_{xy} = e_{yx}$). For this solution, $A_x - A_y$ are uniformly zero, meaning that the OUP bands are strongly hybridized at all λ.

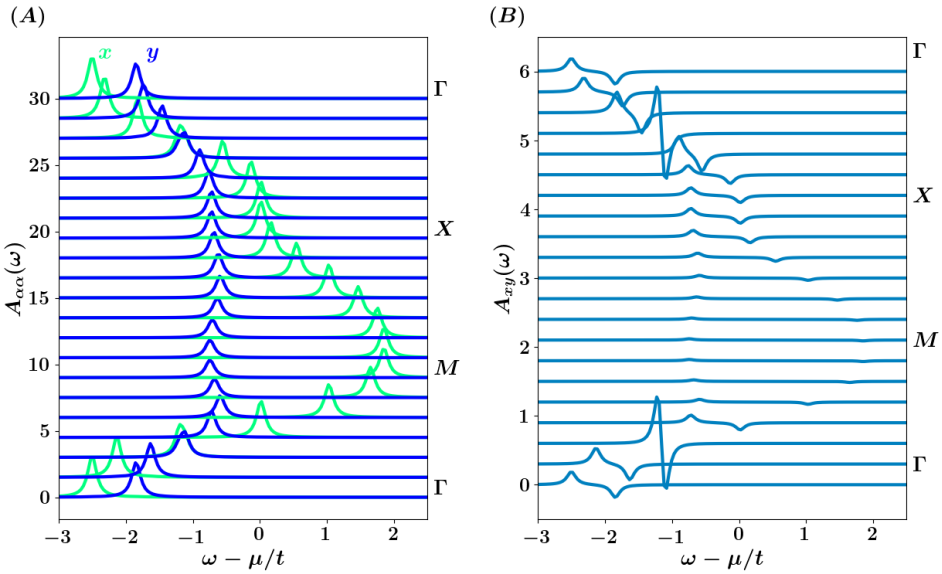

Figure 33: For $\lambda = 0.06t$ $n = 1.72$ (A) displays the intra orbital spectral function $A_{\alpha\alpha}$ as a function of energy $\omega - \mu$ for different high symmetry k-points. The spectral for each k-points are shifted by $1.5t$ for clarity. (B) Shows the inter-orbital spectral function $A_{\alpha\beta}$ for the same parameter. Here the results for each k-points are shifted by $0.3t$ for clarity. The inter-orbital spectral function is non-zero whenever the two intra orbital spectral function overlaps, indicating hybridization.

To confirm this hybridization between the orbitals, we plot in Fig. 33A the spectral function for both the x (green) and y (blue) orbitals as a function of of energy for several high symmetry points in the OSMP at $n = 1.72$ and $\lambda = 0.06t$ (associated to the band of Fig. 32A). Between each momentum points a shift of $1.5t$ has been considered for clarity. On 33B, we plot the inter orbital spectral function for the same parameters of the OSMP. As it takes smaller values, the shift between the k-points is taken equal to $0.3t$.

The spectral function of the two orbitals overlaps for electrons near Γ-X points of the Brillouin zone. The overlaps lead to a substantial interorbital spectral function along the $\Gamma - X$ regions, as

shown in Fig. (33B). However, the spectral functions around $M - X$ points remain well separated and retain their orbital character. Therefore, the interorbital spectral function remains flat around $M - X$ regions.

Therefore, we reveal the characteristics of the bands in the OSMP and OUP phases. First, in the OSMP phase, one of the bands flattens and goes below the Fermi level. Secondly, in the OSMP phase, the two bands have weak hybridization and retain their orbital character. Thirdly, the hybridization occurs only around specific momentum points where the two bands overlap. However, such hybridization remains appreciable for any finite λ, indicating the absence of a complete breakdown of hybridization in the OSMP phase.

Because of this small hybridization no Kondo breakdown is observed. The presence of an interorbital repulsion U_{xy} may have to be considered in order to completely vanish hybridization. This project is left for future studies.

We now shift our attention to the Fermi surface.

6.3 . The orbital selective Mott phase

6.3.1 . Fermi surface

To give a better characterization of the orbital selective Mott phase, and establish an experimental connection with ARPES experiments [83, 84], we represent in Fig. 34 the Fermi surfaces at $n = 1.72$ associated to the three values of λ of Fig. 32.

On the Fermi surface we only represent the Fermi contour, corresponding to the momentum such that the bands have a vanishing energy. While diminushing λ and going from the OUP to the OSMP, an electron pocket centered on (π, π) vanishes. This is in agreement with experimental papers mentioning the loss of spectral weight in the Fermi surface as a characteristic component of Orbital Selective Mott Phase [139]. In our model, this loss of spectral weight at the Fermi energy is explained by the localization of one of the orbital, corresponding to the lower Hubbard band of Fig. 32 that gets completely under the Fermi energy.

Fig. 34A and Fig. 34B are fairly similar. This is because they both corresponds to the OSMP at different λ. Modifying the electron density have a direct effect on the Fermi surface, as observed in the section were the violation of Luttinger theorem has been established (Sec. 5.2.2). To establish the effect of λ, we report on Fig. 34D the evolution of the area enclosed by the Fermi surface as a function of λ for several electron density, with the same color code as in Fig. 31. This area remains almost constant with λ, explaining the similarities between the two figures. However, a big jump in the Fermi surface area occurs when the system undergoes the transition to the OUP phase.

While this increase of the Fermi area can be explained by the second electron pockets being restored, we would like to offer an analogy at this stage with Kondo lattice model. It is first important to note this model is different from Kondo, as strong interaction and hopping are present on both orbitals. That being said, as detailed in Sec. 4.3 Kondo lattice model has the notable effect of enlarging the Fermi surface whenever hybridization occurs as explained in Sec. 4.3.2. The situation is comparable here, as the fermi surface area is enlarged when the transition occurs between the almost non hybridized OSMP and the hybridized OUP. We could also compare the fact that OSMP survive to non zero λ with the competition between antiferromagnetism and hybridization of the Kondo-Heisenberd model as explained in Sec. 4.3.3. This last comparison must be understood cautiously,

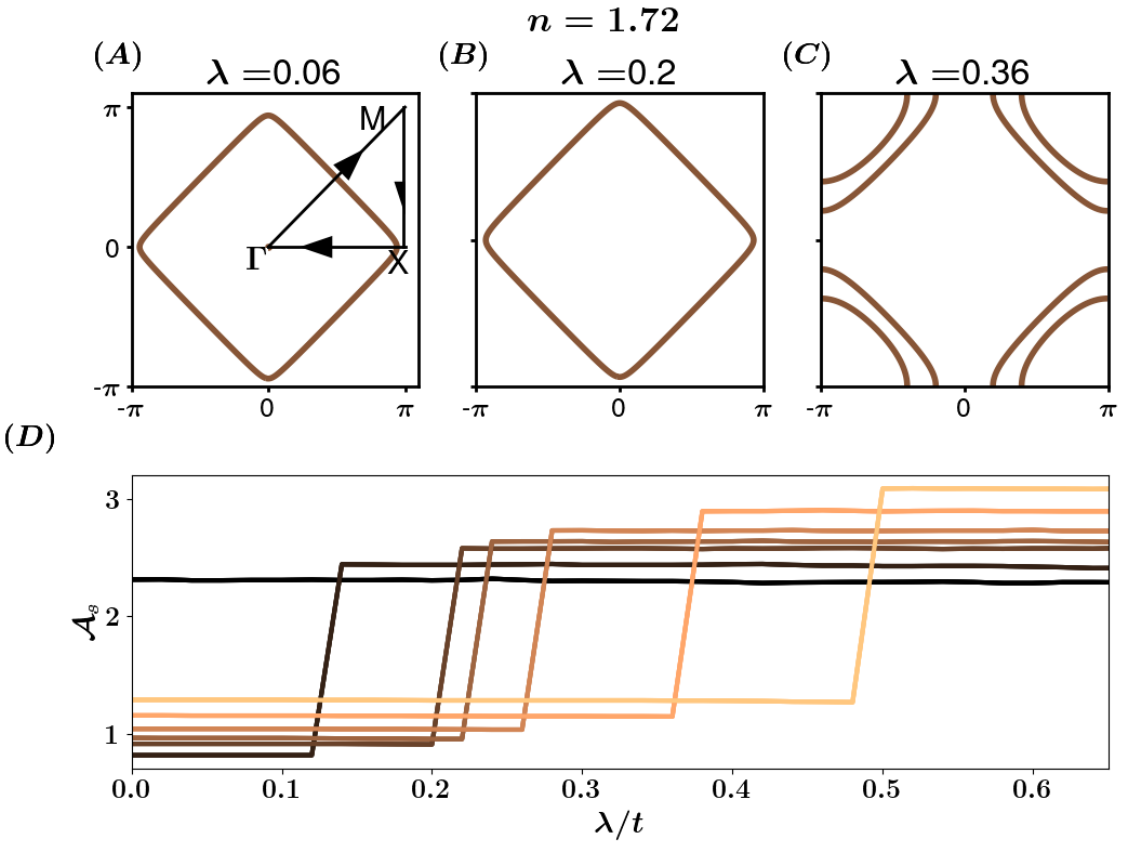

Figure 34: (A) Displays the spectral function $A(\mathbf{k}, \epsilon_F)$ at $\lambda = 0.06t$ in the OSMP phase for $n = 1.72$. (B) Depicts the same for $\lambda = 0.2t$, in the metastable region of the OSMP. (C) Fermi surface of the orbital uniform phase at $\lambda = 0.36t$. In the OSMP, only a single Fermi sheet is observable, whereas in the metallic phase, two sheets are visible. Furthermore, the Fermi surface area is smaller in the OSMP phase compared to the OUP. (D) Illustrates the evolution of the Fermi volume $\mathcal{A}_s$ as a function of inter-orbital hopping for different electron densities, showing a jump at the transition. In the OSMP phase, the Mott orbital does not contribute to the Fermi volume since one band remains filled.

as a paramagnetic assumption has been done in the beginning of the composite operator treatment. Nevertheless, it appears two energy scales are competing in our system, one that would favor Mottness and the other one favoring hybridization. This might explain why OSMP can "resist" to non-zero λ, in contrast to other studies [140].

6.3.2 . Density of states

We shift our attention to the total density of states at n=1.72 as a function of λ on fig. 35A. The lowest line corresponds to $\lambda = 0$ while the uppermost is $\lambda = 0.42t$, and a step of $\delta\lambda = 0.02t$ is taken between each density of states line, separated with an energy shift of $0.05t$ for clarity. The green dashed line corresponding to o energy represent the Fermi energy. The system is in the OSMP until it reaches the critical value of λ after which the phase cannot be stabilized anymore (red line of the

phase diagram of Fig. 31). Above this value $\lambda_c = 0.22t$ the system is in the OUP phase.

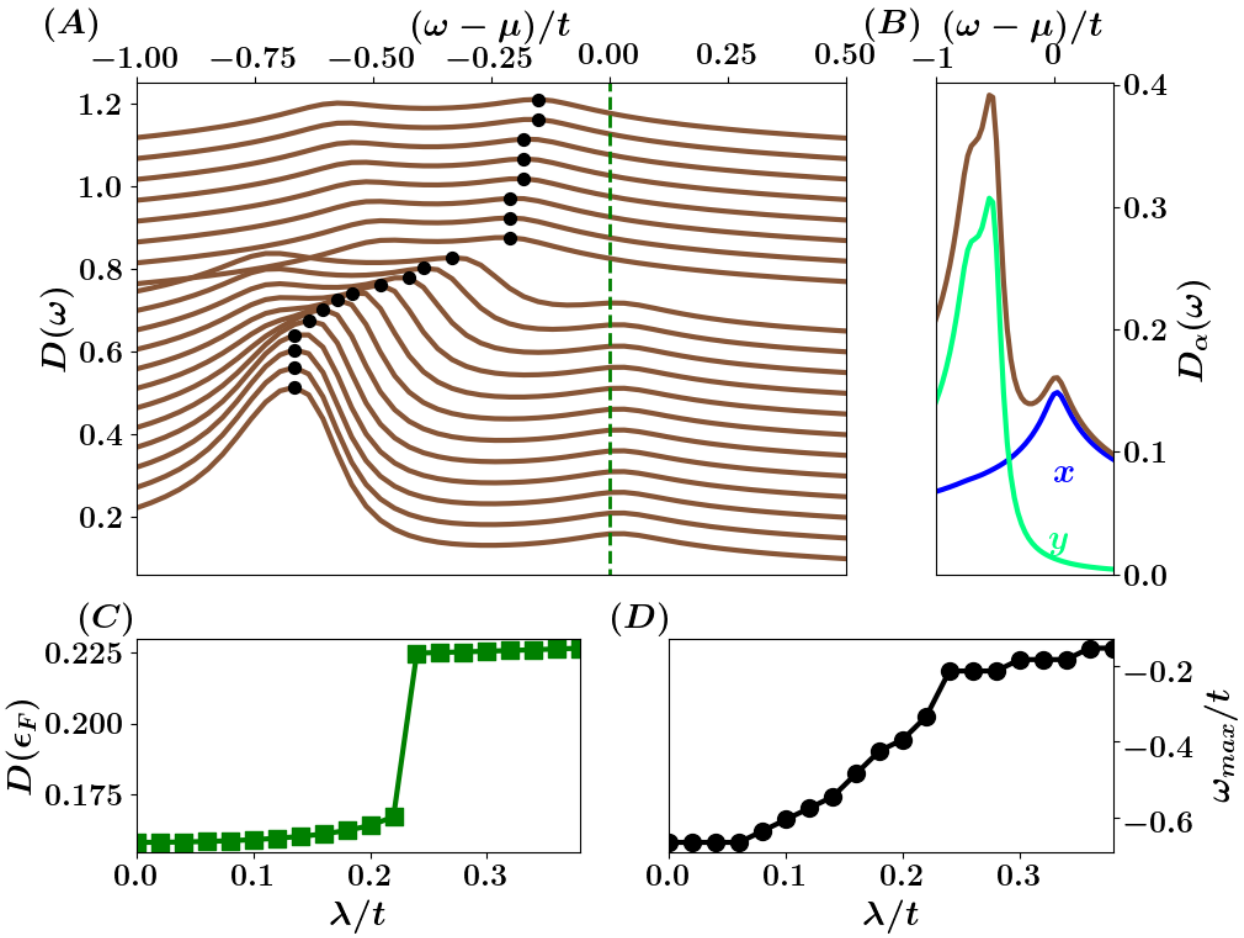

Figure 35: (A) Density of states at $n = 1.72$ and $U = 20t$ for λ ranging from o to $0.42t$ with a step of $0.02t$. A shift of energy of $0.05t$ is made between each λ value for clarity. A Mott peak is observed at low λ and gets flatter as λ is increased. (B) Orbitally resolved Density of states at $\lambda = 0.16t$. This Mott peak is the consequence of one orbital, which is in consistent with the OSMP being almost unhybridized, as detailed in Sec. 6.2.3. (C) Display of the density of states at the Fermi energy. A jump is noticeable at the phase transition because the Mott orbital becomes metallic. Within the OSMP, λ increase the density at the Fermi energy as it creates small hybridization, and push away from half-filling one of the two orbitals. (D) The position of the maximum of the density as a function of λ. As λ increase, hybridization gets stronger and the peak gets closer to half-filling.

At low λ value in the OSMP, a peak below the Fermi energy is noticeable. It is associated to the filled bands depicted in Sec. 6.2.3. Following the conclusion of Sec. 6.3.1 that system in this phase is almost unhybridized, we display on Fig. 35B the orbitally resolved density of states corresponding to $\lambda = 0.16t$. The total density of states is represented in brown while in blue and green are respectively the y and x orbital density of states. The observed peak is indeed the consequence of only one of the

two orbital, corresponding to the filled eigenvalue of the OSMP bands. However, at the Fermi energy, this orbital still has a small but non-zero density of states.

32C tracks the density of states at the Fermi energy. While a clear jump is observed at the OSMP-OUP transition due to the Mott orbital becoming metallic, an increasement of $D(\epsilon_F)$ is observed with λ within the OSMP. This is in agreement with the small hybridization observed around the crossing point of bands in the OSMP in Fig. 32. As showed in previous section, in the OSMP, only at $\lambda = 0$ one of the two eigenvalues is perfectly at half-filling and unhybridized. When λ gets non-zero, a small hybridization is noticeable. As a consequence, the "Mott" orbital is not exactly at half-filling anymore and some states appear at the Fermi energy. Inter orbital hopping compete against the OSMP and progressively hybridized the orbitals and enhance the density of states at the Fermi energy. Once λ gets big enough this hybridization fully destroys the OSMP and the two bands become perfectly hybridized. As a consequence, the density at the Fermi energy presents an important jump.

The density of states gets flatter with increasing λ until no "Mott" peak is distinguishable. Fig. 32D tracks the position of this peak with λ. While a noticeable jump also appears at the phase transition, we observe a shift of the peak to the Fermi energy as it get flatter.

6.3.3 . quasiparticle weight and behavior with Coulomb repulsion

Although composite operator theory is a non-Fermi liquid theory due to its apparent violation of Luttinger theorem (cf Sec. 5.2.2), the quasi-particle weight can still be introduced as the overlap between bare electrons and the quasi-particles of this theory. Indeed, the expression of the electronic Green's function in the composite operator framework is given by

$$G_{\alpha\beta} = \sum_{n\gamma\nu} \frac{\sigma^n_{\gamma\nu}}{\omega - \epsilon^n_k + i0^+} \tag{196}$$

Where n runs over the four eigenvalues of the E matrix ϵ^n and σ^n are the spectral weight matrix defined by Eq. 102. The indices γ and ν are chosen accordingly to rebuild G_{xx}, G_{yy} or G_{xy} and are the matrix elements in the ψ basis of σ (for instance, for G_{xx} γ and ν runs from 1 to 2).

In general, close to the Fermi surface and at small energies, a Green function can be written [12] as:

$$G = \frac{Z}{\omega - \tilde{E}_k + \frac{i}{2\tau(k,\omega)}} \tag{197}$$

$\tau(k,\omega)$ is the quasiparticle lifetime, and diverges as $\omega \to 0$ for a Fermi liquid. As we consider only real Green's function, we do not have this term. Z is the quasiparticle weight. By comparing Eq. 196 and Eq. 197, we get:

$$G_{\alpha\beta} = \sum_{n=1}^{4} \frac{Z^n_{\alpha\beta}}{\omega + \epsilon^n_k + i0^+} \quad \text{with} \quad Z_{\alpha\beta} = \sum_{\gamma\nu} \sigma^n_{\gamma\nu} \tag{198}$$

On figure 36A we report the value of the total quasi-particle weight $Z = \sum_n Z^n_{xx} + Z^n_{yy}$ as a function of λ for several electron density n. An average over the Fermi surface has been done, and the

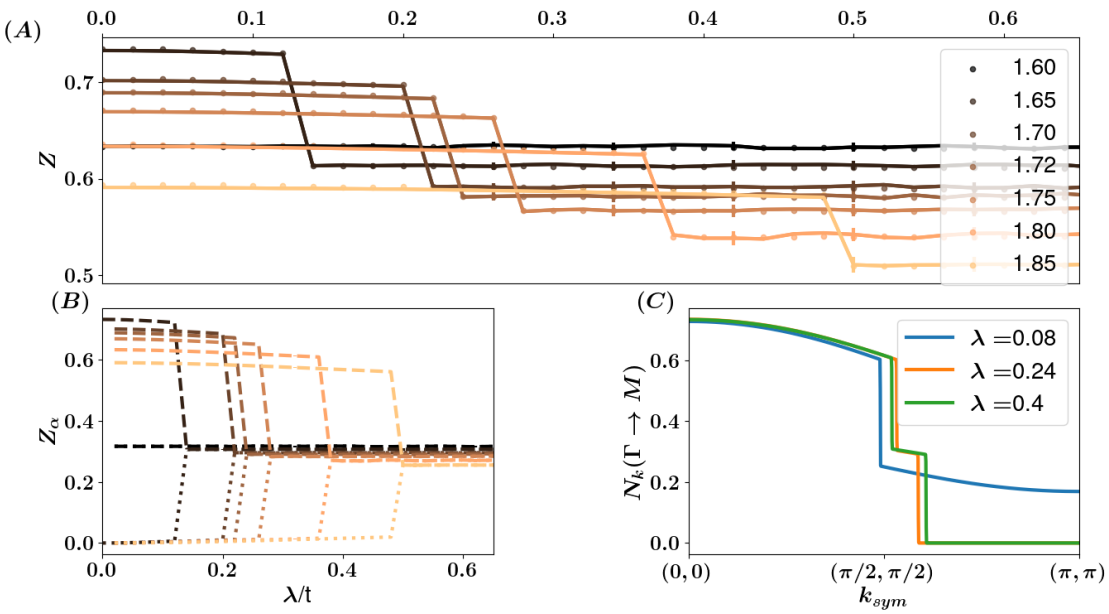

Figure 36: (A): Quasi-particle weigh Z as a function of λ for several electron density n (given in legend). The continuous line correspond to the explicit computation of Z using the Green's function while the dots are obtained by measuring the discontinuity in the momentum resolved electron density N_k. (C): an example of the orbital resolved momentum density in the Γ to M high symmetry line. Two jumps are seen in the OUP because of the presence of two Fermi contour. In the OSMP, only one jump occurs, but N_k is non zero at M due to the filled Mott orbital. (B) The orbital resolved quasi-particle weight. In the OSMP, one of the two orbital has a vanishing weight due to the strong localization of the electrons of the Mott orbital.

displayed errorbar corresponds to the standard deviation. As Z is never close to one, the quasiparticles of the theory are different from the bare electron. Eq. 198 indeed indicates the bare electrons have been fractionalized into four quasi-particles associated to the bands. As a consequence, none of these overlap can be close to one since these quasi-particles have different features than the bare electrons.

We also report the typical shape of N_k along the Γ to M high symmetry line in fig. 36C. By definition of the Green's function in Eq. 197, when crossing the Fermi contour a discontinuity of the order of Z is observed in momentum space. One drop is observed for the OSMP, and the momentum resolved density does not vanish at M due to the fully filled Mott bands. Two drops are seen in the OUP due to the two Fermi contour of the phase. In this case, Z is defined as the sum of these two drops. We report the Z measured this way as a function of λ on Fig 36A as dots. There is a good agreement between the two ways of computing Z

Since there is no Fermi surface at half-filling, and that Z is a quantity defined at the Fermi energy, $Z = 0$ at half-filling. As electron density n is decreasing, Z increases. Therefore, we can also interpret the quasi-particle weight as a measurement of how close the system is from Mott regime.

36B displays the orbitally resolved Quasi-particle weight. In the OSMP the Mott orbital has an almost (exactly at $\lambda = 0$) vanishing quasi-particle weight due to the almost localized nature of the electron. Since the other, non-Mott orbital is further away from half-filling than the two orbital in the OUP, its associated weight is higher. An abrupt drop of the total quasi-particle momentum is observed at the transition, meaning that having two orbitals hole doped makes quasi-particles feel in average more the interaction than in the OSMP.

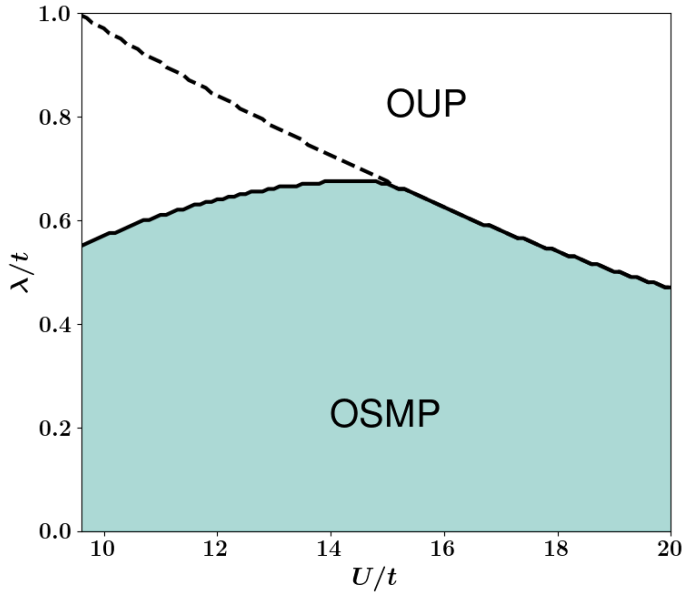

Figure 37: We present the phase diagram as a function of intra-orbital interaction strength U and λ for $n = 1.85$. The colored area shows the region where the OSMP phase is energetically favorable, whereas the OUP phase is favorable in the white region. The OSMP is a metastable state between the thick and dashed lines.

Finally, In Fig. 37, we present the phase diagram when the on-site repulsion U is varied for electron density $n = 1.85$. The colored region indicates where the OSMP phase is more favorable than the uniform phase. On the other hand, the OUP phase is stable in the white areas. The OSMP is a metastable state between the thick and dashed lines.

For lower U, there is a weak increment of critical interorbital hopping λ_c where the OSMP phase becomes unfavorable. For large $U > 15$ the same λ_c reduces with increasing U. Thus, the critical λ_c shows a non-monotonic behavior with Hubbard interaction U.

To qualitatively understand this result, we examine the destabilization of the OSMP phase. Initially, we assume double occupancy is forbidden due to strong repulsion. First, we focus on comprehending the decrease of λ_c with increasing Hubbard interaction.

In the OSMP phase, all the Mott orbital sites are singly occupied, whereas the metallic orbital has itinerant vacancies. When $\lambda \neq 0$, electrons can hop from the Mott to the metallic orbitals if the metallic site is vacant. A stable OSMP phase depends on refilling the holes in the Mott orbital without

significant hybridization. Without recombination, holes will proliferate in the Mott orbital, leading to the breakdown of the orbital differentiation. The hole created in the Mott-orbital is heavy and can be assumed to be approximately immobile.

Two scenarios are possible once an electron hops to the metallic orbital: it either immediately hops back to the Mott orbital or transfers to a neighboring site within the same orbital. The stability of the OSMP phase depends on the ratio between t and λ for a fixed U and electron density.

In the $\lambda \ll t$ regime, electrons are more likely to hop between neighboring sites of the same orbitals rather than between orbitals. Since double occupancy is forbidden, recombination can only happen when any electron on the metallic orbital returns to the site at which Mott orbital has the hole and goes back to the Mott orbital. The mobility of electrons in the metallic orbitals is crucial in such a recombination pathway, which is relatively enhanced for lower U. Thus, the OSMP phase survives for a broader range of λ when U is lower.

In the $\lambda \gg t$ regime, inter-orbital hopping between the x and y orbitals dominates. This leads to strong hybridization between the x and y orbitals, which destroys the OSMP phase.

Finally, we focus on understanding why λ_c decreases for $U < 15$. In this regime, double occupancy contributes to destabilizing the OSMP ordering. As U decreases, double occupancies become more likely, increasing hybridization between the Mott and itinerant orbitals. Consequently, a metastable OSMP phase can still be present at lower U due to the competing processes that are favored when lowering U. However, the OSMP becomes energetically less favorable compared to the orbitally uniform phase.

7 . Conclusion and outlook

The composite operator scheme is a very powerful tool to study strong correlation, that has been forgotten for too long. In this manuscript, we have considered Hubbard operators which are good excitation of the Mott phase, and have performed a detailed analysis of the method in the vicinity of the Mott-region, around half-filling.

In Sec. 5, we brought an answer to the long conflict between the two usually considered [104, 141] set of self-consistent equations: Roth and Pauli scheme. We made a in-depth study of the solution, bands, fermi surface and densities of states. Among the two solutions obtained with Pauli scheme named "COM1" and "COM2", COM1 does not describe a Mott-insulator at half-filling, does not stabilize superconductivity and overall does not seem to take the interaction into account as the bands we obtained are simply the tight-binding dispersion splitted by the interaction. While COM2 is describing a Mott-insulator at half-filling and stabilize superconductivity, its associated Fermi surface displays an unexplained second electron pocket for every doping. The density of states of both Roth and COM2 solution displays the expected transfer of spectral weight from the lower to the upper Hubbard bands. This is also reported by the "waterfall" feature displayed when plotting the spectral weight on the bands: in the hole doped regime, closer to half-filling, pairs are more likely to form and the upper Hubbard bands gains some states. The final argument to discriminate Pauli scheme is detailed on Fig. 20, as it violates Roth decoupling. As the decoupling does not involve any additional approximation than the central composite operator hypothesis on the current (Eq. 87) that we already assume, it has to be satisfied after convergence. We thus claim Roth scheme is the physical solution one should consider.

Further benchmarks of the method have been established by observing a Luttinger violation at every electron density, and extending the method to longer ranged hopping and d-wave superconductivity. Luttinger violation is even more consequent in the neighborhood of half-filling, and we can conclude this region is a non-Fermi liquid phase. We proved the presence of d-wave superconductivity is a direct consequence of the Van Hove singularity in the density of states, as is only observed in its vicinity. Superconductivity creates a particle-hole symmetry of the bands and opens up a gap of the order of the anomalous superconducting order parameter θ around (π, π). Due to the d-wave symmetry factor, a nodal point is also reported: the Fermi surface therefore consists in set of dots, broadened with some lifetime on fig. 21 for clarity. As more states are available, every quantities is increased, including the mean-field superconducting order parameter. Furthermore, the inclusion longer ranged hopping have confirmed this correlation: as the Van Hove singularity is driven away at higher doping, so do the superconducting peak. We also reported that beside breaking particle-hole symmetry, the extension to longer ranged hopping does not help to satisfy better Luttinger theorem.

In Sec. 6, we applied composite operators method to the interesting case study of a two orbital Hubbard model with inter-orbital hopping. A spontaneous orbital symmetry breaking is reported leading to an orbital selective Mott phase, without any inter orbital interaction or Hund term in the model. In the absence of inter orbital hopping, the electronic bands of this phase are exactly unhybridized, leading to one of the two bands completely filled and below the Fermi energy. The orbital associated to the filled band is then at half-filling and insulating because of Mott physics. As the inter orbital hopping increases, hybridization progressively occurs at the crossing points of the bands,

driving slightly away the Mott orbital from half-filling case. Past a critical value, the two bands get fully hybridized as the system enter an orbital uniform phase. A phase diagram as a function of the inter-orbital hopping and total electron density is displayed on Fig. 31.

If one consider the Fermi energy, this localization of an orbital in the orbital selective Mott phase leads to a charactistic loss of spectral weight reported by ARPES experiments [84]. Analogously to Kondo physics, as hybridization is increased, an increasing of the Fermi surface area is seen in the orbital uniform phase. An orbitally resolved density of states picture also support the strong localization of the selective Mott phase with a peak below the Fermi energy getting progressively flatter and indistinguishable as hybridization is increased by tuning the inter orbital hopping. We finally confirm once again this localization of an orbital by observing a vanishing of one of the orbitally resolved quasi-particle weight in the selective Mott phase. The effect of Coulomb interaction is also studied, as a phase diagram as a function of the interaction and the inter orbital hopping is diplayed on Fig. 37. A maximum of the stability of the orbital selective Mott phase is found in the phase diagram, as the resulting competitions of hopping processes and energy penalty of pairs formations.

Let us provide some final few mentions of the still unexplored potential of this method. This manuscript only considered translational and rotational invariance to perform the self-consistent loop in momentum space. An extension to a fully real space treatment with a finite size lattice is under development and will be the object of further studies. This real space composite operator method might bring to light translational breaking order such as charge density wave or topological effect.

8 . Other works

In this final section, we give a summary of the main results of the other studies performed during this PhD as a co-author. As we deemed them difficult to connect with the composite operator method, which was the main focus of this thesis, it was decided to only synthetically explain the projects as well as my personal contribution in each of these articles.

A serie of three articles was made on superconductivity in monolayer and few layers graphene. The goal of this project was to study and categorize the various superconducting symmetry in these materials. To this end, the first article focused on the computation of the different superconducting symmetry channels. We characterized the momentum resolved lowest energy bands for the various channels as well as the density of states. The study is then repeated to bilayer ABA and ABC stacking. Among all the symmetries considered, two different profiles are distinguished. The fully gapped states displays a U-shaped density of states and includes $s-$, $f-$, $d+id'-$ and $p+ip'-$ wave states while the nodal states such as $d_{xy}-$, $d_{x^2-y^2}-$, p_x- ans p_y- wave states present a V-shaped density of states. In the case of few-layers graphene, the low energy bands is modified by the presence of interlayer coupling changes the profile compare to the monolayer case of only nodal states. In this case, all the nodal points presents a small splitting in momentum space which is not observed in the monolayer study. My personal contribution in this first article was mainly the computation of the form factor, the generation the band structures figures for monolayer graphene, as well as helping in the redaction of the article.

The second article on graphene then focuses on the Chern number study and the edge states.

Chiral states $d + id'$ and $p + ip'$ are considered as only those break time reversal symmetry and can have a non-zero Chern number as the chemical potential and the superconducting pairing strength are tuned. Using an impurity technique, the edge states are visualized within the gap and related to the value of the Chern number. Edge states are also confirmed to be spin degenerated by observing a Zeeman splitting. More complicated diagram for the value of the Chern number are displayed for the bi- and tri-layer graphene case, but the conclusions are mostly the same, and the value of the Chern number is related to the edge states. As such, this can provide a way of characterizing the superconducting pairing symmetry. As I haven't work on any topological related topic, my personal contribution in the second paper was only limited to computing the form factors, as well as a few equations extracted from the first article.

The final article presents the effect of a scalar or magnetic impurity in both monolayer and few layer graphene. For each of the superconducting symmetries the additional local density of states from the impurity is computed by mean of a T-matrix technique [142]. The presence of such additional density means the impurity is creating states within the gap. In the case of a scalar impurity, no subgap is created for superconducting in both the extended s-wave and on-site channels. For any other symmetry, two spin-degenerated subgaps are observable. In the case of a magnetic impurity, two subgaps are seen in the case of an extended s-wave and the other nodal states while four subgaps states exists for the $d + id'$, f and $p + ip'$ channels. A momentum resolved representation of the local density of states is given by computing quasi-particle interferences and shows a breaking of the six fold symmetry for nodal states and not for the fully gapped states, which is in agreement with bands structure computation from the first paper. The results remain similar for bilayer and trilayer graphene, allowing to keep the same analysis. This article therefore provide ways by characterizing the subgaps caused by impurities to constrain the superconducting symmetry of graphene. My personal contribution to this third article was consequent. Beside the computation, I generated all local density of states plots as well as quasi-particle interference for monolayer graphene, and few cases for bi- and tri- layers graphene. I also contributed in the making of the draft, then in the redaction of captions and appendices.

Another study of a metallic junctions has been performed. In this study an attractive Hubbard model is considered and a charge density wave is artificially stabilized on the left side of the junction, with a non-zero attractive interaction. The right side is kept metallic with no interaction. A proximity effect of charge order is observed as charge modulation persist in the metallic section. When changing the electron density of the right metallic side, the proximity effect survive but in domains caused by phase shifts. Therefore a tunneling of the quasi-particle from the ordered region is observed to the metallic region similarly to what is known with a junction between a superconductor and a normal metal. In this article, my contribution was a full rewriting of the code in parallel of the other author and observing the proximity effect for charge density wave together with collaborator. I mostly rechecked all the results detailed in the article, but did not contribute in the redaction.

References

[1] R. Lifshitz, "What is a crystal?," Zeitschrift für Kristallographie, vol. 222, p. 313–317, June 2007.

[2] Y. A. Izyumov, "Theory of an impurity state in a crystal†," Advances in Physics, vol. 14, pp. 569–619, Oct. 1965.

[3] N. Ashcroft and N. Mermin, Physique des solides. EDP Sciences, 2002.

[4] H. Bruus and K. Flensberg, Many-body quantum theory in condensed matter physics - an introduction. United States: Oxford University Press, 2004.

[5] A. Altland and B. D. Simons, Condensed matter field theory. Cambridge University Press, 2010.

[6] P. K. Misra, "Chapter 1 - basic properties of crystals," in Physics of Condensed Matter (P. K. Misra, ed.), pp. 1–35, Boston: Academic Press, 2012.

[7] D. W. B.-O. (auth.), Crystallography. Springer, 1993.

[8] F. Bloch, "Über die quantenmechanik der elektronen in kristallgittern," Zeitschrift für Physik, vol. 52, pp. 555–600, 1929.

[9] S. H. Simon, The Oxford solid state basics. Oxford, UK: Oxford Univ. Press, 2013.

[10] C. Jacoboni, Bloch States and Band Theory, pp. 69–83. Berlin, Heidelberg: Springer Berlin Heidelberg, 2010.

[11] C. Varma, Z. Nussinov, and W. van Saarloos, "Singular or non-fermi liquids," Physics Reports, vol. 361, no. 5, pp. 267–417, 2002.

[12] E. Pavarini, Dynamical mean-field theory of correlated electrons: Lecture notes of the autumn school on correlated electrons 2022. 2022.

[13] Landau Fermi-Liquid Theory and Low Temperature Properties of Normal Liquid 3He, ch. 1, pp. 1–121. John Wiley and Sons, Ltd, 1991.

[14] J. Spałek, "Liquids, theory of: Fermi liquids," in Reference Module in Materials Science and Materials Engineering, Elsevier, 2016.

[15] K. Yamada, Fermi liquid theory, p. 22–28. Cambridge University Press, 2004.

[16] Y. Kuramoto, Fermi Liquid Theory, pp. 65–74. 02 2020.

[17] S. Sachdev, Quantum Phases of Matter. Cambridge University Press, 2023.

[18] M. Kinza, Theory of Fermi-liquids in Metals: A Compact Overview as an Introduction to Theoretical Solid-State Physics. essentials, Wiesbaden: Springer Fachmedien Wiesbaden, 2021.

[19] J. M. Luttinger, "An Exactly Soluble Model of a Many-Fermion System," Journal of Mathematical Physics, vol. 4, pp. 1154–1162, 09 1963.

[20] P. A. Lee, N. Nagaosa, and X.-G. Wen, "Doping a mott insulator: Physics of high-temperature superconductivity," Rev. Mod. Phys., vol. 78, pp. 17–85, Jan 2006.

[21] F. Gebhard, The Mott Metal-Insulator Transition: Models and Methods. No. 137 in Springer Tracts in Modern Physics, Berlin, Heidelberg: Springer-Verlag Berlin Heidelberg Springer e-books, 1997.

[22] T. D. Stanescu, P. Phillips, and T.-P. Choy, "Theory of the luttinger surface in doped mott insulators," Phys. Rev. B, vol. 75, p. 104503, Mar 2007.

[23] R. M. Martin, L. Reining, and D. M. Ceperley, Derivation of the Luttinger theorem, p. 735–738. Cambridge University Press, 2016.

[24] A. Praz, J. J. Feldman, H. Knoerrer, and E. Trubowitz, "A proof of luttinger's theorem," EPL, vol. 72, pp. 49–54, 2005.

[25] J. M. Luttinger and J. C. Ward, "Ground-state energy of a many-fermion system. ii," Phys. Rev., vol. 118, pp. 1417–1427, Jun 1960.

[26] M. Oshikawa, "Topological approach to luttinger's theorem and the fermi surface of a kondo lattice," Physical Review Letters, vol. 84, p. 3370–3373, Apr. 2000.

[27] D. V. Else, R. Thorngren, and T. Senthil, "Non-fermi liquids as ersatz fermi liquids: General constraints on compressible metals," Physical Review X, vol. 11, Apr. 2021.

[28] O. E. Obakpolor and P. Hosur, "Surface luttinger arcs in weyl semimetals," Phys. Rev. B, vol. 106, p. L081112, Aug 2022.

[29] I. Osborne, T. Paiva, and N. Trivedi, "Broken Luttinger theorem in the two-dimensional Fermi-Hubbard model," Physical Review B, vol. 104, p. 235122, Dec. 2021.

[30] S. Kellar and K.-M. Tam, "Non-fermi liquid behaviour in the three dimensional hubbard model," 2020.

[31] D. M. Edwards, "The breakdown of fermi liquid theory in the hubbard model: Ii," Journal of Physics: Condensed Matter, vol. 5, p. 161, jan 1993.

[32] W.-W. Yang, Q. Chen, H.-G. Luo, and Y. Zhong, "Violation of luttinger's theorem in the simplest doped mott insulator: Falicov-kimball model in the strong-correlation limit," Physical Review B, vol. 106, Nov. 2022.

[33] V. Kozhevnikov, "Meissner effect: History of development and novel aspects," 05 2021.

[34] C. A. Reynolds, B. Serin, and L. B. Nesbitt, "The isotope effect in superconductivity. i. mercury," Phys. Rev., vol. 84, pp. 691–694, Nov 1951.

[35] B. Serin, C. A. Reynolds, and C. Lohman, "The isotope effect in superconductivity. ii. tin and lead," Phys. Rev., vol. 86, pp. 162–164, Apr 1952.

[36] H. Fröhlich, "Isotope effect in superconductivity," Proceedings of the Physical Society. Section A, vol. 63, p. 778, jul 1950.

[37] J. Bardeen, L. N. Cooper, and J. R. Schrieffer, "Theory of Superconductivity," Physical Review, vol. 108, pp. 1175–1204, Dec. 1957.

[38] R. M. Fernandes, "Lecture notes: Bcs theory of superconductivity," 2015.

[39] M. Chernodub, "Can nothing be a superconductor and a superfluid?," Proceedings of Science, 04 2011.

[40] R. A. Dunlap, "Bcs theory," in Electrons in Solids, 2053-2571, pp. 9–1 to 9–11, Morgan and Claypool Publishers, 2019.

[41] M. Franz, "Superconductivity: Importance of fluctuations," Nature Physics, vol. 3, pp. 686–687, 10 2007.

[42] J. G. Bednorz and K. A. Müller, "Possible high T_c superconductivity in the Ba-La-Cu-O system," Zeitschrift fur Physik B Condensed Matter, vol. 64, pp. 189–193, June 1986.

[43] M. R. Norman and C. Pépin, "The electronic nature of high temperature cuprate superconductors," Reports on Progress in Physics, vol. 66, p. 1547, sep 2003.

[44] P. W. Phillips, L. Yeo, and E. W. Huang, "Exact theory for superconductivity in a doped mott insulator," Nature Physics, vol. 16, p. 1175–1180, July 2020.

[45] D. Chowdhury and S. Sachdev, "The enigma of the pseudogap phase of the cuprate superconductors," July 2015.

[46] R. L. Greene, P. R. Mandal, N. R. Poniatowski, and T. Sarkar, "The strange metal state of the electron-doped cuprates," Annual Review of Condensed Matter Physics, vol. 11, p. 213–229, Mar. 2020.

[47] A. Farhoodfar, The Effect of Disorder on Strongly Correlated Electrons. 01 2011.

[48] Y. Maeno, T. M. Rice, and M. Sigrist, "The Intriguing Superconductivity of Strontium Ruthenate," Physics Today, vol. 54, pp. 42–47, 01 2001.

[49] Q. Si, R. Yu, and E. Abrahams, "High-temperature superconductivity in iron pnictides and chalcogenides," Nature Reviews Materials, vol. 1, Mar. 2016.

[50] D. Scalapino, "The case for dx2 – y2 pairing in the cuprate superconductors," Physics Reports, vol. 250, no. 6, pp. 329–365, 1995.

[51] M. Sigrist and K. Ueda, "Phenomenological theory of unconventional superconductivity," Rev. Mod. Phys., vol. 63, pp. 239–311, Apr 1991.

[52] A. Leggett, 283Cuprate superconductivity. Oxford University Press, 09 2006.

[53] J. Hubbard, "Electron correlations in narrow energy bands," Proceedings of the Royal Society of London. Series A. Mathematical and Physical Sciences, vol. 276, pp. 238–257, Nov. 1963.

[54] F. Essler, H. Frahm, F. Göhmann, A. Klümper, and V. Korepin, "The one-dimensional hubbard model," The One-Dimensional Hubbard Model, by Fabian H. L. Essler , Holger Frahm , Frank Göhmann , Andreas Klümper , Vladimir E. Korepin, Cambridge, UK: Cambridge University Press, 2010, 08 2010.

[55] V. Turkowski, One-Band Hubbard Model: DMFT Solution, pp. 75–130. Cham: Springer International Publishing, 2021.

[56] F. Lechermann, Model Hamiltonians and Basic Techniques. 08 2011.

[57] R. Eder, Introduction to the Hubbard model, vol. 7. Physics of Correlated Insulators, Metals, and Superconductors, Modeling and Simulation (Forschungszentrum J¨ulich, J¨ulich, 2017) pp. 6.1–6.29., 2007.

[58] T. Ogawa, K. Kanda, and T. Matsubara, " Gutzwiller Approximation for Antiferromagnetism in Hubbard Model *)," Progress of Theoretical Physics, vol. 53, pp. 614–633, 02 1975.

[59] S. Jiang, D. J. Scalapino, and S. R. White, "Density matrix renormalization group based downfolding of the three-band hubbard model: Importance of density-assisted hopping," Physical Review B, vol. 108, Oct. 2023.

[60] M. Qin, C.-M. Chung, H. Shi, E. Vitali, C. Hubig, U. Schollwöck, S. R. White, and S. Zhang, "Absence of superconductivity in the pure two-dimensional hubbard model," Phys. Rev. X, vol. 10, p. 031016, Jul 2020.

[61] M. Qin, T. Schäfer, S. Andergassen, P. Corboz, and E. Gull, "The hubbard model: A computational perspective," Annual Review of Condensed Matter Physics, vol. 13, p. 275–302, Mar. 2022.

[62] B.-X. Zheng, C.-M. Chung, P. Corboz, G. Ehlers, M.-P. Qin, R. M. Noack, H. Shi, S. R. White, S. Zhang, and G. K.-L. Chan, "Stripe order in the underdoped region of the two-dimensional hubbard model," Science, vol. 358, no. 6367, pp. 1155–1160, 2017.

[63] T. K. Kopec, "Competition between charge ordering and superconductivity in la2–xmxcu04," Physica C: Superconductivity, vol. 153-155, pp. 219–220, 1988.

[64] H.-C. Jiang and S. A. Kivelson, "Stripe order enhanced superconductivity in the hubbard model," Proceedings of the National Academy of Sciences, vol. 119, no. 1, p. e2109406119, 2022.

[65] N. F. MOTT, "Metal-insulator transition," Rev. Mod. Phys., vol. 40, pp. 677–683, Oct 1968.

[66] P. Fazekas, Lecture Notes on Electron Correlation and Magnetism. WORLD SCIENTIFIC, 1999.

[67] P. Cai, W. Ruan, Y. Peng, C. Ye, X. Li, Z. Hao, X. Zhou, D.-H. Lee, and Y. Wang, "Visualizing the evolution from the mott insulator to a charge-ordered insulator in lightly doped cuprates," Nature Physics, vol. 12, p. 1047–1051, Aug. 2016.

[68] J. Katriel and R. Pauncz, Theoretical Interpretation of Hund's Rule, vol. 10 of Advances in Quantum Chemistry. Academic Press, 1977.

[69] J. Solyom, Fundamentals of the Physics of Solids: Volume I Structure and Dynamics. 01 2007.

[70] L. de' Medici, "Hund's metals, explained," 2017.

[71] S. Hoshino and P. Werner, "Spontaneous orbital-selective mott transitions and the jahn-teller metal of A_3c_{60}," Phys. Rev. Lett., vol. 118, p. 177002, Apr 2017.

[72] E. K. Ko, S. Hahn, C. Sohn, S. Lee, S.-S. B. Lee, B. Sohn, J. R. Kim, J. Son, J. Song, Y. Kim, D. Kim, M. Kim, C. H. Kim, C. Kim, and T. W. Noh, "Tuning orbital-selective phase transitions in a two-dimensional hund's correlated system," Nature Communications, vol. 14, June 2023.

[73] J. Sun, Y. Liu, and Y. Song, "Manipulation of hund's rule coupling and orbital-selective mott transition," Acta Physica Sinica, vol. 64, 12 2015.

[74] X.-Z. Qu, D.-W. Qu, W. Li, and G. Su, "Roles of hund's rule and hybridization in the two-orbital model for high-t_c superconductivity in the bilayer nickelate," 2023.

[75] A. Georges and G. Kotliar, "The Hund-metal path to strong electronic correlations," Physics Today, vol. 77, pp. 46–53, 04 2024.

[76] A. Georges, L. d. Medici, and J. Mravlje, "Strong correlations from hund's coupling," Annual Review of Condensed Matter Physics, vol. 4, p. 137–178, Apr. 2013.

[77] P. Werner, E. Gull, and A. J. Millis, "Metal-insulator phase diagram and orbital selectivity in three-orbital models with rotationally invariant hund coupling," Phys. Rev. B, vol. 79, p. 115119, Mar 2009.

[78] L. de'Medici, A. Georges, and S. Biermann, "Orbital-selective mott transition in multiband systems: Slave-spin representation and dynamical mean-field theory," Physical Review B, vol. 72, Nov. 2005.

[79] V. Anisimov, I. Nekrasov, D. Kondakov, T. Rice, and M. Sigrist, "Orbital-selective mott-insulator transition in ca 2 - x sr x ruo 4," The European Physical Journal B - Condensed Matter and Complex Systems, vol. 25, pp. 191–201, 02 2002.

[80] S. Nakatsuji and Y. Maeno, "Quasi-two-dimensional mott transition system $ca_{2-x}sr_xruo_4$," Phys. Rev. Lett., vol. 84, pp. 2666–2669, Mar 2000.

[81] A. Kreisel, B. M. Andersen, P. O. Sprau, A. Kostin, J. C. S. Davis, and P. J. Hirschfeld, "Orbital selective pairing and gap structures of iron-based superconductors," Phys. Rev. B, vol. 95, p. 174504, May 2017.

[82] P. O. Sprau, A. Kostin, A. Kreisel, A. E. Böhmer, V. Taufour, P. C. Canfield, S. Mukherjee, P. J. Hirschfeld, B. M. Andersen, and J. C. S. Davis, "Discovery of orbital-selective cooper pairing in fese," Science, vol. 357, no. 6346, pp. 75–80, 2017.

[83] M. Neupane, P. Richard, Z.-H. Pan, Y.-M. Xu, R. Jin, D. Mandrus, X. Dai, Z. Fang, Z. Wang, and H. Ding, "Observation of a novel orbital selective mott transition in $\mathrm{ca_{1.8}sr_{0.2}ruo_4}$," Phys. Rev. Lett., vol. 103, p. 097001, Aug 2009.

[84] M. Yi, Z.-K. Liu, Y. Zhang, R. Yu, J.-X. Zhu, J. Lee, R. Moore, F. Schmitt, W. Li, S. Riggs, J.-H. Chu, B. Lv, J. Hu, M. Hashimoto, S.-K. Mo, Z. Hussain, Z. Mao, C. Chu, I. Fisher, Q. Si, Z.-X. Shen, and D. Lu, "Observation of universal strong orbital-dependent correlation effects in iron chalcogenides," Nature Communications, vol. 6, July 2015.

[85] A. Dalal and J. Ruhman, "Orbitally selective mott phase in electron-doped twisted transition metal-dichalcogenides: A possible realization of the kondo lattice model," Phys. Rev. Res., vol. 3, p. 043173, Dec 2021.

[86] A. Ramires and J. L. Lado, "Emulating heavy fermions in twisted trilayer graphene," Physical Review Letters, vol. 127, July 2021.

[87] A. Georges, L. d. Medici, and J. Mravlje, "Strong correlations from hund's coupling," Annu. Rev. Condens. Matter Phys., vol. 4, no. 1, pp. 137–178, 2013.

[88] Y. Komijani and G. Kotliar, "Analytical slave-spin mean-field approach to orbital selective mott insulators," Physical Review B, vol. 96, no. 12, p. 125111, 2017.

[89] R. Yu and Q. Si, "Orbital-selective mott phase in multiorbital models for iron pnictides and chalcogenides," Physical Review B, vol. 96, no. 12, p. 125110, 2017.

[90] F. B. Kugler and G. Kotliar, "Is the orbital-selective mott phase stable against interorbital hopping?," Physical review letters, vol. 129, no. 9, p. 096403, 2022.

[91] D. Vollhardt, "Dynamical mean-field theory of strongly correlated electron systems," in Proceedings of the International Conference on Strongly Correlated Electron Systems (SCES2019), Journal of the Physical Society of Japan, Mar. 2020.

[92] A. Georges, G. Kotliar, W. Krauth, and M. J. Rozenberg, "Dynamical mean-field theory of strongly correlated fermion systems and the limit of infinite dimensions," Reviews of Modern Physics, vol. 68, pp. 13–125, Jan. 1996.

[93] M. Kinza and C. Honerkamp, "Single impurity anderson model and dynamical mean field theory : a functional renormalization group study," 2014.

[94] G. Kotliar, S. Savrasov, K. Haule, V. Oudovenko, O. Parcollet, and C. Marianetti, "Electronic structure calculations with dynamical mean-field theory," Reviews of Modern Physics, vol. 78, 08 2006.

[95] H. Park, K. Haule, and G. Kotliar, "Cluster dynamical mean field theory of the mott transition," Physical Review Letters, vol. 101, Oct. 2008.

[96] F. Sun and X. Y. Xu, "Boosting determinant quantum monte carlo with submatrix updates: Unveiling the phase diagram of the 3d hubbard model," 2024.

[97] C. N. Varney, C.-R. Lee, Z. J. Bai, S. Chiesa, M. Jarrell, and R. T. Scalettar, "Quantum monte carlo study of the two-dimensional fermion hubbard model," Phys. Rev. B, vol. 80, p. 075116, Aug 2009.

[98] E. W. Huang, C. B. Mendl, H.-C. Jiang, B. Moritz, and T. P. Devereaux, "Stripe order from the perspective of the hubbard model," npj Quantum Materials, vol. 3, Apr. 2018.

[99] M. Schneider, J. Ostmeyer, K. Jansen, T. Luu, and C. Urbach, "The hubbard model with fermionic tensor networks," in Proceedings of The 38th International Symposium on Lattice Field Theory — PoS(LATTICE2021), LATTICE2021, Sissa Medialab, May 2022.

[100] F. Gebhard and O. Legeza, "Tracing the mott-hubbard transition in one-dimensional hubbard models without umklapp scattering," Physical Review B, vol. 104, Dec. 2021.

[101] L. M. Roth, "Electron Correlation in Narrow Energy Bands. I. The Two-Pole Approximation in a Narrow S Band," Physical Review, vol. 184, pp. 451–459, Aug. 1969.

[102] J. Beenen and D. M. Edwards, "Superconductivity in the two-dimensional Hubbard model," Physical Review B, vol. 52, pp. 13636–13651, Nov. 1995.

[103] F. Mancini and A. Avella, "The Hubbard model within the equations of motion approach," Advances in Physics, vol. 53, pp. 537–768, July 2004.

[104] T. D. Stanescu, I. Martin, and P. Phillips, "d x 2 – y 2 pairing of composite excitations in the two-dimensional Hubbard model," Physical Review B, vol. 62, pp. 4300–4308, Aug. 2000.

[105] E. J. Calegari, S. G. Magalhaes, and A. A. Gomes, "Superconductivity in a two dimensional extended Hubbard model," The European Physical Journal B, vol. 45, pp. 485–496, June 2005. arXiv:cond-mat/0505427.

[106] W. Nolting and W. Borgiel/, "Band magnetism in the hubbard model," Phys. Rev. B, vol. 39, pp. 6962–6978, Apr 1989.

[107] E. Calegari, C. Lobo, S. Magalhaes, C. Chaves, and A. Troper, "Specific heat of a non-local attractive hubbard model," Physics Letters A, vol. 377, p. 1637–1642, Oct. 2013.

[108] A. Avella, F. Mancini, F. P. Mancini, and E. Plekhanov, "Emery vs. hubbard model for cuprate superconductors: a composite operator method study," The European Physical Journal B, vol. 86, pp. 1–19, 2013.

[109] C. Cohen-Tannoudji, B. Diu, and F. Laloë, Mécanique Quantique - Tome 1: Nouvelle édition. EDP Sciences, Nov. 2020.

[110] M. M. Odashima, B. G. Prado, and E. Vernek, "Pedagogical introduction to equilibrium Green's functions: condensed matter examples with numerical implementations," Revista Brasileira de Ensino de Física, vol. 39, Sept. 2016. arXiv:1604.02499 [cond-mat].

[111] E. Fradkin, Field Theories of Condensed Matter Physics. Cambridge University Press, 2 ed., Feb. 2013.

[112] W. P. Lima, F. R. V. Araújo, D. R. Da Costa, S. H. R. Sena, and J. M. Pereira, "Tight-binding Model in First and Second Quantization for Band Structure Calculations," Brazilian Journal of Physics, vol. 52, p. 42, Apr. 2022.

[113] J. A. Sobota, Y. He, and Z.-X. Shen, "Angle-resolved photoemission studies of quantum materials," Rev. Mod. Phys., vol. 93, p. 025006, May 2021.

[114] M. Jarrell, "Hubbard model in infinite dimensions: A quantum monte carlo study," Phys. Rev. Lett., vol. 69, pp. 168–171, Jul 1992.

[115] Y. A. Izyumov, "Hubbard model of strong correlations," Physics-Uspekhi, vol. 38, p. 385, apr 1995.

[116] J. T. Heath and K. S. Bedell, "Necessary and sufficient conditions for the validity of luttinger's theorem," New Journal of Physics, vol. 22, p. 063011, jun 2020.

[117] R. U. Haq and S. S. Bharadwaj, "Schrieffer-wolff transformation of anderson models," 2018.

[118] P. Nozières and A. Blandin, "Kondo effect in real metals," Journal de Physique, vol. 41, no. 3, pp. 193–211, 1980.

[119] O. Zachar, "Staggered liquid phases of the 1d kondo-heisenberg lattice model," Physical Review B - PHYS REV B, vol. 63, 04 2001.

[120] Li, Huan, Song, Hai-Feng, and Liu, Yu, "Phase diagram of the kondo-heisenberg model on honeycomb lattice with geometrical frustration," EPL, vol. 116, no. 3, p. 37005, 2016.

[121] A. Avella and F. Mancini, The Composite Operator Method (COM), p. 103–141. Springer Berlin Heidelberg, Aug. 2011.

[122] A. Avella, F. Mancini, D. Villani, L. Siurakshina, and V. Y. Yushankhai, "The Hubbard Model in the Two-Pole Approximation," International Journal of Modern Physics B, vol. 12, pp. 81–97, Jan. 1998.

[123] A. Avella, F. Mancini, D. Villani, and H. Matsumoto, "The two-dimensional t-t'-U model as a minimal model for cuprate materials," The European Physical Journal B, vol. 20, pp. 303–311, Apr. 2001.

[124] B. Bacq-Labreuil, C. Fawaz, Y. Okazaki, Y. Obata, H. Cercellier, P. Lefevre, F. Bertran, D. Santos-Cottin, H. Yamamoto, I. Yamada, M. Azuma, K. Horiba, H. Kumigashira, M. d'Astuto, S. Biermann, and B. Lenz, "On the cuprates' universal waterfall feature: evidence of a momentum-driven crossover," Dec. 2023. arXiv:2312.14381 [cond-mat].

[125] J. Graf, G.-H. Gweon, K. McElroy, S. Y. Zhou, C. Jozwiak, E. Rotenberg, A. Bill, T. Sasagawa, H. Eisaki, S. Uchida, H. Takagi, D.-H. Lee, and A. Lanzara, "Universal High Energy Anomaly in the Angle-Resolved Photoemission Spectra of High Temperature Superconductors: Possible Evidence of Spinon and Holon Branches," Physical Review Letters, vol. 98, p. 067004, Feb. 2007.

[126] D. Bergeron, D. Chowdhury, M. Punk, S. Sachdev, and A.-M. S. Tremblay, "Breakdown of Fermi liquid behavior at the (\pi,\pi)=2k_f spin-density wave quantum-critical point: the case of electron-doped cuprates," Physical Review B, vol. 86, p. 155123, Oct. 2012. arXiv:1207.1106 [cond-mat].

[127] P. Phillips, T.-P. Choy, and R. G. Leigh, "Breakdown of fermi liquid theory in doped mott insulators by dynamical spectral weight transfer," 2008.

[128] J. M. Luttinger, "Fermi Surface and Some Simple Equilibrium Properties of a System of Interacting Fermions," Physical Review, vol. 119, pp. 1153–1163, Aug. 1960.

[129] J. T. Heath and K. S. Bedell, "Necessary and sufficient conditions for the validity of Luttinger's theorem," New Journal of Physics, vol. 22, p. 063011, June 2020.

[130] I. Dzyaloshinskii, "Some consequences of the Luttinger theorem: The Luttinger surfaces in non-Fermi liquids and Mott insulators," Physical Review B, vol. 68, p. 085113, Aug. 2003.

[131] J. Skolimowski and M. Fabrizio, "Luttinger's theorem in the presence of Luttinger surfaces," Physical Review B, vol. 106, p. 045109, July 2022.

[132] J. G. Bednorz and K. A. Müller, "Perovskite-type oxides—the new approach to high-T_c superconductivity," Rev. Mod. Phys., vol. 60, pp. 585–600, Jul 1988.

[133] M. R. Norman, "Linear response theory and the universal nature of the magnetic excitation spectrum of the cuprates," Physical Review B, vol. 75, p. 184514, May 2007.

[134] L. Taillefer, "Scattering and Pairing in Cuprate Superconductors," Annual Review of Condensed Matter Physics, vol. 1, pp. 51–70, Aug. 2010.

[135] Z. K. Liu, M. Yi, Y. Zhang, J. Hu, R. Yu, J.-X. Zhu, R.-H. He, Y. L. Chen, M. Hashimoto, R. G. Moore, S.-K. Mo, Z. Hussain, Q. Si, Z. Q. Mao, D. H. Lu, and Z.-X. Shen, "Experimental observation of incoherent-coherent crossover and orbital-dependent band renormalization in iron chalcogenide superconductors," Phys. Rev. B, vol. 92, p. 235138, Dec 2015.

[136] R. Yu and Q. Si, "Orbital-selective mott phase in multiorbital models for iron pnictides and chalcogenides," Phys. Rev. B, vol. 96, p. 125110, Sep 2017.

[137] J. Huang, R. Yu, Z. Xu, J.-X. Zhu, J. S. Oh, Q. Jiang, M. Wang, H. Wu, T. Chen, J. D. Denlinger, S.-K. Mo, M. Hashimoto, M. Michiardi, T. M. Pedersen, S. Gorovikov, S. Zhdanovich, A. Damascelli, G. Gu, P. Dai, J.-H. Chu, D. Lu, Q. Si, R. J. Birgeneau, and M. Yi, "Correlation-driven electronic reconstruction in fete1–xsex," Communications Physics, vol. 5, jan 2022.

[138] L. de'Medici, A. Georges, and S. Biermann, "Orbital-selective mott transition in multiband systems: Slave-spin representation and dynamical mean-field theory," Phys. Rev. B, vol. 72, p. 205124, Nov 2005.

[139] J. Huang, R. Yu, Z. Xu, J.-X. Zhu, J. Oh, Q. Jiang, M. Wang, H. Wu, T. Chen, J. Denlinger, S.-K. Mo, M. Hashimoto, M. Michiardi, T. Pedersen, S. Gorovikov, S. Zhdanovich, A. Damascelli, G. Gu, P. Dai, and M. Yi, "Correlation-driven electronic reconstruction in fete1–xsex," Communications Physics, vol. 5, 01 2022.

[140] F. B. Kugler and G. Kotliar, "Is the orbital-selective mott phase stable against interorbital hopping?," Phys. Rev. Lett., vol. 129, p. 096403, Aug 2022.

[141] A. Avella and F. Mancini, "Anomalous Self-Energy Features in the 2D Hubbard Model," Acta Physica Polonica A, vol. 113, pp. 395–398, Jan. 2008.

[142] S. Pinon, V. Kaladzhyan, and C. Bena, "Surface green's functions and boundary modes using impurities: Weyl semimetals and topological insulators," Physical Review B, vol. 101, Mar. 2020.

A . Résumé de la thèse en Français

Cette thèse porte sur l'étude du modèle de Hubbard, considéré comme le modèle le plus simple pour étudier des matériaux où les électrons interagissent fortement entre eux. Les interactions électroniques sont cruciales à comprendre d'un point de vue théorique, car elles sont à l'origine de beaucoup de comportements intriguants parfois encore mal compris, comme la supraconductivité à haute température, les isolants de Mott, les transitions orbitalement sélectives...

Depuis son introduction, le modèle de Hubbard est toujours non résolu exactement dans le cas général, bien qu'il soit analytiquement résolu en une dimension. Ainsi, la plupart des approches modernes sur ce modèle consiste à faire des approximations pour extraire des informations. Parmi la grande quantité de méthodes théoriques utilisées sur ce modèle, nous pouvons citer la DMFT (dynamical mean field theory), la DQMC (determinantal quantum Monte Carlo), ou des approches variationnelles avec les fonctions d'onde de Gutzwiller.

Cette thèse se concentre sur une méthode approximative de résolution du modèle de Hubbard dans le cas où les interactions sont dominantes: les opérateurs composites. Dans ce résumé, nous détaillerons succinctement le principe des opérateurs composites et montrerons quelques résultats obtenus.

Considérons un réseau carré 2D. L'hamiltonien de Hubbard est le suivant:

$$H = -\sum_{ij\sigma} t_{ij}(c^{\dagger}_{i\sigma}c_{j\sigma} + hc) + U\sum_{i} n_{i\uparrow}n_{i\downarrow} - \mu\sum_{i\sigma} n_{i\sigma} \tag{199}$$

Dans cette équation, $c_{i\sigma}$ et $c^{\dagger}_{i\sigma}$ respectivement détruisent ou créent un électron au site i avec un spin σ. $n_{i\sigma} = c^{\dagger}_{i\sigma}c_{i\sigma}$ vaut 1 s'il y a un électron au site i avec un spin σ et zéro autrement. Ainsi le terme en U est une interaction coulombienne qui rend défavorable la présence de deux électrons au même site (et avec des spins opposés à cause du principe de Pauli). Comme U est considéré grand dans ce manuscrit, si une paire d'électrons est formée, le système doit payer une énergie U, ce qui rend ces configurations défavorables (mais pas impossibles). t_{ij} est l'énergie qu'il faut payer pour qu'un électron saute du site i au site j. μ est le potentiel chimique, et fixe le nombre total d'électrons dans le système.

Le principe de la méthode des opérateurs composites se rapproche de l'approximation de Hubbard I. En effet, nous allons introduire les mêmes opérateurs de Hubbard que dans cette approximation:

$$\psi_{i\sigma} = \begin{pmatrix} \xi_{i\sigma} \\ \eta_{i\sigma} \end{pmatrix} \qquad \text{avec} \quad \begin{cases} \xi_{i\sigma} & = c_{i\sigma}(1 - n_{i\bar{\sigma}}) \\ \eta_{i\sigma} & = c_{i\sigma}n_{i\bar{\sigma}} \end{cases} \tag{200}$$

Il est important de noter l'introduction du vecteur ψ: nous dénoterons $\psi^1_{i\sigma} = \xi_{i\sigma}$ sa première composante et $\psi^2_{i\sigma} = \eta_{i\sigma}$ sa deuxième. Ces opérateurs ont la propriété notable d'avoir des courants $J_{i\sigma}$ proportionnels à eux-même dans la limite atomique (où $t_{ij} = 0$. Nous noterons H_{loc} l'hamiltonien résultant). Ainsi:

$$J_{i\sigma} = [\psi_{i\sigma}, H_{loc}] = \mathbf{A}\psi_{i\sigma} \tag{201}$$

Puisque $\psi_{i\sigma}$ est un vecteur, $\mathbf{A}$ est une matrice de proportionnalité et sera notée en gras. Calculer les commutateurs explicitement permet d'obtenir son expression:

$$\mathbf{A} = \begin{pmatrix} \mu & 0 \\ 0 & U-\mu \end{pmatrix} \tag{202}$$

Beaucoup de propriétés importantes du système peuvent être extraites de la fonction de Green electronique $G_{ij\sigma\sigma'}$, définie par:

$$G_{ij\sigma\sigma'}(\tau) = \langle\langle c_{i\sigma}(\tau); c^{\dagger}_{j\sigma'}\rangle\rangle = \theta_H(\tau)\langle\{c_{i\sigma}(\tau); c^{\dagger}_{j\sigma'}\}\rangle \tag{203}$$

Dans cette équation nous avons introduit le temps de Matsubara τ, la fonction de Heaviside $\theta_H(\tau)$ et la notation $\langle\langle .,. \rangle\rangle$, définie par le second terme de l'équation. L'opérateur $\langle . \rangle$ signifie une valeur moyenne thermique, tandis que $\{.,.\}$ représente l'anticommutateur de deux opérateurs.

Afin de déterminer la fonction de Green électronique, la technique des opérateurs composites utilise l'eq. 202 et introduit la matrice des fonctions de Green composites, définie par:

$$\mathbf{S}_{ij\sigma\sigma'} = \langle\langle \psi_{i\sigma}(\tau); \psi^{\dagger}_{j\sigma'}\rangle\rangle \tag{204}$$

L'intérêt principal d'introduire cette matrice réside dans le fait que sommer ses composantes permet de reconstruire la fonction de Green électronique. En effet, il faut remarquer que $\xi_{i\sigma} + \eta_{i\sigma} = c_{i\sigma}$ pour en déduire que:

$$G_{ij\sigma\sigma'} = S^{11}_{ij\sigma\sigma'} + S^{12}_{ij\sigma\sigma'} + S^{21}_{ij\sigma\sigma'} + S^{22}_{ij\sigma\sigma'} \tag{205}$$

Ainsi, déterminer la fonction de Green électronique revient à déterminer la matrice de fonctions de Green composites. En utilisant la propriété des courants des opérateurs de Hubbard (Eq. 202), il est facile de le faire dans la limite atomique ($t_{ij} = 0$). En effet, on peut calculer l'équation du mouvement de cette matrice:

$$\frac{d}{d\tau}\mathbf{S}_{ij\sigma\sigma'} = \delta_{\sigma\sigma'}(\delta(\tau)\langle\{\psi_{i\sigma}(\tau); \psi_{j\sigma}\}\rangle_{loc} + \langle\langle[\psi_{i\sigma}(\tau); H_{loc}]; \psi^{\dagger}_{j\sigma}\rangle\rangle_{loc} \tag{206}$$

$\delta_{\sigma\sigma'}$ a été introduit car nous supposerons dans tout le manuscrit la limite paramagnétique. Il est important de noter que comme nous sommes dans la limite atomiques, les valeurs moyennes thermiques se font dans cette même limite locale, d'où le $\langle ... \rangle_{loc}$. De manière générale, le second terme des équations du mouvement de fonctions de Green est une autre fonction de Green, difficile à calculer puisqu'il faut refaire son équation du mouvement, ce qui donnera encore une fonction de Green inconnue... Cependant, grâce à la propriété des opérateurs de Hubbard dans la limite atomique (Eq. 202), l'équation du mouvement est entièrement soluble. On obtient:

$$\mathbf{S}_{ij\sigma\sigma'} = \delta_{\sigma\sigma'}(\omega - \mathbf{A} + i0^{+})^{-1}\mathbf{I}_{ij\sigma} \tag{207}$$

Où $\mathbf{I}_{ij\sigma}$ est appelée matrice de renormalisation et est définie par:

$$\mathbf{I}_{ij\sigma} = \delta_{ij}\begin{pmatrix} 1-\langle n_{i\sigma}\rangle_{loc} & 0 \\ 0 & \langle n_{i\sigma}\rangle_{loc} \end{pmatrix} \tag{208}$$

Ainsi dans la limite atomique la fonction de Green obtenue est donnée par:

$$G_{ij\sigma\sigma'} = \frac{1 - \langle n_{i\sigma}\rangle_{loc}}{\omega - \mu + i0^+} + \frac{\langle n_{i\sigma}\rangle_{loc}}{\omega - U - \mu + i0^+} \tag{209}$$

Le système est donc exactement soluble dans cette limite. Maintenant, la méthode des opérateurs composites consiste à effectuer une approximation lorsque l'on considère le terme de saut t_{ij}. En effet dans le cas général, les courants $J_{i\sigma} = [\psi_{i\sigma}, H]$ ne sont plus proportionnels à $\psi_{i\sigma}$. Ils peuvent néanmoins être décomposés en une partie proportionnelle, et une partie non-proportionnelle. Ainsi l'approximation principale des opérateurs composites consiste à supposer que les courants des opérateurs de Hubbard demeurent proportionnels à ces opérateurs dans le cas général:

$$J_{i\sigma} \approx \sum_l \mathbf{E}_{il\sigma}\psi_{l\sigma} \tag{210}$$

Deux autres relations peuvent être déduites en conséquence de cette approximation. En effet, en introduisant $\mathbf{M}_{ij\sigma} = \langle\{J_{i\sigma}, \psi_{j\sigma}\}\rangle$, il vient naturellement que:

$$\begin{cases} \mathbf{M}_{ij\sigma} & \approx \sum_l \mathbf{E}_{il\sigma}\mathbf{I}_{lj\sigma} \\ \mathbf{S}_{ij\sigma\sigma'}(\omega) & \approx \delta_{\sigma\sigma'}\sum_l [\omega\mathbf{Id}_2 - \mathbf{E}]^{-1}_{il}\mathbf{I}_{lj\sigma} \end{cases} \tag{211}$$

La première équation vient directement de la définition de M, tandis que la deuxième peut être obtenue en effectuant une transformée de Fourrier temporelle sur l'équation du mouvement de $\mathbf{S}$.

L'intérêt de cette approximation se trouve dans le fait que la matrice $\mathbf{S}$ (et donc la fonction de Green électronique) peut être obtenue en déterminant les matrices $\mathbf{E}$ et $\mathbf{I}$ correctement. Ces dernières peuvent être calculées explicitement, mais dépendront des paramètres suivants:

$$\begin{cases} n_{i\sigma} & = \langle c^\dagger_{i\sigma} c_{i\sigma}\rangle = \frac{n_i}{2} \\ e_{ij} & = \langle \xi_{j\sigma}\xi^\dagger_{i\sigma}\rangle - \langle \eta_{j\sigma}\eta^\dagger_{i\sigma}\rangle \\ p_{ij} & = \langle n_{i\sigma}n_{j\sigma}\rangle + \langle S^-_i S^+_j\rangle - \langle \Delta_i\Delta^*_j\rangle \end{cases} \tag{212}$$

Ainsi, grâce à l'approximation des opérateurs composites, déterminer la fonction de Green électronique dans le cas général revient à fixer correctement ces trois paramètres. Cela peut alors être fait en utilisant le théorème de fluctuation dissipation pour relier les fonctions de corrélations $C_{ij\sigma} = \langle\psi_{i\sigma}\psi^\dagger_{j\sigma}\rangle$ aux valeurs propres de $\mathbf{E}$. On obtient alors l'équation (104). Ensuite, les paramètres ci-dessus peuvent être décomposés en fonction des C_{ij} (Eq. 112) afin d'établir un calcul auto-cohérent de ces paramètres. Le paramètre p est exprimé en fonction des fonctions de corrélations en utilisant le découplage de Roth, détaillé en annexe.

La méthode présente le défaut de posséder après convergence une fonction de corrélation qui devrait valoir zéro à cause du principe de Pauli, mais qui est non nulle. Ainsi, une autre méthode fut suggérée: au lieu d'utiliser le découplage de Roth pour contraindre la valeur de p, on impose cette fonction de corrélation à zéro et on laisse p varier librement de manière auto-cohérente. Ce manuscrit se concentre sur ce long débat dans la littérature de la méthode [122], et arrive à la conclusion que la méthode imposant le principe de Pauli n'est pas physique, puisque le paramètre p varie librement

et n'est pas fixé de manière auto-cohérente. Plus exactement, le découplage de Roth ne suppose aucune approximation supplémentaire que celle déjà effectuée par la méthode. Il doit alors être exact. Néanmoins la figure ci-dessous montre que le p obtenu avec la méthode de Roth n'est pas égal à celui calculé par le découplage de Roth à paramètres équivalents.

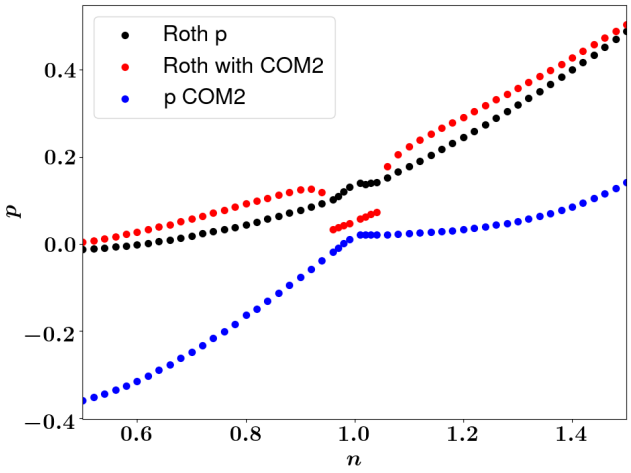

Figure 38: paramètre p calculé avec la méthode de Roth (points noirs), p calculé avec la méthode de Pauli (points bleus) et p calculé avec le découplage de Roth à partir des fonctions de corrélations obtenues avec la méthode de Pauli. Puisque le découplage de Roth ne suppose aucune autre approximation que celle des opérateurs composites, il devrait associer à p sa vraie valeur physique. Puisque les points bleus et rouge ne sont pas confondus, le p calculé avec la méthode de Pauli n'est pas contraint à la valeur physique qu'il devrait avoir. La méthode de Pauli n'est pas physique.

Fort de cette conclusion le reste du manuscrit se concentre sur le découplage de Roth. Une violation du théorème de Luttinger est observée, ce qui n'est pas inattendu puisque l'approximation de Hubbard I le violait aussi, et des articles utilisant la DQMC montraient aussi une violation [29]. La méthode est également étendue à la supraconduction, où nous concluons que la supraconduction prédite par la méthode n'est qu'une conséquence de la singularité de Van Hove. En effet sur la figure ci-dessous, il apparaît que le pic de la supraconductivité coïncide avec un pic dans la densité d'état à l'énergie de Fermi (densité calculée sans supraconduction). Cette coïncidence a été confirmée en étendant une deuxième fois la méthode à des voisins éloignés jusqu'à l'ordre 5 et en observant les mêmes pics coïncider.

Finalement, un nouveau système est étudié avec les opérateurs composites en se concentrant sur la solution issue du découplage de Roth: un modème de Hubbard à deux orbitales. Un diagramme de phase est calculé en fonction de l'énergie de saut inter-orbitale, et une phase de Mott orbitalement sélective apparaît quand cette énergie est suffisamment faible. Ceci traduit une brisure spontanée de la symmétrie orbitale qui a de l'intérêt dans le domaine des matériaux supraconducteurs à base de fer, où une telle phase a déjà été observée expérimentalement [84]. En parallèle, une phase orbitalement uniforme (où les deux orbitales sont identiques) est observable sur l'ensemble du diagramme de phase. Il est alors possible de calculer l'énergie libre des deux phases pour savoir quand l'une est favorable par rapport à l'autre. Ainsi, le diagramme de phase présenté en figure 31 possède une zone

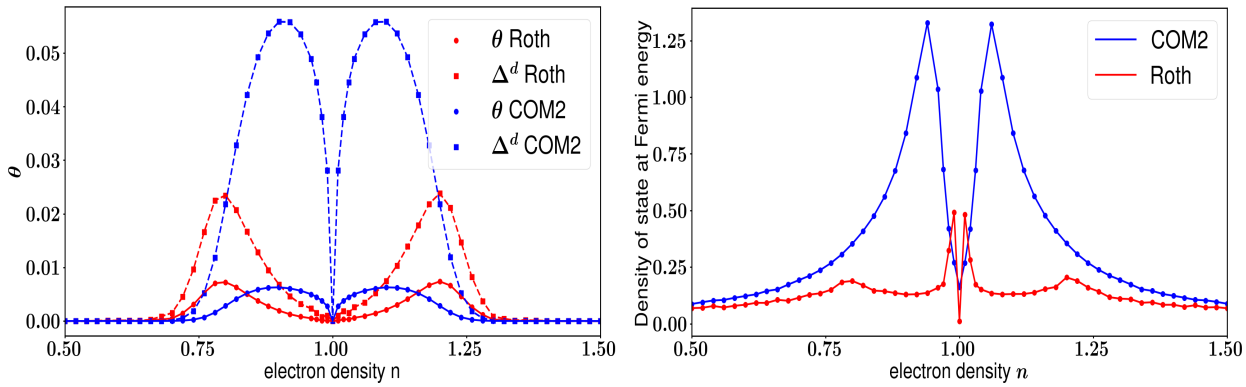

(a) paramètres θ et Δ^d.

(b) Densité d'état à l'énergie de Fermi.

Figure 39: (a) Paramètre d'ordre supraconducteur anormal θ calculé avec la méthode et paramètre d'ordre supraconducteur en symétrie d reconstruit avec les fonctions de corrélations. (b) Densité d'état à l'énergie de Fermi en l'absence de supraconduction. Les maximums de (a) et (b) coïncident: la supraconduction apparaît comme une conséquence de la singularité de Van Hove.

verte là où la phase orbitalement sélective est favorable, une zone blanche où elle est défavorable, et une ligne séparant la zone blanche selon que la solution peut être stabilisée (et est alors métastable) ou non.

$$i\frac{d}{dt}\begin{pmatrix}F_{ijl}(t)\\G_{ijl}(t)\end{pmatrix}=\sum_k \mathbf{E}_{ik}\begin{pmatrix}F_{klj}(t)\\G_{kjl}(t)\end{pmatrix}+\delta(t)\begin{pmatrix}f^1_{ijl}\\f^2_{ijl}\end{pmatrix} \tag{213}$$

B . Product of a real and symmetric matrix by a diagonal matrix has real eigenvalues

At the center of the composite operator method lies the **E** matrix, whose eigenvalues are correlated to the self-consistent parameters of the method. It is then important to know whether these eigenvalues can be complex or if they will always be real.

The **E** matrix is the product of a real and symmetric **M** matrix with a real diagonal **I** matrix, as described by Eq. 89. Let us show this implies that the eigenvalues of E are real.

The characteristic polynomial of a real symmetric $n \times n$ matrix M is given by the equation:

$$det(XId_n - M) = 0 \tag{214}$$

From spectral theorem it is known the eigenvalues of a symmetric matrix with real entries are real. Therefore the solution of the above characteristic polynomial (which are the eigenvalues) are real. Let us now consider the product of M by a diagonal $n \times n$ matrix with positive entries D:

$$E = MD \tag{215}$$

The characteristic polynomial can be rewritten as follow:

$$det(XId_n - MD) = det(D^{1/2}(Xid_n - D^{1/2}MD^{1/2})D^{-1/2}) \tag{216}$$

Using the product property of determinant $det(AB) = det(A)det(B)$ the right hand term can be simplified. It follows that the characteristic polynomial of $E = MD$ and $F = D^{1/2}MD^{-1/2}$ are the same. As a consequence, E and F matrices have the same eigenvalues. Since F is a product of a real symmetric eigenvalue by diagonal matrix, according to spectral theorem F has real eigenvalues. Therefore, E also has real eigenvalues.

Because of this, no broadening has to be considered as all involved quantities in the self-consistency are real.

C . Roth decoupling and computation of p

In this appendix we derive the self-consistent equation of

$$p(i-j) = \langle n_{i\uparrow}n_{j\uparrow}\rangle + \langle S_i^+ S_j^-\rangle - \langle \Delta_i \Delta_j^*\rangle \tag{217}$$

C.1 . Pair-pair term

Following the step of L. Roth [101], we express p as a function of correlation functions by mean of equations of motion.

First, notice we can write

$$\langle \Delta_i \Delta_j^*\rangle = \langle \xi_{i\uparrow} c_{i\downarrow}\Delta_j^*\rangle + \langle \eta_{i\uparrow} c_{i\downarrow}\Delta_j^*\rangle \tag{218}$$

Note we illustrate this decoupling with $\xi_{i\uparrow}$ and $\eta_{i\uparrow}$ but the idea is exactly the same with $\psi_{i\downarrow}$. We introduce the following Green's functions

$$\begin{cases} F_{ijl}(\tau) &= \langle\langle \xi_{i\uparrow}(\tau); c_{j\downarrow}\Delta_l^*\rangle\rangle \\ G_{ijl}(\tau) &= \langle\langle \eta_{i\uparrow}(\tau); c_{j\downarrow}\Delta_l^*\rangle\rangle \end{cases} \tag{219}$$

We then consider the equations of motion for these Green's functions

$$\begin{aligned} \partial_\tau \begin{pmatrix} F_{ijl}(\tau) \\ G_{ijl}(\tau)\end{pmatrix} &= \theta_H(\tau) \begin{pmatrix} \langle\{\partial_t \xi_{i\uparrow}(\tau); c_{j\downarrow}\Delta_l^*\}\rangle \\ \langle\{\partial_\tau \eta_{i\uparrow}(\tau); c_{j\downarrow}\Delta_l^*\}\rangle \end{pmatrix} \\ &+ \delta(\tau) \begin{pmatrix} f^1_{ijl} \\ f^2_{ijl}\end{pmatrix} \end{aligned} \tag{220}$$

where $f^n_{ijl} = \langle\{\psi_i^n; c_{j\downarrow}\Delta_l^*\}\rangle$. We now use Eq. (88) to obtain

$$\partial_\tau \begin{pmatrix} F_{ijl}(\tau) \\ G_{ijl}(\tau)\end{pmatrix} = \sum_k E_{ik} \begin{pmatrix} F_{kjl}(\tau) \\ G_{kjl}(\tau)\end{pmatrix} + \delta(\tau) \begin{pmatrix} f^1_{ijl} \\ f^2_{ijl}\end{pmatrix} \tag{221}$$

We then time and space Fourier transform associating the Fourier variable k_1 to $r_i - r_l$ and k_2 to $r_i - r_j$. The equation becomes

$$\begin{pmatrix} F_{k_1k_2}(\omega) \\ G_{k_1k_2}(\omega) \end{pmatrix} = (\omega \mathbf{Id}_2 - E_{k_1+k_2})^{-1} \begin{pmatrix} f^1_{k_1k_2} \\ f^2_{k_1k_2} \end{pmatrix} \tag{222}$$

Finally we use Eq. (91) to obtain

$$\begin{pmatrix} F_{k_1k_2}(\omega) \\ G_{k_1k_2}(\omega) \end{pmatrix} = S_{k_1+k_2}(\omega) I^{-1} \begin{pmatrix} f^1_{k_1k_2} \\ f^2_{k_1k_2} \end{pmatrix} \tag{223}$$

Finally, we can extract $\langle \Delta_i \Delta_j^* \rangle$ by summing F and G, integrating over ω and taking the imaginary part to use Eq. (94) in order to replace the composite Green's functions by correlation functions. We get

$$\begin{aligned} TF[\langle c_{i\sigma} c_{j\bar{\sigma}} \Delta_l^* \rangle](k_1, k_2) = & \frac{2}{2-n} \sum_k (C^{11}_{k_1+k_2} + C^{12}_{k_1+k_2}) f^1_{k_1k_2} \\ & + \frac{2}{n} \sum_k (C^{12}_{k_1+k_2} + C^{22}_{k_1+k_2}) f^2_{k_1k_2} \end{aligned} \tag{224}$$

We compute $f^n_{kjl} = \langle \{ \psi^n_k ; c_{j\downarrow} \Delta_l^* \} \rangle$ using the algebraic relations given in appendix C leads to

$$\begin{aligned} f^1_{ijl} =& \delta_{ij} \langle \Delta_i \Delta_l^* \rangle + \delta_{il} (C^{21}_{ij} + C^{22}_{ij}) \\ f^2_{ijl} =& -\delta_{ij} \langle \Delta_i \Delta_l^* \rangle + \delta_{il} (C^{11}_{ij} + C^{12}_{ij}) \end{aligned} \tag{225}$$

Performing a Fourier transform of f^1_{ijl} and f^2_{ijl} and setting i=j by integrating on k_2, then finally inverse Fourier transform on k_1 leads to:

$$\langle \Delta_i \Delta_l^* \rangle = \frac{4}{n(2-n)} \frac{(C^{11}_{il} + C^{12}_{il})(C^{22}_{il} + C^{21}_{il})}{1 - \frac{2}{2-n}(C^{11}_0 + C^{12}_0) + \frac{2}{n}(C^{21}_0 + C^{22}_0)} \tag{226}$$

Which is the form in the main text. We pose

$$\phi = -\frac{2}{2-n}(C^{11}_0 + C^{12}_0) + \frac{2}{n}(C^{21}_0 + C^{22}_0) \tag{227}$$

Replacing C^{11}_0 and C^{22}_0 by their definitions allows us to express these correlations function explicitly as a function of n. We don't explicit C^{12}_0 however, else it will be zero while it is not numerically: C^{12}_0 should stay in the numerical minimization process to obtain our results. Doing so leads to the following expression for ϕ

$$\phi = \frac{n^2 - 4(\frac{n}{2} - \langle n_{i\uparrow} n_{i\downarrow} \rangle - C^{12}_0)}{n(2-n)} \tag{228}$$

With our notations the pair-pair term becomes

$$\langle \Delta_i \Delta_l^* \rangle = \frac{\rho_3}{1+\phi} \tag{229}$$

C.2 . Spin-Spin term

The spin-spin term is defined as $\langle S_i^+ S_l^- \rangle = \langle c_{i\uparrow}^\dagger c_{i\downarrow} c_{l\downarrow}^\dagger c_{l\uparrow} \rangle$. In order to have our basis element as the first term, we rewrite it as

$$\langle S_i^+ S_l^- \rangle = -\langle c_{i\uparrow}^\dagger c_{i\downarrow} c_{l\uparrow} c_{l\downarrow}^\dagger \rangle = -\langle c_{l\uparrow} c_{l\downarrow}^\dagger c_{i\uparrow}^\dagger c_{i\downarrow} \rangle \tag{230}$$

We therefore introduce the following Green's functions (setting $\tau' = 0$)

$$\begin{cases} F_{ijl}(\tau) = & \langle\langle \xi_{i\uparrow}(\tau); c_{j\downarrow}^\dagger S_l^+ \rangle\rangle \\ G_{ijl}(\tau) = & \langle\langle \eta_{i\uparrow}(\tau); c_{j\downarrow}^\dagger S_l^+ \rangle\rangle \end{cases} \tag{231}$$

The next steps are the same as with the pair-pair term. The only difference lies in the definition of f^n in the resulting equations of motion. For the spin-spin term it is defined as $f_{ijl}^n = \langle \{ \psi_i^n; c_{j\downarrow}^\dagger S_l^+ \} \rangle$. Hence we arrive at the following equation

$$\begin{aligned} TF(\langle c_{i\uparrow} c_{j\downarrow}^\dagger S_l^+ \rangle)(k_1, k_2) = & \frac{2}{2-n} (C_{k_1+k_2}^{11} + C_{k_1+k_2}^{12}) f_{k_1 k_2}^1 \\ & + \frac{2}{n} (C_{k_1+k_2}^{12} + C_{k_1+k_2}^{22}) f_{k_1 k_2}^2 \end{aligned} \tag{232}$$

A computation of the f^n leads to

$$\begin{aligned} f_{ijl}^1 &= \delta_{ij} \langle S_i^- S_l^+ \rangle - \delta_{kl} (C_{ij}^{11} + C_{ij}^{12}) \\ f_{ijl}^2 &= -\delta_{ij} \langle S_i^- S_l^+ \rangle - \delta_{kl} (C_{ij}^{12} + C_{ij}^{22}) \end{aligned} \tag{233}$$

Therefore by Fourier transform the expression of f, then by integrating over k_2 to set i=j and by inverse Fourier transform on k_1, we obtain

$$\langle S_i^- S_l^+ \rangle = - \frac{\frac{2}{2-n} (C_{il}^{11} + C_{il}^{12})^2 + \frac{2}{n} (C_{il}^{12} + C_{22}^{il})^2}{1 + \frac{2}{2-n} (C_0^{11} + C_0^{12}) - \frac{2}{n} (C_0^{12} + C_0^{22})} \tag{234}$$

Which become with our notations

$$\langle S_i^- S_l^+ \rangle = \frac{\rho_1}{1 - \phi} \tag{235}$$

C.3 . Charge-Charge term

As we did for the $\langle S_i^- S_l^+ \rangle$ term we need to commute the charge charge term so the first element can be decomposed using our spinor. We then rewrite

$$\langle c_{i\uparrow}^\dagger c_{i\uparrow} n_{l\uparrow} \rangle = \frac{n}{2} - \langle c_{i\uparrow} c_{i\uparrow}^\dagger n_{l\uparrow} \rangle \tag{236}$$

We introduce the following Green's functions

$$\begin{cases} F_{ijl}(\tau) = & \langle\langle \xi_{i\uparrow}(\tau); c^\dagger_{j\uparrow} n_{l\uparrow}\rangle\rangle \\ G_{ijl}(\tau) = & \langle\langle \eta_{i\uparrow}(\tau); c^\dagger_{j\uparrow} n_{l\uparrow}\rangle\rangle \end{cases} \tag{237}$$

Once again the general form of the equation for $\langle c_{i\sigma} c^\dagger_{i\sigma} n_{l\sigma}\rangle$ will be the same as for the other 2 terms. However the definition of the involved f^n_{ijl} will not be the same. We compute $f^n_{ijl} = \langle\{\psi^n_i; c^\dagger_{j\uparrow} n_{l\uparrow}\}\rangle$

$$\begin{aligned} f^1_{ijl} &= \delta_{ij}(\frac{n}{2} - \langle n_{i\downarrow} n_{l\uparrow}\rangle) + \delta_{il}(C^{11}_{ij} + C^{12}_{ij}) \\ f^2_{ijl} &= \delta_{ij}\langle n_{i\downarrow} n_{l\uparrow}\rangle + \delta_{il}(C^{12}_{ij} + C^{22}_{ij}) \end{aligned} \tag{238}$$

We hence obtain

$$\langle n_{i\uparrow} n_{l\uparrow}\rangle = \frac{n}{2} - \rho_1 - \phi\langle n_{i\uparrow} n_{l\downarrow}\rangle + \frac{n}{2-n}(C^{11}_0 + C^{12}_0) \tag{239}$$

We don't know how to express $\langle n_{i\downarrow} n_{l\uparrow}\rangle$ as a function of the correlations functions. So we need to redo this decoupling on this term. This time we use

$$\langle n_{i\downarrow} n_{l\uparrow}\rangle = \frac{n}{2} - \langle c_{l\uparrow} c^\dagger_{l\uparrow} n_{i\downarrow}\rangle \tag{240}$$

We therefore introduce

$$\begin{cases} F_{ijl}(\tau) = & \langle\langle \xi_{i\uparrow}(\tau); c^\dagger_{j\uparrow} n_{l\downarrow}\rangle\rangle \\ G_{ijl}(\tau) = & \langle\langle \eta_{i\uparrow}(\tau); c^\dagger_{j,\uparrow} n_{l\downarrow}\rangle\rangle \end{cases} \tag{241}$$

The $f^n_{ijl} = \langle\psi^n_i, c^\dagger_{j\uparrow} n_{l\downarrow}\rangle$ are given by

$$\begin{aligned} f^1_{ijl} &= \delta_{ij}(\frac{n}{2} - \langle n_{i\downarrow} n_{l\downarrow}\rangle) \\ f^2_{ijl} &= \delta_{ij}\langle n_{i\downarrow} n_{l\downarrow}\rangle \end{aligned} \tag{242}$$

Using the paramagnetic assumption we have $\langle n_{i\uparrow} n_{l\uparrow}\rangle = \langle n_{i\downarrow} n_{l\downarrow}\rangle$, leading to

$$\langle n_{i\uparrow} n_{l\downarrow}\rangle = \frac{n}{2} - \phi\langle n_{i\uparrow} n_{l\uparrow}\rangle + \frac{n}{2-n}(C^{11}_0 + C^{12}_0) \tag{243}$$

If we inject this in the equation of $\langle n_{i\uparrow} n_{l\uparrow}\rangle$, we obtain

$$\langle n_{i\uparrow} n_{l\uparrow}\rangle = -\rho_1 + \phi^2\langle n_{i\uparrow} n_{l\uparrow}\rangle + \frac{n}{2-n}(C^{11}_0 + C^{12}_0)(1-\phi) \tag{244}$$

The last term can be simplified. An explicit computations of the C_0 leads to $C^{11}_0 + C^{12}_0 = 1 - n + \langle n_{i\uparrow} n_{i\downarrow}\rangle$, allowing us to show the last term is in fact just equal to $\frac{n^2}{4}$. We therefore obtain

$$\langle n_{i\uparrow} n_{l\downarrow}\rangle = \frac{n^2}{4} - \frac{\rho_1}{1-\phi^2} \tag{245}$$

Which is the self consistent equation we have. Combining the three terms, since $p = \langle n_{i\uparrow} n_{l\uparrow}\rangle + \langle S^+_i S^-_l\rangle - \langle \Delta_i \Delta^*_l\rangle$, we obtain the following self consistent equation

$$p = \frac{n^2}{4} - \frac{\rho_1}{1-\phi^2} - \frac{\rho_1}{1-\phi} - \frac{\rho_3}{1+\phi} \tag{246}$$

D . Roth decoupling with superconductivity

In this appendix we show how Roth decoupling changes when we include superconductivity with 4x4 basis. We will redo one of the terms of p as an example, and perform the decoupling for the θ parameter. Let us start by considering $\langle S_i^- S_l^+ \rangle$ in p for example. The superconducting basis is of size 4 and define by

$$\psi = \begin{pmatrix} \xi_{i\uparrow} \\ \eta_{i\uparrow} \\ \xi_{i\downarrow}^\dagger \\ \eta_{i\downarrow}^\dagger \end{pmatrix} \tag{247}$$

To include the full basis we need to introduce 4 Green's functions now

$$\begin{aligned} A_{ijl} =& \langle\langle \xi_{i\uparrow}; c_{j\downarrow}^\dagger S_l^+ \rangle\rangle \\ B_{ijl} =& \langle\langle \eta_{i\uparrow}; c_{j\downarrow}^\dagger S_l^+ \rangle\rangle \\ F_{ijl} =& \langle\langle \xi_{i\downarrow}^\dagger; c_{j\downarrow}^\dagger S_l^+ \rangle\rangle \\ G_{ijl} =& \langle\langle \eta_{i\downarrow}^\dagger; c_{j\downarrow}^\dagger S_l^+ \rangle\rangle \end{aligned} \tag{248}$$

Now the equations of motion has to be defined for the 4 Green's functions. Hence

$$\partial_\tau \begin{pmatrix} A_{ijl} \\ B_{ijl} \\ F_{ijl} \\ G_{ijl} \end{pmatrix} (\tau) = \sum_k E_{ik} \begin{pmatrix} A_{ijl} \\ B_{ijl} \\ F_{ijl} \\ G_{ijl} \end{pmatrix} (\tau) + \delta(\tau) \begin{pmatrix} f_{ijl}^1 \\ f_{ijl}^2 \\ f_{ijl}^3 \\ f_{ijl}^4 \end{pmatrix} \tag{249}$$

With $f_{ijl}^n = \langle \{ \psi_i^n; c_{j\downarrow}^\dagger S_l^+ \} \rangle$. As before we can use the relation $(\omega - E_k) = S_k(\omega) I^{-1}$ after a space Fourier transform and integrate over ω after we took the imaginary part to replace the composite Green's function matrix by a correlation function matrix. Thus

$$\begin{aligned} -TF[\langle c_{j\downarrow}^\dagger c_{i\uparrow} S_l^+ \rangle](k_1, k_2) =& \frac{2}{2-n} [(C_{k_1+k_2}^{11} + C_{k_1+k_2}^{12}) f_{k_1 k_2}^1 + (C_{k_1+k_2}^{12} + C_{k_1+k_2}^{22}) f_{k_1 k_2}^2 \\ &+ (C_{k_1+k_2}^{13} + C_{k_1+k_2}^{23}) f_{k_1 k_2}^3 + (C_{k_1+k_2}^{14} + C_{k_1+k_2}^{24}) f_{k_1 k_2}^4] \end{aligned} \tag{250}$$

In the last equation, the first line is the same as before, while the second line are additionnal terms appearing with the superconducting basis. f^1 and f^2 have already been computed before in Eq. (233). We give here f^3 and f^4:

$$\begin{aligned} f_{ijl}^3 =& \delta_{il} (C_{ij}^{13} + C_{ij}^{14}) \\ f_{ijl}^4 =& \delta_{il} (C_{ij}^{23} + C_{ij}^{24}) \end{aligned} \tag{251}$$

Finally the spin-spin term in p becomes

$$\langle S_i^- S_l^+ \rangle = - \frac{\rho_1 + \rho_2}{1 - \phi} \tag{252}$$

With $\rho_2 = \frac{2}{2-n}(C_{il}^{13} + C_{il}^{14})^2 + \frac{2}{n}(C_{il}^{23} + C_{il}^{24})^2$.

Now we move on to the Roth decoupling for θ. We consider a decoupling starting from $\langle\langle c_{i\downarrow}^\dagger, c_{i\uparrow}^\dagger n_{l\sigma}\rangle\rangle$. We introduce the following Green's functions

$$\begin{pmatrix} A_{ijl} = & \langle\langle \xi_{i\uparrow}; c_{j\uparrow}^\dagger n_{l\uparrow}\rangle\rangle \\ B_{ijl} = & \langle\langle \eta_{i\uparrow}; c_{j\uparrow}^\dagger n_{l\uparrow}\rangle\rangle \\ F_{ijl} = & \langle\langle \xi_{i\downarrow}^\dagger; c_{j\uparrow}^\dagger n_{l\uparrow}\rangle\rangle \\ G_{ijl} = & \langle\langle \eta_{i\downarrow}^\dagger; c_{j\uparrow}^\dagger n_{l\uparrow}\rangle\rangle \end{pmatrix} \tag{253}$$

The decoupling is identical and by considering F+G we arrive to

$$\begin{aligned} TF[\langle c_{i\downarrow}^\dagger c_{j\uparrow}^\dagger n_{l\sigma}\rangle](k_1,k_2) = & \frac{2}{2-n}[(C_{k_1+k_2}^{13} + C_{k_1+k_2}^{14}) f_{k_1k_2}^1 \\ & + (C_{k_1+k_2}^{33} + C_{k_1+k_2}^{44}) f_{k_1k_2}^3] \\ & + \frac{2}{n}[(C_{k_1+k_2}^{23} + C_{k_1+k_2}^{24}) f_{k_1k_2}^2 \\ & + (C_{k_1+k_2}^{34} + C_{k_1+k_2}^{44}) f_{k_1k_2}^4] \end{aligned} \tag{254}$$

With $f_{ijl}^n = \langle\{\psi_i^n; c_{j\uparrow}^\dagger n_{l\sigma}\}\rangle$. Computing the f gives

$$\begin{aligned} f_{ijl}^1 =& \delta_{ij}(\frac{n}{2} - \langle n_{i\uparrow} n_{l\uparrow}\rangle) + \delta_{il}(C_{ij}^{11} + C_{ij}^{12}) \\ f_{ijl}^2 =& \delta_{ij}\langle n_{i\uparrow} n_{l\uparrow}\rangle + \delta_{il}(C_{ij}^{12} + C_{ij}^{22}) \\ f_{ijl}^3 =& -\delta_{ij}\frac{\theta_{il}}{2} \\ f_{ijl}^4 =& \delta_{ij}\frac{\theta_{il}}{2} \end{aligned} \tag{255}$$

We therefore obtain

$$\begin{aligned} \frac{\theta}{2} =& \frac{\langle n_{i\uparrow} n_{l\uparrow}\rangle[\frac{2}{n}(C_0^{23} + C_0^{24}) - \frac{2}{2-n}(C_0^{13} + C_0^{14})] + \zeta}{1+\phi} \\ & + \frac{n}{2}\frac{C_0^{13} + C_0^{14}}{1+\phi} \end{aligned} \tag{256}$$

With $\zeta = \frac{2}{2-n}(C_{il}^{11} + C_{il}^{12})(C_{il}^{13} + C_{il}^{14}) + \frac{2}{n}(C_{il}^{12} + C_{il}^{22})(C_{il}^{23} + C_{il}^{24})$. Finally by noting that $C_0^{23} + C_0^{24} = 0$ and $C_0^{13} + C_0^{14} = 0$, we obtain the equation we used

$$\frac{\theta}{2} = \frac{\zeta}{1+\phi} \tag{257}$$

Let us finally note several decoupling are possible for the 4×4 basis. As mentioned in Ref. [102], these choices will over estimate or underestimate the real value of θ but the behaviour will remain globally the same [104]. For θ, another choice of Roth decoupling would start by considering $\theta_{il} = \langle c_{i\uparrow} c_{i\downarrow} n_{l\sigma}\rangle$. This definition is equivalent to the other one because of singlet pairing assumption. We can then introduce the following set of Green's functions:

$$\begin{pmatrix} A_{ijl} = \langle\langle \xi_{i\uparrow}; c_{j\downarrow} n_{l\sigma} \rangle\rangle \\ B_{ijl} = \langle\langle \eta_{i\uparrow}; c_{j\downarrow} n_{l\sigma} \rangle\rangle \\ F_{ijl} = \langle\langle \eta^\dagger_{i\downarrow}; c_{j\downarrow} n_{l\sigma} \rangle\rangle \\ G_{ijl} = \langle\langle \eta^\dagger_{i\downarrow}; c_{j\downarrow} n_{l\sigma} \rangle\rangle \end{pmatrix} \tag{258}$$

We would then have to consider A+B in order to rebuild θ. Note there are several decoupling choice for p too. In the $\psi = (\xi_{i\uparrow}, \eta_{i\uparrow})^T$ case, there is only one possible decoupling for p, but the more the basis is extended the more choices are possible. When several choices can be considered, the final expression should be symmetrized and consider all of the possible Roth decoupling.

E . Roth decoupling for the 2 orbital Hubbard model

E.1 . Decoupling of px and py

In this appendix we give more details on how Roth decoupling was done for each terms.
We introduce the 4 following Green's function:

$$\begin{pmatrix} A \\ B \\ F \\ G \end{pmatrix}_{ijk} (\tau) = \begin{pmatrix} \langle\langle \xi_{ix\uparrow}(\tau); c_{jx\downarrow} \Delta^*_{kx} \rangle\rangle \\ \langle\langle \eta_{ix\uparrow}(\tau); c_{jx\downarrow} \Delta^*_{kx} \rangle\rangle \\ \langle\langle \xi_{iy\uparrow}(\tau); c_{jx\downarrow} \Delta^*_{kx} \rangle\rangle \\ \langle\langle \eta_{iy\uparrow}(\tau); c_{jx\downarrow} \Delta^*_{kx} \rangle\rangle \end{pmatrix} \tag{259}$$

Let's derive the equations of motion of these Green's functions:

$$\partial_\tau \begin{pmatrix} A \\ B \\ F \\ G \end{pmatrix}_{ijk} (\tau) = \delta(\tau) \begin{pmatrix} f^1 \\ f^2 \\ f^3 \\ f^4 \end{pmatrix}_{ijk} + \theta_H(\tau) \begin{pmatrix} \langle\{\partial_\tau \xi_{ix\uparrow}(\tau); c_{jx\downarrow} \Delta^*_{kx}\}\rangle \\ \langle\{\partial_\tau \eta_{ix\uparrow}(\tau); c_{jx\downarrow} \Delta^*_{kx}\}\rangle \\ \langle\{\partial_\tau \xi_{iy\uparrow}(\tau); c_{jx\downarrow} \Delta^*_{kx}\}\rangle \\ \langle\{\partial_\tau \eta_{iy\uparrow}(\tau); c_{jx\downarrow} \Delta^*_{kx}\}\rangle \end{pmatrix} \tag{260}$$

With $f^n_{ijk} = \langle\{\psi^n_{ijk}; c_{j\downarrow x} \Delta^*_{kx}\}\rangle$. We now use the main approximation of the composite operator method Eq. (173) to get:

$$\partial_\tau \begin{pmatrix} A \\ B \\ F \\ G \end{pmatrix}_{ijk} (\tau) = \delta(\tau) \begin{pmatrix} f^1 \\ f^2 \\ f^3 \\ f^4 \end{pmatrix}_{ijk} + \sum_l E_{il} \begin{pmatrix} A \\ B \\ F \\ G \end{pmatrix}_{ljk} (\tau) \tag{261}$$

After a time Fourier transform we can rewrite this equation as:

$$\sum_l (\omega \delta_{il} Id_4 - E_{il}) \begin{pmatrix} A \\ B \\ F \\ G \end{pmatrix}_{ljk} (\omega) = \begin{pmatrix} f^1 \\ f^2 \\ f^3 \\ f^4 \end{pmatrix}_{ijk} \tag{262}$$

We now use the equation of motion (Eq. (174)) to get:

$$\begin{pmatrix} A \\ B \\ F \\ G \end{pmatrix}_{ijk}(\omega) = \sum_l S_{il}(\omega) I_i^{-1} \begin{pmatrix} f^1 \\ f^2 \\ f^3 \\ f^4 \end{pmatrix}_{ljk} \tag{263}$$

We used the global δ_{ij} prefactor in the I matrix to rewrite it as $I_{ij}^{nm} = \delta_{ij} I_i^{nm}$. We can now take the imaginary part and integrate over frequencies in order to use fluctuation-dissipation theorem (Eq. (104):

$$\begin{pmatrix} \langle \xi_{ix\uparrow} c_{jx\downarrow} \Delta_{kx}^* \rangle \\ \langle \eta_{ix\uparrow} c_{jx\downarrow} \Delta_{kx}^* \rangle \\ \langle \xi_{iy\uparrow} c_{jx\downarrow} \Delta_{kx}^* \rangle \\ \langle \eta_{iy\uparrow} c_{jx\downarrow} \Delta_{kx}^* \rangle \end{pmatrix} = \sum_l C_{il} I_i^{-1} \begin{pmatrix} f^1 \\ f^2 \\ f^3 \\ f^4 \end{pmatrix}_{ljk} \tag{264}$$

I_i^{-1} is diagonal. Now we need to compute the matricial products and consider the sum of the two first components of the vector of the left hand side of the equation. Using the fact that $\xi_{ix\uparrow} + \eta_{ix\uparrow} = c_{ix\uparrow}$, we obtain:

$$\begin{aligned} \langle c_{ix\uparrow} c_{jx\downarrow} \Delta_{kx}^* \rangle = \sum_l & \alpha_{ix} (C_{il}^{11} + C_{il}^{21}) f_{ljk}^1 + \beta_{ix} (C_{il}^{12} + C_{il}^{22}) f_{ljk}^2 \\ & + \alpha_{iy} (C_{il}^{13} + C_{il}^{23}) f_{ljk}^3 + \beta_{iy} (C_{il}^{14} + C_{il}^{24}) f_{ljk}^4 \end{aligned} \tag{265}$$

With:

$$\begin{aligned} \alpha_{ix} &= (I_i^{-1})^{11} = \frac{2}{2 - n_{ix}} \qquad \alpha_{iy} = (I_i^{-1})^{33} = \frac{2}{2 - n_{iy}} \\ \beta_{ix} &= (I_i^{-1})^{22} = \frac{2}{n_{ix}} \qquad \beta_{iy} = (I_i^{-1})^{44} = \frac{2}{n_{iy}} \end{aligned} \tag{266}$$

The only thing left is to compute explicitly the f^n and take i=j. We get:

$$\begin{aligned} f_{ljk}^1 &= \delta_{lj} \langle \Delta_j \Delta_k^* \rangle + \delta_{lk} (C_{ik}^{12} + C_{ik}^{22}) \\ f_{ljk}^2 &= -\delta_{lj} \langle \Delta_j \Delta_k^* \rangle + \delta_{lk} (C_{ik}^{11} + C_{ik}^{12}) \\ f_{ljk}^3 &= 0 \\ f_{ljk}^4 &= 0 \end{aligned} \tag{267}$$

f^3 and f^4 vanishes because they only contain commutators of x operators with y operators. In the end, we get the same expression for $\langle \Delta_{ix} \Delta_{iy}^* \rangle$ as in the uniform case:

$$\langle \Delta_{ix} \Delta_{kx}^* \rangle = (\alpha_{ix} + \beta_{ix}) \frac{(C_{ik}^{11} + C_{ik}^{12})(C_{ik}^{22} + C_{ik}^{12})}{1 - \alpha_{ix}(C_{ii}^{11} + C_{ii}^{12}) + \beta_{ix}(C_{ii}^{22} + C_{ii}^{12})} \tag{268}$$

Every other terms in p_{ijx} and p_{ijy} will also be similar to the uniform case because the f^3 and f^4 that will be considered in the decoupling will vanish for p_{ijx} quantities while for p_{ijy} it will be f^1 and f^2 that vanish. Roth decoupling will be exactly the same for p_{xy}.

Let's detail the other terms of p_x and p_y. First it is important to notice that p_x and p_y decoupling will be exactly the same but with the top-left block for the x channel and the bottom-right block for the y channel of the I and C matrix. This means that an $\alpha_x = (I^{-1})^{11}$ for p_x will become $\alpha_y = (I^{-1})^{33}$ for p_y, and a $C^{11} = \langle \xi_{ix\uparrow} \xi^\dagger_{ix\uparrow} \rangle$ for p_x will become $C^{33} = \langle \xi_{iy\uparrow} \xi^\dagger_{iy\uparrow} \rangle$ for p_y. For this reason we will only consider terms of p_x here.

Let's start with $\langle S^-_{ix} S^+_{kx} \rangle$ with i and k nearest neighbors. We start by rewriting :

$$\langle S^-_{ix} S^+_{kx} \rangle = -\langle c_{i\uparrow} c^\dagger_{i\downarrow} S^+_{kx} \rangle \tag{269}$$

This way we can introduce the following Green's functions:

$$\begin{pmatrix} A \\ B \\ F \\ G \end{pmatrix}_{ijk} = \begin{pmatrix} \langle\langle \xi_{ix\uparrow}; c^\dagger_{jx\downarrow} S^+_{kx} \rangle\rangle \\ \langle\langle \eta_{ix\uparrow}; c^\dagger_{jx\downarrow} S^+_{kx} \rangle\rangle \\ \langle\langle \xi_{iy\uparrow}; c^\dagger_{jx\downarrow} S^+_{kx} \rangle\rangle \\ \langle\langle \eta_{iy\uparrow}; c^\dagger_{jx\downarrow} S^+_{kx} \rangle\rangle \end{pmatrix} \tag{270}$$

The steps that follow are similar to what was detailed in the main text: we consider the equation of motion, and use a time Fourier transform and the equation of motion Eq. (174) to obtain:

$$\begin{pmatrix} A \\ B \\ F \\ G \end{pmatrix}_{ijk} (\omega) = \sum_l S_{il}(\omega) I_i^{-1} \begin{pmatrix} f^1 \\ f^2 \\ f^3 \\ f^4 \end{pmatrix}_{ljk} \tag{271}$$

This time, f^n_{ljk} is defined by $f^n_{ljk} = \langle \{ \psi^n_l ; c^\dagger_{jx\downarrow} S^+_{kx} \} \rangle$. Now one can apply fluctuation dissipation theorem to replace Green's functions by correlation functions and sum over the two first components of the vector of Green's functions (so that we obtain $\langle \xi_{ix\uparrow} + \eta_{ix\uparrow} c^\dagger_{jx\downarrow} S^+_{kx} \rangle$):

$$\begin{aligned} \langle c_{ix\uparrow} c^\dagger_{jx\downarrow} S^+_{kx} \rangle = \sum_l & \alpha_{ix} (C^{11}_{il} + C^{21}_{il}) f^1_{ljk} + \beta_{ix} (C^{12}_{il} + C^{22}_{il}) f^2_{ljk} \\ & + \alpha_{iy} (C^{13}_{il} + C^{23}_{il}) f^3_{ljk} + \beta_{iy} (C^{14}_{il} + C^{24}_{il}) f^4_{ljk} \end{aligned} \tag{272}$$

A computation of f^n_{ljk} leads to:

$$\begin{aligned} f^1_{ljk} &= \delta_{lj} \langle S^-_{ix} S^+_{kx} \rangle - \delta_{kl} (C^{11}_{ik} + C^{12}_{ik}) \\ f^2_{ljk} &= -\delta_{lj} \langle S^-_{ix} S^+_{kx} \rangle - \delta_{kl} (C^{12}_{ik} + C^{22}_{ik}) \\ f^3_{ljk} &= 0 \\ f^4_{ljk} &= 0 \end{aligned} \tag{273}$$

Again, if we were considering $\langle S^-_{iy}S^+_{ky}\rangle$, f^1 and f^2 will vanish and f^3 and f^4 will have the same form of f^1 and f^2 but with $\alpha_x \to \alpha_y$, $C^{11} \to C^{33}$, ...

Finally, we get the following expression for $\langle S^-_{ix}S^+_{ky}\rangle = -\langle c_{i\uparrow}c^\dagger_{i\downarrow}S^+_{kx}\rangle$:

$$\langle S^-_{ix}S^+_{kx}\rangle = -\frac{\rho'_x}{1-\phi_x} \tag{274}$$

With ρ'_x and ϕ_x defined in the main text.

The last term of p_x we haven't considered yet is $\langle n_{ix\uparrow}n_{kx\uparrow}$. This term is a bit more difficult to decouple. Let's start by rewriting it as:

$$\langle n_{ix\uparrow}n_{kx\uparrow}\rangle = \frac{n_{kx}}{2} - \langle c_{ix\uparrow}c^\dagger_{ix\uparrow}n_{kx\uparrow}\rangle \tag{275}$$

We introduce the four following Green's functions:

$$\begin{pmatrix} A \\ B \\ F \\ G \end{pmatrix}_{ijk} = \begin{pmatrix} \langle\langle \xi_{ix\uparrow}; c^\dagger_{jx\uparrow}n_{kx\uparrow}\rangle\rangle \\ \langle\langle \eta_{ix\uparrow}; c^\dagger_{jx\uparrow}n_{kx\uparrow}\rangle\rangle \\ \langle\langle \xi_{iy\uparrow}; c^\dagger_{jx\uparrow}n_{kx\uparrow}\rangle\rangle \\ \langle\langle \eta_{iy\uparrow}; c^\dagger_{jx\uparrow}n_{kx\uparrow}\rangle\rangle \end{pmatrix} \tag{276}$$

Again, the following steps are similar to what is detailed in the main text. We will sum the two first components to reconstruct $\langle c_{ix\uparrow}c^\dagger_{ix\uparrow}n_{kx\uparrow}\rangle$. We get:

$$\begin{aligned}\langle c_{ix\uparrow}c^\dagger_{jx\uparrow}n_{kx\uparrow}\rangle = \sum_l \alpha_{ix}(C^{11}_{il}+C^{21}_{il})f^1_{ljk} + \beta_{ix}(C^{12}_{il}+C^{22}_{il})f^2_{ljk} \\ + \alpha_{iy}(C^{13}_{il}+C^{23}_{il})f^3_{ljk} + \beta_{iy}(C^{14}_{il}+C^{24}_{il})f^4_{ljk}\end{aligned} \tag{277}$$

This time, $f^n_{ljk} = \langle\{\psi_l; c^\dagger_{jx\uparrow}n_{kx\uparrow}\}\rangle$. A direct computation of the anticommutators leads to:

$$\begin{aligned} f^1_{ljk} &= \delta_{lj}(\frac{n_{kx}}{2} - \langle n_{jx\downarrow}n_{kx\uparrow}\rangle) + \delta_{lk}(C^{11}_{lj}+C^{12}_{lj}) \\ f^2_{ljk} &= \delta_{lj}\langle n_{jx\downarrow}n_{kx\uparrow}\rangle + \delta_{lk}(C^{12}_{lj}+C^{22}_{lj}) \\ f^3_{ljk} &= 0 \\ f^4_{ljk} &= 0 \end{aligned} \tag{278}$$

Hence we get:

$$\langle n_{ix\uparrow}n_{kx\uparrow}\rangle = \frac{n_x}{2} - \alpha_x(C^{11}_0+C^{12}_0)\frac{n_x}{2} - \langle n_{ix\downarrow}n_{kx\uparrow}\rangle\phi_x - \rho'_x \tag{279}$$

$\langle n_{ix\downarrow}n_{kx\uparrow}\rangle$ is unknown and must be decouple again with Roth's method. We have:

$$\langle n_{ix\downarrow}n_{kx\uparrow}\rangle = \langle n_{kx\uparrow}n_{ix\downarrow}\rangle = \frac{n_{ix}}{2} - \langle c_{kx\uparrow}c^\dagger_{kx\uparrow}n_{ix\downarrow}\rangle \tag{280}$$

Hence we introduce A, B, F, G $= \langle \psi_i^n; c_{jx\uparrow}^\dagger n_{kx\downarrow} \rangle$. Everything that follows is the same, and we get:

$$\langle n_{ix\uparrow} n_{kx\downarrow} \rangle = \frac{n_x}{2} - \phi_x \langle n_{ix\uparrow} n_{kx\uparrow} \rangle - \alpha_x (C_0^{11} + C_0^{12}) \frac{n_x}{2} \tag{281}$$

With this equation we can express $\langle n_{ix\uparrow} n_{kx\uparrow} \rangle$. We obtain:

$$\langle n_{ix\uparrow} n_{kx\uparrow} \rangle = \frac{(n_x)^2}{4} - \frac{\rho_x'}{1 - (\phi_x)^2} \tag{282}$$

To obtain this result we computed explicitly the C_0 and expressed everything as a function of n_x.

E.2 . Decoupling of pxy

p_{xy} involves two bodies on the same site but on different orbitals. The method we used with p_x and p_y will mainly be unchanged, except that at the end we will take i=j=k. It is important to note however that there are two ways of decoupling each terms: in the x or in the y channel. Let's start with $\langle \Delta_{ix} \Delta_{iy}^* \rangle$, in the x channel. We introduce the following four Green's functions:

$$\begin{pmatrix} A \\ B \\ F \\ G \end{pmatrix}_{ijk} (\omega) = \begin{pmatrix} \langle\langle \xi_{ix\uparrow}; c_{jx\downarrow} \Delta_{ky}^* \rangle\rangle \\ \langle\langle \eta_{ix\uparrow}; c_{jx\downarrow} \Delta_{ky}^* \rangle\rangle \\ \langle\langle \xi_{iy\uparrow}; c_{jx\downarrow} \Delta_{ky}^* \rangle\rangle \\ \langle\langle \eta_{iy\uparrow}; c_{jx\downarrow} \Delta_{ky}^* \rangle\rangle \end{pmatrix} \tag{283}$$

We say this decoupling is in the x channel because to reconstruct $\Delta_x \Delta_y^*$ we need to sum the composite operator of the x orbital. The step that follow are the same than before. We get:

$$\begin{aligned} \langle c_{ix\uparrow} c_{jx\downarrow} \Delta_{ky}^* \rangle = \sum_l & \alpha_{ix} (C_{il}^{11} + C_{il}^{21}) f_{ljk}^1 + \beta_{ix} (C_{il}^{12} + C_{il}^{22}) f_{ljk}^2 \\ & + \alpha_{iy} (C_{il}^{13} + C_{il}^{23}) f_{ljk}^3 + \beta_{iy} (C_{il}^{14} + C_{il}^{24}) f_{ljk}^4 \end{aligned} \tag{284}$$

With $f_{ljk}^n = \langle \psi_i^n c_{jx\uparrow} \Delta_{ky}^* \rangle$. An explicit computation leads to:

$$\begin{aligned} f_{ljk}^1 &= \delta_{lj} \langle \Delta_{lx} \Delta_{ky}^* \rangle \\ f_{ljk}^2 &= -\delta_{lj} \langle \Delta_{lx} \Delta_{ky}^* \rangle \\ f_{ljk}^3 &= \delta_{lk} (C_{jk}^{14} + C_{jk}^{24}) \\ f_{ljk}^4 &= \delta_{lk} (C_{jk}^{13} + C_{jk}^{23}) \end{aligned} \tag{285}$$

Note that the four f^n are non zero because both x and y terms appears in p_{xy}. This term is the one which couple x and y. Hence, after setting i=j and k=i we obtain the following equation :

$$\langle \Delta_{ix} \Delta_{iy}^* \rangle = \frac{\Omega_y'}{1 + \phi_x} \tag{286}$$

With:

$$\begin{aligned}\Omega'_y &= (\alpha_y + \beta_y)(C_0^{13} + C_0^{23})(C_0^{14} + C_0^{24}) \\ \phi_x &= -\alpha_x(C_0^{11} + C_0^{21}) + \beta_x(C_0^{12} + C_0^{22})\end{aligned} \tag{287}$$

For completion, let's do the decoupling in the y channel. Then, we introduce the following Green's function, after noticing that $\langle \Delta_x \Delta_y^* \rangle = \langle \Delta_y \Delta_x^* \rangle$ due to translational invariance.

$$\begin{pmatrix} A' \\ B' \\ F' \\ G' \end{pmatrix}_{ijk} (\omega) = \begin{pmatrix} \langle\langle \xi_{ix\uparrow}; c_{jy\downarrow} \Delta_{kx}^* \rangle\rangle \\ \langle\langle \eta_{ix\uparrow}; c_{jy\downarrow} \Delta_{kx}^* \rangle\rangle \\ \langle\langle \xi_{iy\uparrow}; c_{jy\downarrow} \Delta_{kx}^* \rangle\rangle \\ \langle\langle \eta_{iy\uparrow}; c_{jy\downarrow} \Delta_{kx}^* \rangle\rangle \end{pmatrix} \tag{288}$$

Since now we want to sum the composite operator in the y channel, we want to consider F'+G'. After the same procedure, we get the following equation:

$$\begin{aligned}\langle c_{ix\uparrow} c_{jx\downarrow} \Delta_{ky}^* \rangle = \sum_l &\alpha_{ix}(C_{il}^{31} + C_{il}^{41}) f_{ljk}'^1 + \beta_{ix}(C_{il}^{32} + C_{il}^{42}) f_{ljk}'^2 \\ &+ \alpha_{iy}(C_{il}^{33} + C_{il}^{43}) f_{ljk}'^3 + \beta_{iy}(C_{il}^{34} + C_{il}^{44}) f_{ljk}^4\end{aligned} \tag{289}$$

With $f_{ljk}'^n = \langle \psi_i^n c_{jy\uparrow} \Delta_{kx}^* \rangle$. An explicit computation leads to:

$$\begin{aligned} f_{ljk}'^1 &= \delta_{lk}(C_{jk}^{32} + C_{jk}^{42}) \\ f_{ljk}'^2 &= \delta_{lk}(C_{jk}^{31} + C_{jk}^{41}) \\ f_{ljk}'^3 &= \delta_{lj} \langle \Delta_{ly} \Delta_{kx}^* \rangle \\ f_{ljk}'^4 &= -\delta_{lj} \langle \Delta_{ly} \Delta_{kx}^* \rangle \end{aligned} \tag{290}$$

We get:

$$\langle \Delta_{iy} \Delta_{ix}^* \rangle = \frac{\Omega'_x}{1 + \phi_y} \tag{291}$$

With:

$$\begin{aligned}\Omega'_x &= (\alpha_x + \beta_x)(C_0^{31} + C_0^{32})(C_0^{41} + C_0^{42}) \\ \phi_y &= -\alpha_y(C_0^{33} + C_0^{43}) + \beta_y(C_0^{34} + C_0^{44})\end{aligned} \tag{292}$$

Let's move on to $\langle S_{ix}^- S_{iy}^+ \rangle = -\langle c_{ix\uparrow} c_{ix\uparrow}^\dagger S_{iy}^+ \rangle$. We introduce the following Green's functions:

$$\begin{pmatrix} A \\ B \\ F \\ G \end{pmatrix}_{ijk} (\omega) = \begin{pmatrix} \langle\langle \xi_{ix\uparrow}; c_{jx\downarrow}^\dagger S_{ky}^+ \rangle\rangle \\ \langle\langle \eta_{ix\uparrow}; c_{jx\downarrow}^\dagger S_{ky}^+ \rangle\rangle \\ \langle\langle \xi_{iy\uparrow}; c_{jx\downarrow}^\dagger S_{ky}^+ \rangle\rangle \\ \langle\langle \eta_{iy\uparrow}; c_{jx\downarrow}^\dagger S_{ky}^+ \rangle\rangle \end{pmatrix} \tag{293}$$

Applying Roth decoupling leads to:

$$\begin{aligned}\langle c_{ix\uparrow}c^{\dagger}_{jx\downarrow}S^{+}_{ky}\rangle = \sum_{l}\alpha_{ix}(C^{11}_{il}+C^{21}_{il})f^{1}_{ljk}+\beta_{ix}(C^{12}_{il}+C^{22}_{il})f^{2}_{ljk}\\ +\alpha_{iy}(C^{13}_{il}+C^{23}_{il})f^{3}_{ljk}+\beta_{iy}(C^{14}_{il}+C^{24}_{il})f^{4}_{ljk}\end{aligned} \tag{294}$$

With $f^{n}_{ljk}=\langle\psi^{n}_{l};c^{\dagger}_{jx\downarrow}S^{+}_{ky}\rangle$. We can compute directly f^{n} and get:

$$\begin{aligned}f^{1}_{ljk}&=\delta_{lj}\langle S^{-}_{lx}S^{+}_{ky}\rangle\\ f^{2}_{ljk}&=-\delta_{lj}\langle S^{-}_{lx}S^{+}_{ky}\rangle\\ f^{3}_{ljk}&=\delta_{lk}(C^{31}_{jl}+C^{32}_{jl})\\ f^{4}_{ljk}&=\delta_{lk}(C^{41}_{jl}+C^{42}_{jl})\end{aligned} \tag{295}$$

Hence, we get:

$$-\langle S^{-}_{ix}S^{+}_{iy}\rangle=-\phi_{x}\langle S^{-}_{ix}S^{+}_{iy}\rangle+\alpha_{y}(C^{13}_{0}+C^{23}_{0})^{2}+\beta_{y}(C^{14}_{0}+C^{24}_{0})^{2} \tag{296}$$

Which give what is in the text:

$$\langle S^{-}_{ix}S^{+}_{iy}\rangle=-\frac{\Omega_{y}}{1-\phi_{x}} \tag{297}$$

With :

$$\Omega_{y}=\alpha_{y}(C^{13}_{0}+C^{23}_{0})^{2}+\beta_{y}(C^{14}_{0}+C^{24}_{0})^{2} \tag{298}$$

A decoupling in the y channel would lead to:

$$\langle S^{-}_{iy}S^{+}_{ix}\rangle=-\frac{\Omega_{x}}{1-\phi_{y}} \tag{299}$$

With :

$$\Omega_{x}=\alpha_{x}(C^{31}_{0}+C^{32}_{0})^{2}+\beta_{x}(C^{41}_{0}+C^{42}_{0})^{2} \tag{300}$$

Finally let's consider $\langle n_{ix\uparrow}n_{iy\uparrow}\rangle=\frac{n_{iy}}{2}-\langle c_{ix\uparrow}c^{\dagger}_{ix\uparrow}n_{iy\uparrow}\rangle$ (x channel). We pose the following Green's functions:

$$\begin{pmatrix}A\\B\\F\\G\end{pmatrix}_{ijk}(\omega)=\begin{pmatrix}\langle\langle\xi_{ix\uparrow};c^{\dagger}_{jx\uparrow}n_{ky\uparrow}\rangle\rangle\\ \langle\langle\eta_{ix\uparrow};c^{\dagger}_{jx\uparrow}n_{ky\uparrow}\rangle\rangle\\ \langle\langle\xi_{iy\uparrow};c^{\dagger}_{jx\uparrow}n_{ky\uparrow}\rangle\rangle\\ \langle\langle\eta_{iy\uparrow};c^{\dagger}_{jx\uparrow}n_{ky\uparrow}\rangle\rangle\end{pmatrix} \tag{301}$$

To reconstruct $\langle n_{ix\uparrow}n_{iy\uparrow}\rangle$ we need to consider A+B in the equation of motions. Thus we get:

$$\begin{aligned}\langle c_{ix\uparrow}c^{\dagger}_{jx\uparrow}n_{kx\uparrow}\rangle = = \sum_l \alpha_{ix}(C^{11}_{il}+C^{21}_{il})f^1_{ljk} + \beta_{ix}(C^{12}_{il}+C^{22}_{il})f^2_{ljk} \\ + \alpha_{iy}(C^{13}_{il}+C^{23}_{il})f^3_{ljk} + \beta_{iy}(C^{14}_{il}+C^{24}_{il})f^4_{ljk}\end{aligned} \tag{302}$$

With $f^n_{ljk} = \langle\{\psi_i; c^{\dagger}_{jx\uparrow}n_{ky\uparrow}\}\rangle$. We compute them explicitly and get:

$$\begin{aligned}f^1_{ljk} &= \delta_{lj}(\frac{n_y}{2} - \langle n_{lx\downarrow}n_{ky\uparrow}\rangle) \\ f^2_{ljk} &= \delta_{lj}\langle n_{lx\downarrow}n_{ky\uparrow}\rangle \\ f^3_{ljk} &= \delta_{lk}(C^{31}_{jl}+C^{32}_{jl}) \\ f^4_{ljk} &= \delta_{lk}(C^{41}_{jl}+C^{42}_{jl})\end{aligned} \tag{303}$$

We get:

$$\langle n_{ix\uparrow}n_{iy\uparrow}\rangle = \frac{n_y}{2} - \alpha_x(C^{11}_0+C^{21}_0)\frac{n_y}{2} - \phi_x\langle n_{ix\downarrow}n_{iy\uparrow}\rangle - \Omega_y \tag{304}$$

In the y channel we get:

$$\langle n_{iy\uparrow}n_{ix\uparrow}\rangle = \frac{n_x}{2} - \alpha_y(C^{33}_0+C^{43}_0)\frac{n_x}{2} - \phi_y\langle n_{iy\downarrow}n_{iy\uparrow}\rangle - \Omega_x \tag{305}$$

Another Roth decoupling needs to be done on $\langle n_{ix\downarrow}n_{iy\uparrow}\rangle$. It is very similar to the one on $\langle n_{ix\uparrow}n_{iy\uparrow}\rangle$. We obtain:

$$\langle n_{ix\downarrow}n_{iy\uparrow}\rangle = \frac{n_y}{2} - \alpha_x(C^{11}_0+C^{21}_0)\frac{n_y}{2} - \phi_x\langle n_{ix\uparrow}n_{iy\uparrow}\rangle \tag{306}$$

For the x channel. In the y channel we get:

$$\langle n_{iy\downarrow}n_{ix\uparrow}\rangle = \frac{n_x}{2} - \alpha_y(C^{33}_0+C^{43}_0)\frac{n_x}{2} - \phi_y\langle n_{iy\uparrow}n_{ix\uparrow}\rangle \tag{307}$$

We can therefore express $\langle n_{ix\uparrow}n_{iy\uparrow}\rangle$. There are two decoupling (x/y) for $\langle n_{ix\uparrow}n_{iy\uparrow}\rangle$ and two for $\langle n_{ix\downarrow}n_{iy\uparrow}\rangle$. Since $\langle n_x n_y\rangle = \langle n_y n_x\rangle$, we consider the symetrize expression obtain by taking the average of all of the four decoupled expressions, as Roth did in her original paper Ref. [101]. We get :

$$\langle n_{ix\uparrow}n_{iy\uparrow}\rangle = \frac{1}{2}\sum_{\alpha\in(xy)}\frac{\Omega^{\alpha}_0 - \Omega_{\bar{\alpha}}}{1-(\phi_\alpha)^2} \tag{308}$$

With:

$$\begin{aligned}\Omega^x_0 &= \frac{n_y}{2}[\alpha_x(C^{11}_0+C^{21}_0)-1](-1+\phi_x) \\ \Omega^y_0 &= \frac{n_x}{2}[\alpha_y(C^{33}_0+C^{43}_0)-1](-1+\phi_y)\end{aligned} \tag{309}$$